EURADOS Report 2024-02
Oberschleißheim, May 2024

EURADOS
European Radiation Dosimetry Group e. V.

Computational Methods in Dosimetry – State of the Art and Emerging Developments: Proceedings of the 15th EURADOS School, Belgrade, June 23rd, 2022

Manuel Bardiès, Robert Bernat, Carles Domingo Miralles, Paolo Ferrari, Pasquale Lombardo, Vladimir Markovic, Francesc Salvat Pujol, Emanuele Scifoni, Rick Tanner, Maria Zankl

ISSN 2226-8057
ISBN 978-3-943701-37-1
DOI 10.12768/2z7y-7606

European Radiation Dosimetry Group e. V.

EURADOS Report 2024-02

Neuherberg, May 2024

Computational Methods in Dosimetry – State of the Art and Emerging Developments: Proceedings of the 15th EURADOS School, Belgrade, June 23rd, 2022

Manuel Bardiès[1], Robert Bernat[2], Carles Domingo Miralles[3], Paolo Ferrari[4], Pasquale Lombardo[5], Vladimir Markovic[6], Francesc Salvat Pujol[7], Emanuele Scifoni[8], Rick Tanner[9], Maria Zankl[10]

[1] National Institute of Health and Health Research (INSERM), France

[2] Ruđer Bošković Institut (RBI), Croatia

[3] Autonomous University of Barcelona, Spain

[4] Radiation Protection Institute (ENEA), Italy

[5] Nuclear Research Centre (SCK.CEN), Belgium

[6] University of Kragujevac, Serbia

[7] European Nuclear Research Centre (CERN), Switzerland

[8] Trento Institute for Fundamental and Applied Physics (TIFPA), Italy

[9] UK Health Security Agency, United Kingdom

[10] Helmholtz Zentrum München German Research Centre for Environmental Health (HMGU), Germany

ISSN 2226-8057

ISBN 978-3-943701-37-1

DOI 10.12768/2z7y-7606

Editors: Hans Rabus[1,2], Sebastian Trinkl[3,4]

[1] Physikalisch-Technische Bundesanstalt, Berlin, Germany

[2] Chairperson, EURADOS WG 6 “Computational Dosimetry”

[3] Bundesamt für Strahlenschutz, Neuherberg, Germany

[4] Member of the EURADOS Council

Reviewers: Stefano Agosteo[1], Roger Harrison[2], Roberto Versaci[3]

[1] Politecnico di Milano, Milan, Italy

[2] University of Newcastle, Newcastle, United Kingdom

[3] The Extreme Light Infrastructure ERIC, ELI Beamlines Facility, Dolni Brezany, Czech Republic

Imprint

Issued by:
European Radiation Dosimetry e. V.
Ingolstädter Landstraße 1
85764 Oberschleißheim
Germany
office@eurados.org
www.eurados.org

The European Radiation Dosimetry e.V. is a non-profit organization promoting research and development and European cooperation in the field of the dosimetry of ionizing radiation. It is registered in the Register of Associations (Amtsgericht München, registry number VR 207982) and certified to be of non-profit character (Finanzamt München, notification from 2023-03-14).

Liability Disclaimer

No liability will be undertaken for completeness, editorial or technical mistakes, omissions as well as for correctness of the contents.

Content:

Foreword

The 15th EURADOS School "Computational Methods in Dosimetry – State of the Art and Emerging Developments" took place within the framework of the EURADOS Annual Meeting 2022, which marked the 40th Anniversary of EURADOS. The theme of the School was motivated by the previous completion of a series of intercomparisons organised by Working Group 6 "Computational Dosimetry" and the publication of a Virtual Special Issue[1] in Radiation Measurements which collected the articles on the results and findings of these intercomparisons.

The slides of the presentations given at the School are available on the EURADOS website[2] and recordings of most of the presentations can be found on the EURADOS YouTube channel[3]. This EURADOS report contains written summaries of the presentations by most of the speakers at the School.

The first two chapters give an introduction to the topic of computational dosimetry and to the foundations of the Monte Carlo technique which plays an important role in this area. In the third chapter, the important practical aspect of how to use Monte Carlo techniques in an efficient way is addressed. The ensuing chapter 4 deals with the implementation of numerical anthropomorphic phantoms in Monte Carlo simulation, a highly relevant aspect for the use of Monte Carlo simulations in radiation protection.

Chapter 5 focusses on another important aspect of computational dosimetry, the use of unfolding techniques to determine neutron spectra from measurements. Both chapters 4 and 5 already allude to EURADOS intercomparisons in computational dosimetry. The history of intercomparisons organized by EURADOS WG6 is reviewed in chapter 6 which also includes a reproduction of the summary paper from the Special Issue on the common points and the lessons learnt from these exercises.

The second part of the report relates to trends and new developments in computational methods in dosimetry. The advances of the OpenDose3D project, which aims at building a sound basis for dosimetry in nuclear medicine, are described in chapter 7. New developments in radiotherapy treatment planning for external radiotherapy using particle beams are given in chapter 8 and flexible computational phantoms for use with simulations for the development personal online dosimetry in chapter 9. The final chapter 10 is devoted to the issue of data processing in radiation protection dosimetry, an important aspect of increasing digitisation in this field.

[1] https://www.sciencedirect.com/journal/radiation-measurements/special-issue/10P2TQP6G3F

[2] https://eurados.sckcen.be/events/winter-schools

[3] https://www.youtube.com/EURADOS

1. Introduction to Computational Dosimetry

Paolo Ferrari, ENEA-IRP Radiation Protection Institute, Italy; **José-Maria Gómez-Ros**, CIEMAT, Madrid (Spain)

Abstract

Computational physics is a discipline that can ideally be found at the intersection of Physics, Computer Science and Mathematics. Computational dosimetry can be defined as one of their daughters devoted to radiation metrology (Siebert and Thomas, 1997). An alternative definition, reported in the same paper, states that computational dosimetry is the process of connecting and ordering known data, by means of relations based on theory or established models, in order to create new data and to reveal new insights: a quite challenging statement.

Computational dosimetry includes analytical, deterministic and Monte Carlo methods (MC) and due the vastness of this field, just a brief and incomplete introduction is outlined in the present chapter.

1.1. Analytical Methods

Only simple cases can be treated analytically (e.g., attenuation in semi-infinite media of an isotropically emitting gamma source homogeneously distributed on a surface). Point sources, line sources or simple volumetric sources represent the basis of this techniques that relies on reducing the real-life problem to be studied to an extremely simplified geometry.

The simplest case is the point-like source. A source can be considered point-like when its dimension are orders of magnitude smaller than the minimum distance at which the radiation quantity has to be estimated. Unfortunately, there is no general rule to decide whether a source can be treated as a point source, because all depends on the elements present in the scenario to be modelled.

Since the dosimetric quantity depends on particle fluence, all the formulae below refer to fluence estimation.

In the case of a point source in an infinite volume (so there is no reflection from the walls/boundaries), the particle fluence rate (particles per area and time) at a distance d can be estimated simply as:

$$\varphi = \frac{A}{4\pi d^2}. \tag{1.1}$$

Here, A is the activity of the source and d the distance at which the flux φ is calculated. Now considering the absorption due to the presence of the medium between the source and the measuring point, Eq. 1.1 is transformed into Eq. 1.2, where $\mu(E)$ is the attenuation factor of the medium crossed by the particles. Indeed, as we are generally not in "good geometry" conditions[4] a *build-up factor*, $B(E, \mu d)$, depending on energy and on the product of $\mu(E)$ and absorber thickness d, is introduced:

$$\varphi = \frac{A}{4\pi d^2} \times B(E, \mu d) \times e^{-\mu(E)d} \tag{1.2}$$

[4] A "good geometry" is a condition represented by a narrow beam, or a collimated beam, when a receptor/detector can receive only the unscattered part of the radiation.

For a mono-energetic point-like source of energy *E*, the dose rate in the material of the detector, characterized by the mass absorption coefficient $\mu_{en}(E)/\rho$, can be calculated as:

$$\dot{D} = \left(\frac{A}{4\pi d^2} e^{-\mu(E)d}\right) \times B(E,\mu d) \times \frac{\mu_{en}(E)}{\rho} \times E \tag{1.3}$$

The values of $B(E,\mu d)$ are tabulated and determined by expressions such as Eq. 1.4 where the quantities $A'(E)$, $\alpha_1(E)$, $\alpha_2(E)$ are determined through estimates of experimental data for different materials (Chilton et al., 1984).

$$B(E,\mu d) = A'(E) \times e^{-\alpha_1(E)\mu d} + [1 - A'(E)] \times e^{-\alpha_2(E)\mu d} \tag{1.4}$$

The situation becomes yet more complex in the case of a plane circular source with uniform activity distribution in an infinite medium (see Fig. 1.1).

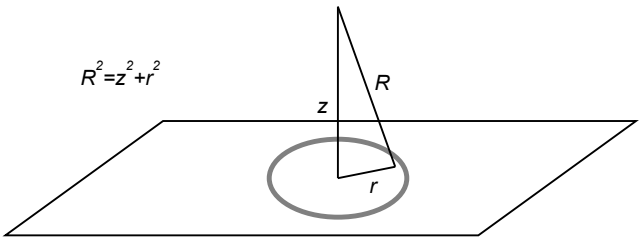

Fig. 1.1: Scheme of the calculation for a circular plane source.

In this case, considering a small portion of the source in a ring (as shown in Fig. 1.1), the fluence due to the activity A_S is given by Eq. 1.5, where r is the radius of the ring, R the distance to the measuring point and μ and ρ are the linear attenuation coefficient and the density of the medium interposed between the emission point and the measuring point respectively.

$$d\varphi = A_S \times 2\pi r \times dr \times B(E,\mu R) \times \frac{e^{-\mu R}}{4\pi R^2} \tag{1.5}$$

Integrating Eq. 1.5 one obtains the desired expression for the flux:

$$\varphi(z) = A_S \times 2\pi \int_0^\infty r \times B(E,\mu R) \times \frac{e^{-\mu R}}{4\pi R^2}\, dr = \frac{A_S}{2} \int_z^\infty B(E,\mu R) \times \frac{e^{-\mu R}}{R} dR \tag{1.6}$$

The solution of Eq. 1.6 is given by the numerical evaluation of the exponential integral (see for example table 5.1 in Abramowitz and Stegun (1964)).

Another important case, not so uncommon (just consider a syringe or a pipe containing a radiopharmaceutical in nuclear medicine), is the linear source (see the scheme in Fig. 1.2).

Assuming a finite source with a linear activity density S_l, the flux at the measuring point P is obtained employing basic trigonometry by the following equations with the source element dl, the distance a, and the angle θ:

$$l = a \times \tan(\theta) \tag{1.7}$$

$$\delta = \frac{a}{\cos(\theta)} \tag{1.8}$$

$$dl = \frac{a}{\cos^2(\theta)} \times d\theta \tag{1.9}$$

$$d\varphi = \frac{S_l}{4\pi\delta^2} \times dl \tag{1.10}$$

$$\varphi = \int_0^{\theta_1} \frac{S_l}{4\pi\delta^2} \times dl = \frac{S_l}{4\pi a}\theta_1 \tag{1.11}$$

The solution given in Eq. 1.11 applies to the special case where the measuring position is on a line perpendicular to the source through one of its endpoints as shown in Fig. 1.2. For a point in a different position with respect the source, other equations apply. What is worth emphasizing here is that the flux decreases with the inverse of the distance and not the inverse of the square of the distance, as in the case of the point-like source.

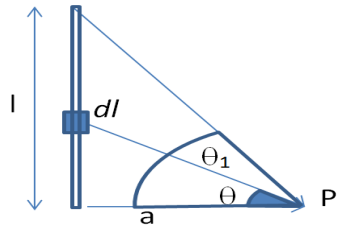

Fig. 1.2: Scheme of the calculation for a linear source

Similar expressions can be found in cases of radiation transport and shielding calculations for plane, cylindrical and slab sources (Jager et al., 1968). They are also known under the name of "Point Kernels" methods, all sharing the basic idea of calculating the field caused by a distributed source as the summation of the effects produced by the single elementary portion of source itself (Trubey, 1970).

These methods, that were employed also for the calculation of the specific absorbed fraction for internal contamination in the MIRD model (Bolch et al., 1999), and implemented using computer codes, still represent an important contribution in computational dosimetry. They can be used as a benchmark for other methods (in case of simple geometry) and as a practical and powerful tool (as well as time efficient) in some applications related to radiation shielding (Chucas and Curl, 2000, Ingersoll, 1986, Kotegawa, 1996, Li et al, 2020, Visonneau et al., 2017, Zeb and Wasim, 2017), dosimetry (Longeot et al., 2014, Marincel et al., 2007) and radiation transport (Marinkovic et al., 2007, Papadimitroulas et al., 2012).

1.2. Deterministic Methods

Deterministic methods have been implemented to find a solution of the Boltzmann equation. This equation was originally developed by the Austrian physicist for the kinetic theory of gases and successively adopted to describe the transport of radiation particles. The Boltzmann equation allows the evaluation of the particle density variation in a given volume of phase space due to the particle production, scattering, absorption and leakage from the volume itself.

The particle density, n, is the number of particles in a given volume at a certain position in space and time, with kinetic energy in a given energy range (E+dE) and a direction of motion in a given angular range (Ω+$d\Omega$). Particle density can be related to particle flux, φ, and velocity, v, through Eq. 1.12:

$$\varphi = n \times v \tag{1.12}$$

Thus, the variation in time of the particle density in the defined volume of phase space can be written as:

$$\frac{d}{dt}n = production - absorption - leakage \tag{1.13}$$

Developing the elements of Eq. 1.13 and employing the relation given in Eq. 1.12 between particle density and angular flux, one obtains:

$$\frac{1}{v}\frac{d}{dt}\varphi(\bar{r},E,t,\overline{\Omega}) = \dot{S} + \int_0^{\infty}\int_0^{2\pi}\Sigma_s(E'\to E,\Omega'\to\Omega)\varphi\,(E',\Omega',t,\bar{r})dE'd\Omega' \\ -\Sigma_a\varphi(\bar{r},E,t,\overline{\Omega}) - \overline{\Omega}.\overline{\nabla}\varphi(\bar{r},E,t,\overline{\Omega}) \tag{1.14}$$

Here, $\dot{S}$ represents the possible source rate term, generating particles in the considered volume; the integral represents the in-scattering term, i.e., particles originally not belonging to the considered phase space that, because of the scattering, are moved in the "useful" angular and energy range. The third term on the right-hand side is just the absorption term (particles that are removed because of being absorbed by the medium) and the last term, associated with the gradient of the flux, is the leakage term, representing the particles exiting the volume.

The initial and boundary conditions of Eq. 1.14 are respectively:

$$\varphi(\bar{r},E,0,\overline{\Omega}) = \varphi_0 \tag{1.15}$$

$$\varphi(\bar{r},E,0,\overline{\Omega}) = 0\ if\ \overline{\Omega}.\bar{\mathrm{k}} < 0\ (\ k\ is\ the\ unit\ vector\ of\ the\ surface) \tag{1.16}$$

Eq. 1.16 expresses the fact that the volume cannot contain holes or concavities since otherwise a particle exiting from the volume, i.e., a negative contribution to Eq. 1.14, could possibly re-enter in the volume, thus invalidating Eq. 1.14.

Notwithstanding the conditions in Eqs. 1.15 and 1.16, Eq. 1.14 cannot be solved analytically as it stands. Additional, more restrictive conditions are required, such as, for example, stationary state (time-independent), one-dimensionality and mono-energetic particles, allowing the application, for example, of spherical harmonics, or the Fokker-Planck approximation, or phase-space discretization and numerical integration.

In nuclear engineering, with simple geometries (such as infinite slabs), homogeneous media (i.e., cross-sections are the same at each point), "good" sources (giving no space singularity problems), and flux not rapidly varying with position, Fick's diffusion law can be applied to neutron flux. This transforms a simplified version of Eq. 1.14 into a "wave equation" that can be easily solved through separation of variables (time and space) and the "classical" technique based on the superimposition of cosine and sine eigenfunctions (Duderstad and Hamilton, 1975).

A powerful numerical approach to solve Eq. 1.14 is represented by the Finite Difference Method (FDM) and the Finite Element Method (FEM). FDM is a numerical technique that solves the problem approximating the differential equation with finite differences (Chapra and Canale, 2015). FEM defines a mesh of values for a physical field, discretizing the geometry in a series of finite elements in which a simplified version of the original equation is applied; then the global geometry is reconstructed into a global system of equations for the final calculation (Moaveni, 1999). Of course, there is a price to be paid with these techniques. The original single transport equation 14 is substituted by *n* coupled (simpler) equations (called S_n equations) where *n* depends on the discretization step.

This methodology was implemented in several computer codes. Just to give a short and incomplete list, we can mention: ANISN, that solves the one-dimensional Boltzmann transport equation for neutrons or gamma rays in slab, sphere, or cylinder geometries (Engle, 1967); ATTILA, that solves the

standard multigroup S_n equations on 3-D unstructured tetrahedral meshes (Wareing et al., 1997); DANTSYS, designed to solve the time-independent, multigroup discrete ordinates form of the Boltzmann transport equation in several different geometries (Alcouffe et al., 1995); DOORS, a discrete ordinates transport code system including the most recent versions of CCC-0543/TORT-DORT, CCC-0254/ANISN-ORNL, CCC-0628/GBANISN and CCC-0351/FALSTF (Rhoades and Simpson 1997); and SCEPTRE, that solves the linear Boltzmann transport equation for one-, two- and three-dimensional geometries capable of handling any particle type for which multigroup-Legendre cross sections are available (Bohnhoff et al., 2016).

1.3. Monte Carlo Methods

A completely different approach is represented by Monte Carlo methods (Brown, 2005, Lux and Koblinger, 1990, Seco and Verhaegen, 2013, Vassiliev, 2017) which, instead of solving the Boltzmann equation through numerical techniques, attempt to simulate the radiation transport through matter starting from the basic knowledge of the physical interactions of the radiation. This is done by sampling the distance between interactions and the path travelled by the particle, the interaction type, the angular distribution and the energy loss, the production of secondary particles and by scoring of the physical quantity to be tallied; a procedure that is repeated for a very large number of particle histories.

The Monte Carlo technique is based on a simple assumption that the history of a particle inside a medium is the succession of independent steps (a so-called Markov chain) that can be treated separately through the same algorithm. When the particle is finally absorbed or exits from the boundary of the considered world, another particle is generated and followed. The probabilities that rule the different interactions occurring to the particle are just the natural probability expressed through the cross-sections that depends on the energy (and angle) of the particle and on the elemental composition of the traversed medium. The quantity to be tallied (a flux at a point, the energy deposition in a volume, the current through a surface, etc.) is obtained by calculating the mean of the contributions of the particle histories to the tallied quantity. The central limit theorem ensures that increasing the number of simulated particle histories, the mean of the sampled histories converges to the mean of the population (i.e., it converges to the expected real value).

The core of the Monte Carlo method is a (pseudo)random number generator that supplies uniformly distributed numbers in the range [0,1]. These are used each time to sample from the distribution (normalized to one) of the start location of the particle in a volume or on a surface, of the particle direction, and of the cross-section establishing the type of interaction (if any occurs).

Just to give a practical example of the how Monte Carlo technique works, a description of a simple photon tracking is given below.

If we consider a monoenergetic beam of photons passing through a medium, we can apply the well know attenuation law to determine the fraction of the photons that "survive" un-collided:

$$\frac{I}{I_0} = e^{-\mu x} \tag{1.17}$$

Here I_0 is the intensity of the beam before entering the medium of attenuation coefficient μ, and I is the intensity of the beam at position x inside the medium.

If we consider the history of just one particle, the right-hand side of Eq. 1.17 is related to the probability of no interaction with the medium. The probability of interaction with the medium, after having travelled a distance x inside the medium, is thus given by:

$$P(x) = 1 - e^{-\mu x} \tag{1.18}$$

Now, this *P(x)* is a cumulative probability and, by definition, bounded between 0 and 1, where 0 represent the case in which the photon certainly escapes, corresponding to the value $x = 0$ (no medium, no interaction) and the case 1 corresponds to an infinite distance x travelled in the medium, in which case an interaction certainly happens.

This consideration allows us to draw a random number, r^*, uniformly distributed between 0 and 1 and to assign it to *P(x)* expressing the probability of the given interaction:

$$r^* = P(x) = 1 - e^{-\mu x} \tag{1.19}$$

Eq. 1.19 can be easily inverted giving Eq. 1.20 for the point x^* where this interaction has occurred:

$$x^* = -\frac{1}{\mu}\ln(1 - r^*) \tag{1.20}$$

Now, with the direction of the photon and the travelled distance x^*, one can define the track of the photon inside the medium. Comparing its travelled distance and the distance to the nearest medium boundary, *D*, it is possible to say whether the interaction really occurred, namely when $x^* < D$. If the interaction occurred, cross-sections are needed to determine which kind of interaction has happened to the photon at that point. Taking the normalized total cross section, for the given energy and medium, this is the total cumulative probability in which the possible interactions (photoelectric, Compton scattering, Rayleigh scattering, pair production, …) are distributed with their natural probabilities. Drawing another random number between 0 and 1 allows the determination of the interaction that occurred at the point x^*[5]. All the parameters of the interaction (energy, energy released, position, direction) are stored and ready for use in the subsequent step of the tracking. Conversely, if $x^* > D$, the possible interaction occurred outside the medium, i.e., no "real" interaction occurred in the medium, and the photon just travelled un-collided through the medium to its boundary and escapes from it. When the photon escapes from the first medium, it enters in a second medium and the previous algorithm has to be repeated. In that case the starting point coincides with the intersection point between the photon track, given by the original direction sampled at the beginning of its history, and the medium's boundary surface.

After having calculated the subsequent steps of the photon history and its geometrical tracking inside the different materials, the photon history ends when the photon is absorbed (as in a photoelectric interaction) or reaches the boundary of the world (in that case the particle history is just terminated).

The final value of the tallied quantity is obtained by averaging the results of the stored quantities derived from the simulation of n particles.

The physics of the Monte Carlo techniques applied to radiation transport really lies in the cross-sections and, when not available (as in the case of photons energies higher than 1 GeV or neutrons higher than 150 MeV) in nuclear physics models (such as the Cascade-Exciton Model, CEM (Mashnik and Sierk, 2001) or the Los Alamos version of the Quark - Gluon String Model LAQGSM (Goudima et al., 2001)).

[5] In case of Compton scattering, for example, the Klein - Nishina energy-angular distribution can also be normalized and sampled, obtaining the direction of the photons and allowing the calculation of the energy of the re-emitted photon and "knocked-out" electron.

There are a number of Monte Carlo codes available. Some of them can treat a variety of different particles (neutron, photons, electrons, hadrons, charged ions, …), implying that not all the particles can be followed with a detailed physical treatment. This implies that a certain "discretization" in the particle tracking description occurs, which is, for example, the case of electrons tracking in the MCNP code family. This is divided into a number of sub-steps for which, at energies lower than a given threshold, the interactions are treated as a continuous energy loss and only "catastrophic events" (when electron "disappears" or other particles are generated) are simulated explicitly (MCNP5, 2003, Thomson and Kawrakow, 2011). Other codes, conversely, were created for simulating only specific particles and their related physics. To the first group belong codes like FLUKA (Ferrari et al., 2005), that can treat around 60 types of different particles, GEANT4 (Agostinelli et al 2003), MCNP6 (Pelowitz, 2013) and PHITS (Sato et al., 2018); to the second group TRIPOLI4 (Brun et al., 2015), treating only neutrons, photons and electrons, EGS5 (Hirayama et al., 2005), dedicated to photons and electrons, as well as, PENELOPE (Salvat, 2015) and OpenMC (Romano et al., 2015), an open-source code treating neutrons and photons.

One of the main crucial characteristics of Monte Carlo codes is their ability to describe the radiation transport inside complex geometries, such as the structure of organ and tissues inside a human body. This important feature was employed since the beginning of their application in this field to calculate the dose conversion coefficients needed in radiation dosimetry and radiation protection (Bolch et al., 1998, ICRP, 1991, ICRU, 1998, Snyder et al., 1974). This ability became even more essential when detailed voxel models (i.e., human models constructed starting from a tomographic set of images of real individuals) were introduced for radiation protection issues (ICRP, 2009).

The quantity better suited for describing radiation transport in the different geometries is particle fluence. In Monte Carlo codes, it can be estimated through the track length. The particle fluence is defined as the number of particles dN incident on a sphere of cross-sectional area da:

$$\phi = \frac{dN}{da} \tag{1.21}$$

It is easy to see, at least considering the dimensions, that the fluence is equivalent to the quotient of dl, the sum of the lengths of particle trajectories in the volume dV, and the volume of the sphere itself:

$$\phi = \frac{dl}{dV} \tag{1.22}$$

In particular if we consider that:

$$\bar{\phi}.V = \int_V \; dV.\phi(\vec{r}) \tag{1.23}$$

$$\bar{\phi} = \frac{1}{V}\int_V \; dV.\phi(\vec{r}) \cong \frac{1}{V}\sum_j S_j \tag{1.24}$$

Here, $\bar{\phi}$ is the average fluence in the volume and S_j is the j-th path length.

Knowing the energy distribution of fluence, ϕ_E, enables the computation of all the other relevant quantities such as the number of reactions for a given physical interaction:

$$N_\sigma = \int dE.V.\rho_a\sigma(E)\phi_E \tag{1.25}$$

Here, ρ_a is the atomic density and $\sigma(E)$ the cross section for the given interaction.

It is also possible to calculate the kerma k

$$k = \int dE.E.\frac{\mu_{tr}}{\rho}\phi_E \tag{1.26}$$

and, with the proper conversion coefficients, the operational quantities such as the ambient dose equivalent $H^*(10)$:

$$H^*(10) = \int dE . \frac{H^*(10)}{\phi}(E)\phi_E \tag{1.27}$$

The conversion coefficients between operational quantities and field quantities all have been calculated with Monte Carlo codes (ICRU, 1998, 2020). The Specific Absorbed Fractions, to be employed for internal contamination dosimetry, have been calculated in the MIRD analytical phantom (Snyder et al., 1975) as the conversion coefficients for the organ doses, initially in the MIRD phantom and more recently in the ICRP voxel reference adult models (ICRP, 2009) for several radiation particles in a large range of energies (ICRP, 2010).

Monte Carlo methods are powerful tools in computational dosimetry but, obviously, there is a price to be paid, which is related to the uncertainties associated with their results. The uncertainty of a Monte Carlo simulation can be conceptually divided into two components: the accuracy and the precision of the simulations.

Accuracy is related to how much the simulated world is consistent with the problem to be treated and is related to a series of parameters influencing the simulation, i.e., the quality of the data used for the simulations (e.g., exact dimensions and minimum spatial resolution, properties of the materials, quality of the physical models and cross sections, energy binning, …), the possible "cut-off" chosen by the user (e.g., main particle energy cut-off, secondary charged particle tracking not followed, coherent photon scattering disabled, …) and the employment of the most appropriate Monte Carlo code to the problem to be treated (i.e., many codes are multipurpose, others can only treat specific particles but, in general, in a more accurate way). It is not always possible to increase the quality of Monte Carlo results in terms of accuracy because some limitations are unavoidable, and it is crucial that the user be aware of them.

The quantity that, at least theoretically, can be reduced to zero is the uncertainty associated to the precision of the results. The central limit theorem ensures the convergence of the mean of the calculated results to the mean of the population when the number of simulated particles goes to infinity. Considering the mean (Eq. 1.28) and its variance (Eq. 1.29) and calculating the relative error (Eq. 1.30), it is easy to see how the relative error of the mean diminishes as the inverse of the square root of the number of simulated particles.

$$\bar{x} = \frac{1}{N}\sum_{i=1}^{N} x_i \tag{1.28}$$

$$S_{\bar{x}} = \frac{1}{(N-1)}\sum_{i=1}^{N}(x_i - \bar{x})^2 = \frac{1}{(N-1)}\overline{(x^2)} - (\bar{x})^2 \tag{1.29}$$

$$R = \frac{S_{\bar{x}}}{\bar{x}} = \sqrt{\frac{1}{N}\left(\frac{\overline{x^2}}{\bar{x}^2} - 1\right)} \propto \frac{1}{\sqrt{N}} \tag{1.30}$$

This means that the quality of the results, in terms of their precision, can be "easily" improved by increasing the number of simulated particles. This is not a problem in many cases but, for example, for deep radiation penetration problems (as for high energy photons and neutron shielding calculations) the simulation time can become unacceptable (easily reaching weeks without any convergence of the results) and different strategies have to be adopted.

For example, besides the possibility of working with a version of the code suited to parallel computing, so-called Variance Reduction Techniques (VRT) can be employed (Garcia-Pareja et al., 2021, Gualdrini and Ferrari, 2011). VRT basically modify the natural probability making some events

more or less "probable" (rejection techniques, Russian-roulette) or "deterministic" (forced collisions, next event estimator) in a chosen region of the phase-space of the geometry. These biased probabilities help to save time for the simulations. Eventually the results are renormalized, taking into account the natural probability and the bias applied to them. Due to their possible "catastrophic" effect on the simulation, VRT have to be handled with care; their improper use can produce erroneous and unreliable results that can be pass unnoticed (Haghighat, 2003).

1.4. References

Abramowitz M., Stegun I.A. (Editors), 1964. Handbook of Mathematical Functions, National Bureau of Standards, U.S.A.

Agostinelli et al., 2003. Geant4 - a simulation toolkit Nuclear Instruments and Methods in Physics Research Section A: Accelerators, Spectrometers, Detectors and Associated Equipment, 506, 250-303.

Alcouffe, R.E., Baker, R.S. Brinkley, F.W., Duane, R. Marr, D.R., O'Dell, R.D., Walter, W.R., 1995. DANTSYS: A Diffusion Accelerated Neutral Particle Transport Code System. LA-12969-M MANUAL, Los Alamos National Laboratory, U.S.A.

Bohnhoff, W.J., Drumm, C.R., Fan, W.C., Pautz, S.D., Valdez, G.D., 2016. SCEPTRE 1.7 Quick Start Guide, SAND2016-3250, Sandia National Laboratory, U.S.A.

Bolch Wesley E., Lionel G. Bouchet, James S. Robertson, Barry W. Wessels, Jeffry A. Siegel, Roger W. Howell, Alev K., 1999. MIRD Pamphlet N. 17: The Dosimetry of Nonuniform Activity Distributions – Radionuclide S Values at the Voxel Level. The Journal of Nuclear Medicine, 40, 11S-36S.

Brown F., 2005. Fundamentals of Monte Carlo Particle Transport. Report LA-UR-05-4983, Los Alamos National Laboratory, U.S.A.

Brun E. et al., 2015. TRIPOLI-4®, CEA, EDF and AREVA reference Monte Carlo code. Annals of Nuclear Energy 82, 151-160.

Chapra, S.C. and Canale, R.P., 2015. Numerical Methods for Engineers, McGraw Hill.

Chilton, A.B., Shultis, J.K., Faw, R.E, 1984. Principles of radiation shielding, Prentice-Hall Inc.

Chucas S., Curl I., 2000. Streaming Calculations using the Point-Kernel Code RANKERN Journal of Nuclear Science and Technology, Supplement 1, 515-519.

Duderstad J.J. and Hamilton L.J., 1975. Nuclear Reactor Analysis, Wiley

Engle, W.W., 1967. A user manual for ANISN A One-Dimensional Discrete Ordinates Transport Code with Anisotropic Scattering, Oak Ridge National Laboratory, U.S.A.

Ferrari, A., Fasso, A., Ranft, J., Sala, P.R., 2005. FLUKA: a multi-particle transport code, CERN 2005-10, INFN/TC_05/11, SLAC-R-773.

Garcia-Pareja S, Lallena A.M., Salvat F., 2021. Variance-Reduction Methods for Monte Carlo Simulation of Radiation Transport, Frontier in Physics, 9, 718873.

Gualdrini, G., Ferrari, P., 2011. Monte Carlo Variance Reduction Techniques: An Overview With Some Practical Examples. Radiation Protection Dosimetry, 146, 425–433.

Gudima, K. K., Mashnik, S. G., and Sierk, A. J., 2001. LANL Report LA-UR-01-6804, Los Alamos National Laboratory, U.S.A.

Haghighat A., 2003. Monte Carlo Variance Reduction with deterministic importance functions, Progress in Nuclear Energy, 42, 25-53.

Hirayama, H., Namito, Y., Bielajew, A.F., Wilderman, S.J., Nelson, W.R., 2005. SLAC-R-730 (2005) and KEK Report 2005-8.

ICRP 1991. Recommendations of The International Commission on Radiological Protection ICRP Publication 60, International Commission on Radiological Protection, Pergamon Press Oxford.

ICRP 2009. Publication 110 Adult Reference Computational Phantoms

ICRP 2010. Publication 116 Conversion Coefficients for Radiological Protection Quantities for External Radiation Exposures

ICRU 1998 Report 57 Conversion coefficients for use in radiological protection against external radiation. International Commission on Radiation Units and Measurements Bethesda, MD, USA.

ICRU 2020. Report 95, Operational Quantities for External Radiation Exposure. International Commission on Radiation Units and Measurements Bethesda, MD, USA.

Ingersoll, D. T., 1986. User's Manual for PUTZ: A Point-Kernel Photon Shielding Code. Oak ridge National Laboratory ORNL /TM-9803, Oak Ridge National Laboratory, U.S.A.

Jager, R.G., Blizard, E.P., Chilton, A.B, Grotenhuis, M., Hönig, A., Jaeger, T.A., Eisenlohr, H.H. (Eds), 1968. Engineering Compendium on Radiation Shielding. Springer, Berlin

Kotegawa, H., 1996. A Point Kernel Shielding Code, PKN-HP, for High Energy Proton Incident JAERI-Data/Code 96-020

Li, M., Xu, Z., Li, W., Yang, J., Yang, M., Lu, H., Dai, X., 2020. MIGSHIELD: A new model-based interactive point kernel gamma ray shielding package for virtual environment. Nuclear Engineering and Technology, 52, 1557-1564.

Longeot, M., Dupont, B., Zweers, M., Malvagi, F., Trama, J.-C., Dubost, J., 2014. PANTHERE: simulation software for 3D dose rate calculation in complex nuclear facilities. Progress in Nuclear Science and Technology, 4, 557-560.

Marincel, M.K., Weiner, R.F., Osborn, D.M., 2007. MICROSHIELD analysis to calculate external radiation dose rates for several spent fuel casks. Waste Management Conference, February 25-March 1, 2007, Tucson, AZ, U:S:A.

Marinkovic, P., Ilic, R., Spaic, R., 2007. A 3D point-kernel multiple scatter model for parallel-beam SPECT based on a gamma-ray buildup factor. Physics in Medicine and Biology, 52, 5785-5802.

Mashnik, S. G., Sierk, A. J., 2001. In: Proc. AccApp00, Washington, DC, USA, 2000, ANS, La Grange Park, IL, p. 328; E-print: nucl-th/0011064.

MCNP5 2003 – A General Monte Carlo N-Particle Transport Code, Version 5 Volume I: Overview and Theory. LA-UR-03-1987, Los Alamos National Laboratory, U.S.A.

Moaveni, S., 1999. Finite Element Analysis. Prentice Hall.

Papadimitroulas, P., Loudos, G., Nikiforidis, G. C., Kagadis, G. C., 2012. A dose point kernel database using GATE Monte Carlo simulation toolkit for nuclear medicine applications: comparison with other Monte Carlo codes. Medical Physics 39, 5238-5247.

Pelowitz, D.B. (editor), 2013. MCNP6 USER'S MANUAL Version 1.0 (LANL Los Alamos LA-CP-13-00634).

Rhoades, W.A., Simpson, D.B., 1997. The TORT Three-Dimensional Discrete Ordinates Neutron/Photon Transport Code, ORNL/TM-13221, Oak Ridge National Laboratory, U.S.A.

Romano, P.K., Horelik, N.E., Herman, B.R., Nelson, A.G., Forget, B., Smith, K., 2015. OpenMC: A State-of-the-Art Monte Carlo Code for Research and Development. Annals of Nuclear Energy, 82, 90–97.

Salvat F., 2015. The Penelope code system. Specific features and recent improvements. Annals of Nuclear Energy, 82, 98-109.

Sato, T., Iwamoto, Y., Hashimoto, S., Ogawa, T., Furuta, T., Abe, S., Kai, T., Tsai, P.E., Matsuda, N., Iwase, H., Shigyo, N., Sihver, L., Niita, K., 2018. Features of Particle and Heavy Ion Transport Code System PHITS Version 3.02. J ournal of Nuclear Science and Technology, 55, 684-690.

Seco J., Verhaegen F. (eds.) 2013. Monte Carlo Techniques in Radiation Therapy. CRC Press.

Snyder, W.S., Ford, M.R., Warner, G.G., 1974. Revision of MIRD pamphlet No. 5 entitled ''estimates of absorbed fractions for monoenergetic photon sources uniformly distributed in various organs of a heterogeneous phantom''. Report ORNL-4979, Oak Ridge National Laboratory, U.S.A.

Snyder, W.S., Ford, M.R., Warner, G.G., Watson, S.B., 1975. S, Absorbed Dose per Unit Cumulated Activity for Selected Radionuclides and Organs, MIRD Pamphlet No. 11, The Society of Nuclear Medicine, New York, U.S.A.

Thomson, R.M., Kawrakow, I., 2011. On the Monte Carlo Simulation of Electron Transport in the sub - 1 keV Energy Range. Medical Physics, 38, 4531-4534.

Trubey, D.K., 1970. Kernel methods for radiation shielding calculations. Nuclear Engineering and Design, 12, 423-447.

Vassiliev, O.N., 2017. Monte Carlo Methods for Radiation Transport: Fundamentals and Advanced Topics. Springer.

Visonneau, T., Pangault, L., Malouch, F., Malvagi, F., Dolci, F., 2017. NARMER-1: a photon point-kernel code with build-up factors. EPJ Web of Conferences, 153, 06028

Wareing, T.A., McGhee, J.M., Morel, J.E., 1997. ATTILA A 3-D unstructured tetrahedral-mesh Sn code. Nuclear Energy Agency of the OECD (NEA): OECD Publications.

Zeb, J., Wasim, M., 2017. U-Shielder – an open source software for the estimation of gamma shielding using depleted uranium. Radioprotection, 52, 273-275.

2. Monte Carlo Radiation Transport Simulations

Vladimir Markovic, University of Kragujevac, Serbia

Abstract

Transport of radiation can be described via transport equations, which present mathematical descriptions of this physical problem. Such an approach has drawbacks and can be complicated, especially in cases of inhomogeneous media with different composition. This problem is overcome by introducing the Monte Carlo method in radiation transport. This method is based on random sampling of relevant physical quantities which describe transport and interaction of particles with a medium. Randomness is used in a repetitive way, so that relevant variables can be estimated.

2.1. History of Monte Carlo

Monte Carlo method may be defined as a broad class of algorithms that rely on repeated random sampling to obtain numerical results. The underlying concept is to use randomness to solve problems that might either be stochastic or deterministic. This definition is quite general and does not address the practical applicability of the Monte Carlo method. The following example of estimating the value of the number π introduces readers to Monte Carlo approach.

Consider a square with a circle drawn inside it, as shown in Fig. 2.1. Now, if dots are drawn completely randomly inside the square, some will be inside the circle, while others will be outside it.

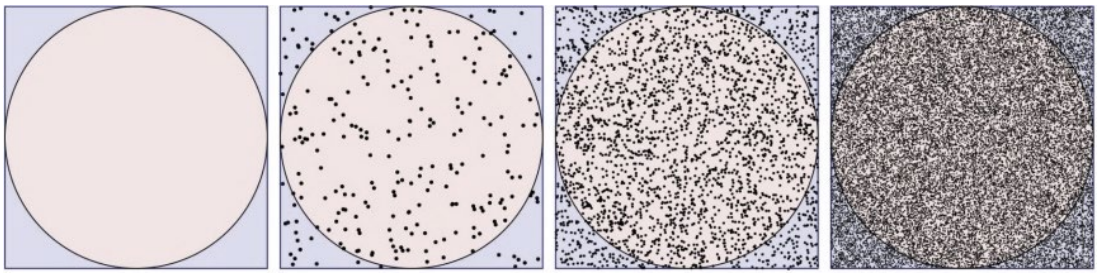

Fig. 2.1: Estimating value of π using the Monte Carlo method

To estimate π, we note that the relationship between the areas of square and circle is given by

$$\frac{P_{circle}}{P_{square}} = \frac{\pi r^2}{4r^2} = \frac{\pi}{4}. \tag{2.1}$$

On the other hand, the relationship between the areas of square and circle is proportional to the number of dots inside the square and the circle, respectively.

$$\frac{P_{circle}}{P_{square}} = \frac{N_{points\ inside\ of\ circle}}{N_{points\ inside\ of\ square}} \tag{2.2}$$

Combining the last two equations leads us to the value of the number π:

$$\pi = 4 \times \frac{N_{points\ inside\ of\ circle}}{N_{points\ inside\ of\ square}} \tag{2.3}$$

For the example presented in Fig. 2.1, the total number of sampled points is 248,100, leading to the estimate π= 3.14156. At this point it is very important to note that using the Monte Carlo method

does not enable the calculation of the exact value of the desired quantity. To get an exact value of π, an infinite number of points need to be sampled. Every finite number of sampled points will lead to estimated value of π with certain numerical accuracy. The more points are sampled, the greater the accuracy will be.

Historically, the Monte Carlo method dates back to 1777 (Comte de Buffon, 1777) when Comte de Buffon proposed his famous needle problem (Fig. 2.2a) and evaluated the probability for a needle to cross stripes on a sheet of paper (Fig. 2.2b).

$$p = \frac{2}{\pi}\frac{l}{t}. \tag{2.4}$$

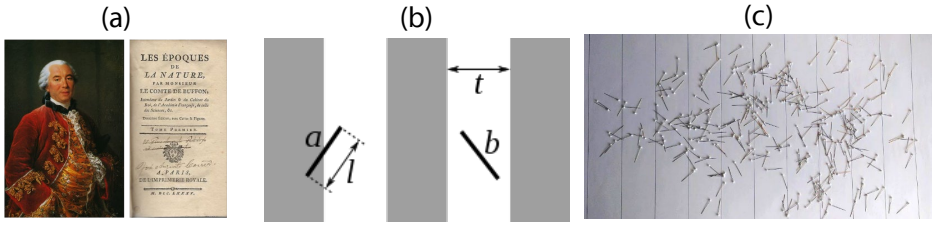

Fig. 2.2: a) Pictures of Comte de Buffon and the front page of his treatise; b) illustration of the geometry of the problem; c) illustration of a Monte Carlo calculation.

Tossing needles onto a sheet with stripes and counting the needles that crossed the stripes, as in Fig. 2.2c, one can estimate value of π. For the 314 needles in the Fig. 2.2c, 101 crossed the stripes, so:

$$\pi = \frac{\text{number of needles}}{\text{needles crossing lines}} = 3.109 \tag{2.5}$$

It is important to note that Comte de Buffon didn't use the Monte Carlo method, but rather just calculated the probability given by Eq. 2.4. A century later, Laplace 1886 suggested that this can be used to calculate value of π (Laplace, 1886).

The greatest expansion of the Monte Carlo method started when famous physicists and mathematicians realised that this method can be employed to solve some mathematically very complicated problems. The pillars of modern Monte Carlo techniques were the John von Neumann, Stanislaw Ulam, and Nicholas Metropolis, on the one hand, and Enrico Fermi, on the other (Metropolis, 1987). They encountered the problem of solving transport equations of the neutrons in inhomogeneous media. Mathematically it is practically impossible to obtain a solution of this problem for very complex systems. Applying boundary conditions on every discontinuity of the system leads to a large number of equations, impractical to handle. At that time, the first computers were invented, and the aforementioned scientists found the best way to employ their power. They used ENIAC - Electronic Numerical Integrator and Computer, and later MANIAC I - Mathematical Analyzer Numerical Integrator and Automatic Computer Model I to simulate neutron transport. It is interesting to note that Fermi invented a mechanical device called FERMIAC to perform numerical simulations.

Today personal computers are powerful enough to perform Monte Carlo simulations using advanced algorithms. For demanding problems, clusters and supercomputers are employed worldwide to solve difficult Monte Carlo problems.

2.2. Insight into radiation transport

Let us take further, deeper steps into the understanding of Monte Carlo, by starting with a simple problem – the two-dimensional movement of Brownian particles. This problem is interesting due to its simplicity. Namely, Brownian particles stochastically move by elastically colliding with atoms of the medium. In a collision, the scattering angle is uniformly random. That means that, in general, Brownian particles can be scattered by arbitrary angles, with no preferred direction (Fig. 2.3a).

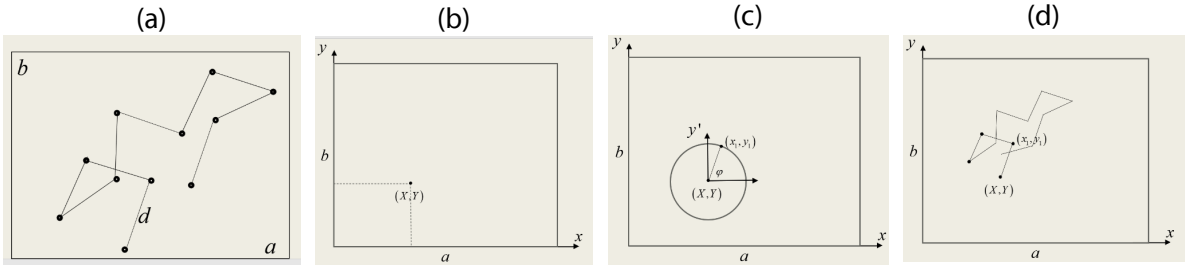

Fig. 2.3: a) random scattering of a Brownian particle; b) Cartesian coordinate system for the defined problem; c) Polar coordinate system for the defined problem; d) repeating the procedure of sampling points leads to a trajectory

To simulate this problem, we need to define the geometry. Let us assume that the particle moves inside a rectangular box with dimensions $a \times b$, and initially include more simplifications: let the path travelled between any two subsequent collisions be fixed and the particle experience only a random change of direction when a collision occurs. The start point of the particle is unknown and should be randomly chosen.

To work with the Monte Carlo method, we need a random number generator. This is usually an algorithm which iteratively can print out, or sample, numbers in no particular order – random numbers. Let us suppose that, at this point, we already have a random number generator, (a function **rand)**, which returns a random number. The procedure of the Monte Carlo simulation is as follows.

Step 1 - pick some arbitrary point in the rectangle. To describe its coordinates, it is natural to use a Cartesian coordinate system, shown in Fig. 2.3b. It is quite simple to randomly sample a starting point using the **rand** function, by calculating *X*=*a****rand** and *Y*=*b****rand**. These will be our starting coordinates.

Step 2 – let us move the particle in an arbitrary direction with a step length *d*. To choose the arbitrary direction, We introduce a polar coordinate system and consider a circle with radius *d*, with its centre at the starting point (Fig. 2.3c). The equation of the circle is $x'^2 + y'^2 = d^2$. In the polar coordinate system, $x' = \rho' \cos\varphi,\ y' = \rho \sin\varphi$, where $\rho' = d,\ \varphi \in [0, 2\pi]$. If we generate the angle randomly $\varphi = 2\pi \cdot \mathrm{rand}$, we can simply obtain a randomly generated point

$$x_1 = x + d\cos\varphi \ \text{ and } \ y_1 = y + d\sin\varphi\,. \tag{2.6}$$

Now, we can move the particle to this point and repeat the procedure (Fig. 2.3d).

2.2.1. Probability theory - continuous variables

For further familiarisation with the Monte Carlo technique, some theoretical aspects of probability theory - the foundation of MC – are instructive. By defining a random variable as a quantity whose value is obtained from repeatable processes, but cannot be predicted with certainty (e.g., counting

quanta from a radioactive source), we can introduce the concepts of probability, symbolized by *P*, and the probability density function (PDF), symbolized by *p*. Let *x* be a continuous random variable which takes values in the interval [x_{min}, x_{max}]. The probability is defined as

$$P\{x \mid x_1 < x < x_1 + dx\} = p(x_1)\,dx \text{ and } P\{x \mid x_1 < x < x_1 + dx\} = \lim_{N\to\infty} \frac{n}{N}, \tag{2.7}$$

Where *n* is the number of values of *x* that fall into the interval [x_1, x_1+d*x*], and *N* is the number of generated *x* values. Fig. 2.4a and b show examples of PDFs and Fig. 2.4c shows the cumulative distribution of the uniform PDF in Fig. 2.4b (see text).

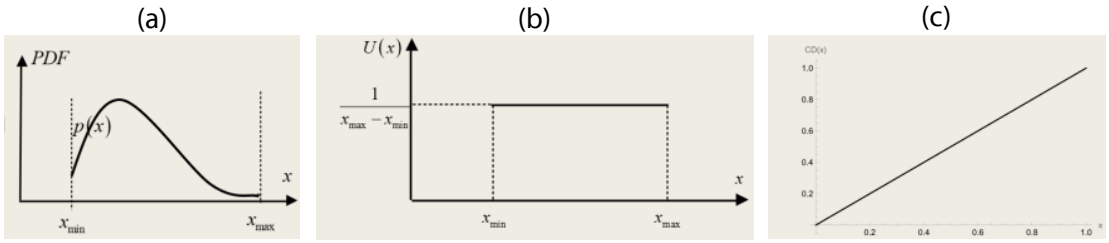

Fig. 2.4: a) Sample probability density function (PDF) of a random variable x having values between x_{min} and x_{max}; b) PDF of a uniform distribution U(x) of *x* between x_{min} and x_{max}; c) cumulative distribution CD(*x*) of a uniform distribution between $x_{min} = 0$ and $x_{max} = 1$.

Some important properties of the PDF are

$$p(x) \geq 0\,,\ \int_{x_{min}}^{x_{max}} p(x)\,dx = 1\,. \tag{2.8}$$

The mean value can be calculated as

$$\langle x \rangle = \int_{x_{min}}^{x_{max}} x \cdot p(x)\,dx\,, \tag{2.9}$$

and the standard deviation as $\sigma^2 = \langle x^2 \rangle - \langle x \rangle^2$, where

$$\langle x^2 \rangle = \int_{x_{min}}^{x_{max}} x^2 \cdot p(x)\,dx\,. \tag{2.10}$$

One very important example of a PDF is the uniform distribution $U(x);\ x \in [x_{min}, x_{max}]$ shown in the middle panel of Fig. 2.4b:

$$U(x) = \begin{cases} 1/(x_{max} - x_{min}) & x_{min} \leq x \leq x_{max} \\ 0 & x < x_{min} \wedge x > x_{max} \end{cases}, \tag{2.11}$$

A further step is to introduce the Cumulative Distribution (CD), defined as

$$CD(x) = \int_{x_{min}}^{x} p(x)dx\,. \tag{2.12}$$

The relations between the CD, the probability and the PDF are given in Eqs. 2.13 and 2.14.

$$P(x \mid a < x < b) = \int_a^b p(x)dx = CD(b) - CD(a), \tag{2.13}$$

$$p(x) = \frac{dCD(x)}{dx}, \tag{2.14}$$

For the uniform distribution

$$U(x) = \begin{cases} 1 & 0 \le x \le 1 \\ 0 & x < 0 \wedge x > 1 \end{cases}, \tag{2.15}$$

the $CDU(x) = x,\ x \in [0,1]$ is shown in Fig. 2.4c.

Some processes in nature are associated with their specific probability distributions, and the mathematical properties presented here can enable us to sample any random variable with a given PDF. At this point, the uniform distribution plays an important role. Namely, if we introduce the random variable $\zeta = CD(x)$, where CD is the cumulative distribution of an arbitrary PDF, this variable ζ is **uniformly distributed on the interval** $[0,1]$. This is a very important property, because it enables us to sample a random variable of any known PDF, starting with a uniformly distributed random variable and the inverse function method. Let us explore this property on a particular distribution, namely the exponential distribution:

$$p(x) = \frac{1}{\lambda} e^{-\frac{x}{\lambda}},\ x \ge 0\,. \tag{2.16}$$

By taking a uniform random variable,

$$\xi = CD(x) = \int_{x_{\min}}^{x} p(x)dx\,, \tag{2.17}$$

The upper limit can be calculated by integration

$$x = -\lambda \ln(1-\xi) \equiv -\lambda \ln(\xi), \tag{2.18}$$

Where the fact was used that if ζ is a uniform random variable, so is 1- ζ. This means that if we have a uniform random variable ζ, we can sample an exponentially distributed variable x by Eq. 2.17.

2.2.2. Random walk

At this point we have a mathematical method to continue with the simulation of the movement of a Brownian particle in a more realistic way. During the random movement, the Brownian particle does not move in steps of equal length between successive collisions. The mean free path is defined on average, whereas in particular steps, different free paths should be considered. The exponential distribution introduced by Eq. 2.16 is the PDF of the free path of the particle between interaction events. This means that by using Eq. 2.18, we can obtain particular values of the free path. If we use $d = -\lambda \ln(\zeta)$ in Eq. 2.6, the motion of our Brownian particle will be as in Fig. 2.5a, where the free paths are randomly sampled.

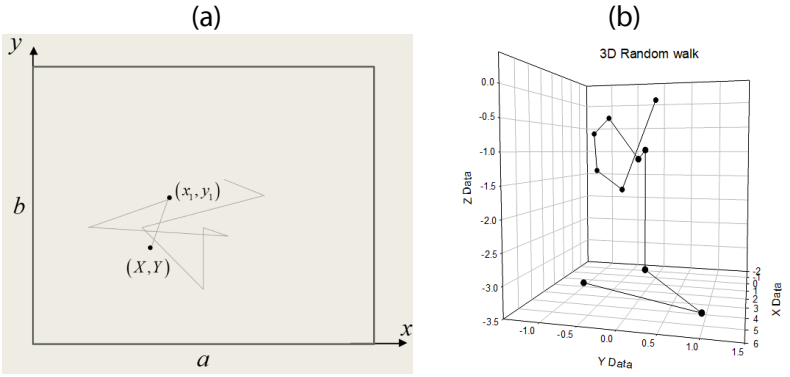

Fig. 2.5: a) random walk of a Brownian particle in 2D; b) random walk of a Brownian particle in 3D.

This method can be generalised to three-dimensional space, by introducing a third dimension and a spherical coordinate system. For the starting point (x_0, y_0, z_0), the final point is $(x_0 + x, y_0 + y, z_0 + z)$, where $(x, y, z) = (d\sin\theta\cos\phi, d\sin\theta\sin\phi, d\cos\theta)$, $\theta = \arccos(1 - 2\xi_1)$, $\phi = 2\pi\xi_2$, $d = -\lambda\ln(\xi_3)$, and ξ refers to uniformly distributed random numbers on the interval [0,1]. Here is an example of Wolfram Mathematica code which generates the 10 random walks presented in Fig. 2.5b:

```
lam=1;
x[0]=0;
y[0]=0;
z[0]=0;
Do[
 d=-lam*Log[RandomReal[]];
 Theta=ArcCos[1-2*RandomReal[]];
   Phi=2*π*RandomReal[];
   x[l]=x[l-1]+d*Sin[Theta]*Cos[Phi];
   y[l]=y[l-1]+d*Sin[Theta]*Sin[Phi];
   z[l]=z[l-1]+d*Cos[Theta];
,{l,1,10}]
Table[{x[l],y[l],z[l]},{l,0,10}]
```

2.2.3. Random numbers

Up to this point we described a three-dimensional random walk of a particle, whose scattering angle is uniformly distributed. In the general case, the first step of Monte Carlo simulations is numerical sampling of random variables from a specified PDF. To do so, we introduced the inverse function method, which is a possible method for PDFs explicitly known and for which the integrals can be solved. Another popular method is the Rejection Sampling method.

Random sampling algorithms are based on the use of random numbers uniformly distributed in the interval [0, 1]. TRUE random numbers cannot be generated from the algorithm process, they should be sampled from some truly random physical process. But for computer-based simulations, pseudo random numbers are in use. Pseudo random numbers are generated from algorithms, and so cannot be true random numbers, since a random variable cannot be obtained from a deterministic algorithm.

It is not possible to distinguish between truly random and pseudo random numbers in terms of the randomness. It is expected that algorithm-generated pseudo random numbers pass all the criteria of the randomness and cannot be distinguished from true random numbers. Here the author quotes Metropolis (1987):

> „How are the various decisions made? To start with, the computer must have a source of uniformly distributed pseudo-random numbers.
>
> A much-used algorithm for generating such numbers is the so-called von Neumann 'middle-square digits.' Here, an arbitrary n-digit integer is squared, creating a 2n-digit product. A new integer is formed by extracting the middle n-digits from the product."

Metropolis described a very simple algorithm for generating random numbers illustrated with following example:

$$123\,456^2 = 15\,\mathbf{241\,383}\,936$$

$$241\,383^2 = 58\,\mathbf{265\,752}\,689$$

$$265\,752^2 = 70\,\mathbf{624\,125}\,504$$

The bold numbers in the middle are random numbers. Generating many of these numbers and scaling them to the [0,1] interval, a sequence of random numbers can be formed. By writing a computer program function, which can return random numbers from that sequence, the function **rand** used in the beginning of this chapter is created. Nowadays advanced algorithms are in use, which ensure that the period of repetition of sequences of random numbers is so large that it cannot be practically exceeded, even for complex simulations.

2.3. Simulation of radiation transport

When simulating radiation transport through an arbitrary medium, the situation is more complicated compared with the random movement of a Brownian particle. Collisions of a Brownian particle were only elastic and scattering was isotropic. When simulating radiation particle transport, interactions can be far more complicated, where in inelastic collisions other radiation particles can emerge. Some interactions are so frequent that collision-by-collision simulations are impractical and impossible to perform. A single interaction of one particle is often referred to as the **event**. The set of all events of one particle is called the **history** of the particle. Simulation of interactions event-by-event of a radiation particle is called **detailed simulation** and codes performing this kind of simulation are called **track structure codes**. In contrast to track structure simulations, in **multiple scattering simulations** a large number of events are condensed into one, called a multiple scattering event.

2.3.1. Detailed methods – Track structure codes

Let us take a look at one general example of a track structure code. The radiation particle is moving through some arbitrary medium and undergoes collisions, which can, in general, be elastic or inelastic. In some cases of inelastic collisions, secondary particles can be created, as in the example shown in Fig. 2.6a, where secondary photons are created. Very often the energy locally deposited in the medium by external radiation is of interest. It is important to note that the energy that the radiation particle (referred to as primary particle) loses locally in the medium is not the same as the energy which is locally deposited. The reason for this is the creation of secondary particles, which can (as in the particular case of secondary photons) travel far from the place of origin and deposit energy elsewhere. This is the reason why secondary particles need to be simulated after the finished

simulation of the primary particle. The simulation of secondary particles is performed in the same manner as the primary one, one by one, until all secondary particles have been processed. This approach allows the exact determination of the energy locally deposited in some region of interest.

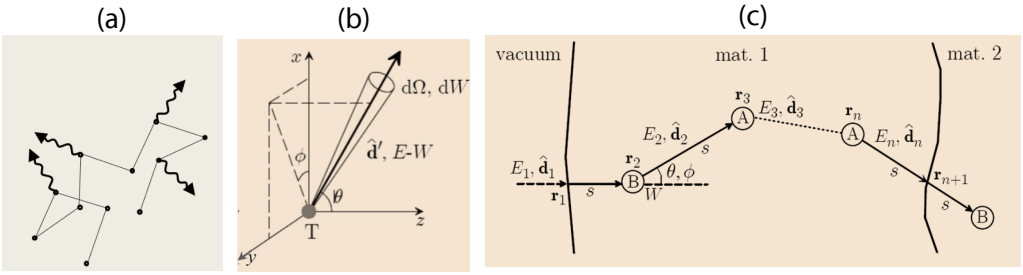

Fig. 2.6: a) secondary photons created in collisional events; b) illustration of a double deferential cross section ; c) particle movement in inhomogeneous media (Salvat F. et al., 2011).

Radiation interacts with a medium through various competing mechanisms. Each interaction event is associated with an appropriate differential cross section (DCS.) Most information on the particle interactions is contained in the double differential cross section

$$\sigma(\Omega,W)=\frac{d^2\sigma}{d\Omega dW}, \tag{2.19}$$

which defines the probability of scattering in some solid angle $d\Omega$, within the energy range dW, as shown in Fig. 2.6b. Taking into account scattering at all angles and energies, a total cross-section can be obtained

$$\sigma=\int_W\int_\Omega \sigma(\Omega,W)\,d\Omega dW, \tag{2.20}$$

The total cross section σ can be related to the mean free path λ for a given medium

$$\lambda=\frac{1}{N\sigma}, \tag{2.21}$$

where N is the number density of atoms or molecules in the medium.

As an example, suppose that the particle can interact via two independent mechanisms A and B, and that their double differential cross sections are

$$\frac{d^2\sigma_A}{d\Omega dW} \text{ and } \frac{d^2\sigma_B}{d\Omega dW}. \tag{2.22}$$

The total cross sections is $\sigma_T=\sigma_A+\sigma_B$, and

$$\lambda_T=\frac{1}{N\sigma_T} \tag{2.23}$$

is total mean free path. It is of interest to define the partial mean free paths

$$\lambda_A = \frac{1}{N\sigma_A} \text{ and } \lambda_B = \frac{1}{N\sigma_B}, \tag{2.24}$$

where the connection to the total mean free path is

$$\frac{1}{\lambda_T} = \frac{1}{\lambda_A} + \frac{1}{\lambda_B}. \tag{2.25}$$

To determine whether event A or B occurs at the end of the total free path, the partial free paths can be sampled independently and the event to occur may be chosen according to the shorter partial free path. It is important to note that the particle travels a distance given by the total free path, while the partial free paths serve for deciding which event occurs at the end of the step.

At this point we can introduce inhomogeneous media. Fig. 2.6c shows an example of a situation in which a particle of radiation enters from vacuum into material 1 and then moves to material 2. When a particle travels through one material, the governing principle is as described above. When a particle crosses the boundary between two media, the particle is "stopped" at the interface between the two, and then new parameters for transport are created according to the properties of the second medium. The transport of the radiation particle in the second medium is further simulated from the interface between the two media, as if it started at that point. This is justified, since radiation transport can be classified as a Markov process, in which the further output doesn't depend on the past history of the particle.

During radiation transport, secondary particles can be created in a collision event and can include photons, electrons, delta rays and other particles. In a detailed simulation, the generated secondary particles are scored, and their properties are stored. Secondary particles are simulated after the simulation of the primary particle (the one that generated the secondaries) and are treated in the same manner as primary one.

2.3.2. Multiple scattering theory

In some cases, detailed simulations using track structure codes are impractical. For example, when simulating the transport of electrons or charged heavy particles, such as protons or alpha particles, the long range of the Coulomb interaction implies that an enormous number of interactions can occur in very small length scales. This kind of simulation would therefore be very demanding on time and computer resources. In such cases multiple scattering codes are employed, which condense many interactions in one artificial event. In the case of simple Brownian motion this can be illustrated as follows:

Let us simulate for instance 8 random free paths from some initial starting point of a Brownian particle. This situation is presented in Fig. 2.7a. Repeating the procedure using different random numbers, we will obtain some other path, as in Fig. 2.7b.

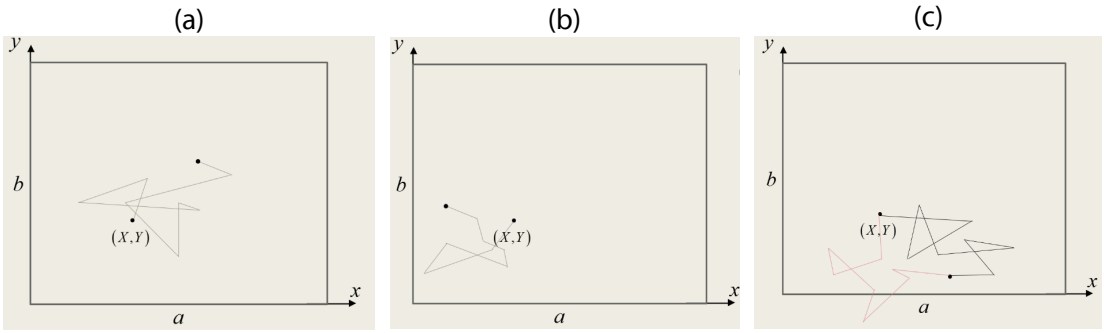

Fig. 2.7: a) randomly sampled path; b) different randomly sampled path; c) drawbacks of multiple scattering theory

This procedure may be repeated many times and the final point after 8 histories scored. The distribution of distance that particle travelled may be determined, and, with sufficient repetitions, a PDF may be obtained which is, for this case, a normal distribution. Now we do not need to use a detailed simulation for finding the distance the Brownian particle travelled after 8 histories. We can use a derived PDF and from it generate random final points. In one step we can move the particle for 8 free step lengths. This is a type of condensed history. The number of 8 can be increased (or decreased) according to the needs of the simulation. However, it must be noted that the more histories we condense, the more information we lose.

To illustrate the loss of information, consider Fig. 2.7c. The particle started from point (X,Y) and its movement after 8 free paths finished in some condensed history-generated end point. For instance, to check whether a particle left the box, using condensed histories, can result in an incorrect answer. The endpoint in Fig. 2.7c suggests that the particle did not leave the box. But if we use the detailed simulation to generate paths, we could obtain a finite probability of the particle leaving the box.

In general, the multiple scattering theory implemented in condensed-history simulations is approximate and may lead to systematic errors (which can be avoided if used with care). For charged particles, multiple scattering theory is a need, rather than a choice, because of the large number of interactions per small track length. Detailed simulation is time consuming, even impossible to perform. Fig. 2.8 illustrates the careful planning of a multiple scattering simulation. The dotted lines represent the real path, while the straight lines represent the multiple scattering simulation.

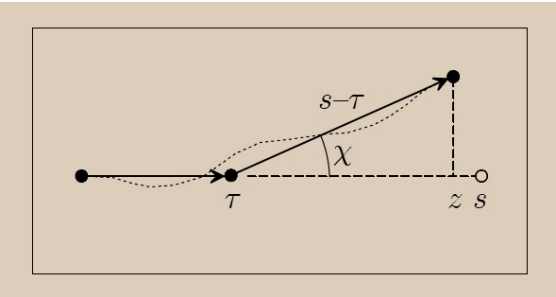

Fig. 2.8: Particle track generated with multiple scattering theory, (Salvat F. et al, 2011)

Finally, let us consider a general algorithm for the simulation of radiation transport. Fig. 2.9 presents such a simplified algorithm, which in general describes the transport of a primary particle along with the secondary ones.

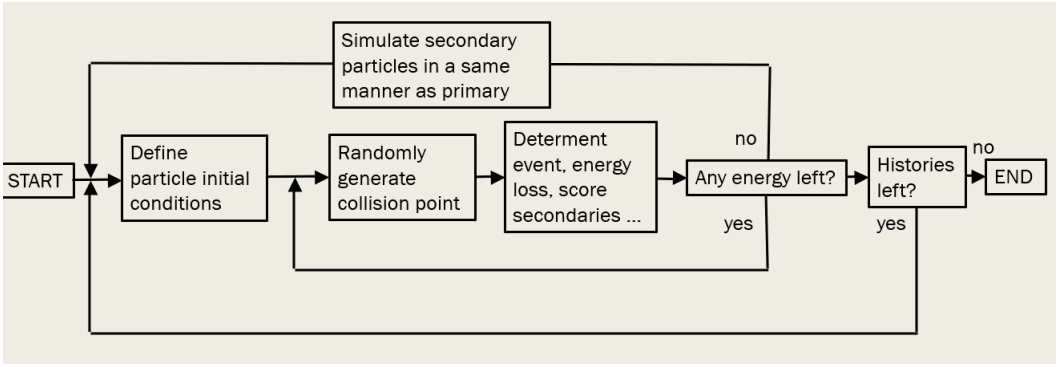

Fig. 2.9: General algorithm of Monte Carlo radiation transport simulation

Fig. 2.9 is a simple summary of MC transport as described in this chapter.

2.4. References

Comte de Buffon, G., 1777. Essai d'arithmetique morale, 4. Supplement a l'Histoire Naturelle.

Laplace, P.S. 1886. Theorie analytique des probabilites, Livre 2. In Oeuvres completes de Laplace, 7, Part 2, 365 - 366. L'academie des Sciences, Paris.

Metropolis N., 1987. "The beginning of the Monte Carlo method", Los Alamos Science Special Issue, 125-130.

Salvat F. et al., 2011. PENELOPE-2011: A Code System for Monte Carlo Simulation of Electron and Photon transport, Workshop proceedings, Barcelona, Spain.

3. On the efficiency of Monte Carlo simulations of radiation transport

Francesc Salvat Pujol, European Organization for Nuclear Research (CERN), Switzerland; **Mihaly Novak**, European Organization for Nuclear Research (CERN), Switzerland; **Susanna Guatelli**, University of Wollongong, Australia

Abstract

Results from Monte Carlo (MC) simulations of radiation transport are affected by statistical uncertainty: a sufficiently large number of primary events must be sampled in order to obtain converged and statistically meaningful estimates of dosimetric quantities. For particularly demanding applications, the CPU time necessary to attain convergence can be prohibitively long, as in problems affected by strong attenuation (e.g., in radiation-shielding design), by a low cross section (e.g., when assessing neutron production in a sufficiently energetic photon field), or in complex geometries (e.g., in detailed voxel geometries for medical applications), etc. In this contribution, the figure of merit customarily employed to quantify the efficiency of MC simulations is discussed, and three approaches are suggested for maximizing it in particularly for CPU-intensive simulations. It is first shown, by way of example, how a basic understanding of the physics governing a given radiation problem and a judicious choice of a few basic simulation parameters can already lead to a drastic enhancement of the simulation efficiency. Next, biasing techniques are introduced, highlighting their potential to further improve the simulation efficiency by orders of magnitude in problems affected by strong attenuation, while stressing the caution to be exercised in their use. Finally, an outlook on attempts exploiting novel machine learning techniques as well as massively parallel computing architectures is presented.

3.1. Introduction

The Monte Carlo (MC) method is the most efficient approach known to-date to address any problem where radiation emanating from a source propagates and interacts with matter to eventually impinge upon a detector, where a dosimetric quantity is measured, such as a particle fluence, dose, or a particle emission spectrum. This family of problems is governed by the Boltzmann transport equation, an integro-differential equation which is solvable analytically in a mere handful of simplified situations: typically for an infinite medium, one (or few) transported particle species, and one (or few) interaction mechanisms (Kase and Zweifel, 1967). While the few known analytical solutions for simplified scenarios play a key role in more complex transport models (e.g., in multiple Coulomb scattering theories), their applicability remains limited. The MC method, instead, tackles the radiation transport problem by sampling an ensemble of particle tracks emanating from a source, driven by a host of radiation-matter interactions with known interaction cross sections, whereby particles may lose energy, change direction, and generate secondary particles, thus giving rise to a radiation shower, leading to material activation with prompt/delayed emission of radiation if hadronic inelastic interactions occur. Accumulating the contribution of every particle step or discrete interaction to the desired physical observables leads to statistical estimates of these quantities. As opposed to more limited analytical approaches, the MC method is naturally extensible to accommodate as many particle species and interaction mechanisms as necessary, providing it with general applicability, to the point that nowadays truly general-purpose codes (CERN, 2023, Ahdida et al., 2022, Battistoni et al., 2015, Agostinelli et al., 2003, Allison et al., 2006, 2016, Sato et al.,

2018, Kulesza et al., 2022, Mokhov, 2016) are readily capable to simulate coupled electromagnetic and hadronic radiation showers in complex material geometries irradiated by photons, leptons, hadrons, and ions in a broad energy range, being able to estimate a large number of physical observables.

MC simulations ultimately evaluate a (consistent and ideally unbiased) statistical estimator f of a physical observable. In view of their stochastic nature, MC estimates are affected by a statistical uncertainty σ which, by virtue of the central limit theorem, scales with the number of simulated primary events N as (Salvat, 2018)

$$\frac{\sigma}{f} \sim \frac{1}{\sqrt{N}}. \tag{3.1}$$

That is, in order to halve the statistical uncertainty in a MC estimate, the number of sampled primary events must be quadrupled. For small N, the value of the statistical estimator f may fluctuate wildly, while for larger N the expectation value of f tends to the average value of the considered physical observable. Numerical experience suggests that the value of f often approaches convergence when the relative uncertainty σ/f drops well below 10% (Werner et al., 2018). The user should adjust the number of primary events N as needed to attain a statistical uncertainty as small as needed.

Needless to say, results from MC simulations are furthermore affected by a systematic error due to the necessary approximations and simplifications underlying the transport and interaction models adopted by a given MC code: their assessment pertains to the domain of code benchmarking and validation against experimental data. Instead, the focus of this contribution is on the statistical uncertainty in results from a MC simulation and, specifically, on how statistical convergence can be accelerated in particularly demanding and CPU-intensive simulations. In section 3.2, a customary figure of merit for the efficiency of a Monte Carlo simulation is briefly discussed. Section 3.3 shows, by way of example, how efficiency can be enhanced by orders of magnitude by a judicious choice of MC simulation parameters, driven by a good understanding of the physics driving the problem. Section 3.4 turns instead to a selection of biasing techniques that can be applied to enhance the simulation efficiency in problems affected by strong attenuation. Finally, an outlook on ongoing attempts to exploit machine learning techniques and highly parallel computing architectures is given in section 3.5.

3.2. Efficiency of a MC estimate

The figure of merit for a MC simulation estimating the value of a physical observable with a statistical estimator f is ordinarily taken as the efficiency ϵ, given by

$$\epsilon = \left(\frac{f}{\sigma}\right)^2 \frac{1}{t}, \tag{2}$$

where σ is the statistical uncertainty and t is the elapsed CPU time. All quantities in the right-hand side are implicit functions of the number of primary events N. However, since in an (unbiased) MC simulation like the one briefly outlined above the CPU time is linearly proportional to the number of primary events,

$$t \sim N, \tag{3}$$

it follows from Eq. 3.1 that the efficiency ϵ is actually independent of N, provided that f is approaching convergence, i.e., $\sigma/f \lesssim 0.1$, otherwise large fluctuations in ϵ can be observed. Thus, for sufficiently large N, the efficiency ϵ is a quantity (with dimensions of inverse time) which measures how effectively a MC estimate f converges towards the value of the considered physical observable for a

given MC simulation algorithm and computer processor. In the following sections, several approaches are presented, all aiming at maximizing ϵ in non-trivial scenarios where f converges slowly (i.e., where convergence would require an N too large and/or a t too long to be practically feasible).

3.3. A basic understanding of the underlying physics as a guide on how to set MC simulation parameters

An obvious and yet at times overlooked resource to enhance the efficiency of a MC simulation consists in having a good understanding of the basic physics governing the radiation problem at hand, which in turn provides solid grounds on which to set the value of various simulation parameters, in order to focus CPU effort where it matters most. Particular attention should be devoted to electromagnetic showers, which are notoriously CPU-intensive: mean free paths for electrons and positrons can easily be shorter than a micrometre and, moreover, every electron, positron, or photon interaction leads to (at least) two emitted particles (with the exception of elastic scattering). Thus, a large number of electrons, positrons, and photons quickly builds up, promptly forming an electromagnetic shower.

MC codes provide algorithms to greatly speed up electron and positron transport (and charged particles in general): multiple Coulomb scattering models allow charged particles to take macroscopic step sizes, accumulating at the end of each step the effect of multiple deflections onto an individual aggregate deflection, normally complemented by a lateral displacement and a path-length correction, while electronic stopping models allow for the accumulated energy loss of a charged particle to be sampled at the end of a macroscopic step, without individually sampling the multiple underlying individual collisions with target electrons. These so-called condensed tracking algorithms expect crucial input from the user: typically, a cutoff scattering angle (above which individual elastic deflections are instead sampled explicitly) and a threshold knock-on electron (delta-ray) production energy (above which knock-on electrons are produced and tracked explicitly). The effect of the latter parameter on the efficiency of a MC simulation is discussed below in detail.

Low values of the delta-ray production threshold E_δ lead to a large number of secondary electrons to be sampled and tracked explicitly, and in turn to a large number of higher-generation secondary electrons and photons, culminating in an exponential growth in the number of particles to track. This leads to a more detailed simulation, at the expense of a rapidly increasing CPU time. Instead, a high value of E_δ will lead to a smaller number of knock-on electrons to be generated and tracked (i.e., a much shorter CPU time), with more energy apportioned along the charged particle step (while knock-on electrons could in principle deposit their energy elsewhere in the geometry). In practice, a balance has to be struck between simulation accuracy and elapsed CPU time. This can be attained by comparing the range of electrons with kinetic energy equal to E_δ with the size of the geometry or the required spatial resolution Δr in scoring grids: for a given Δr, one can set E_δ such that the corresponding electron range is smaller than Δr. In this way, electrons not explicitly tracked would anyway not travel substantially beyond Δr and scored radiometric quantities will retain the requested resolution.

Consider, for example the scoring of the average energy deposition as a function of depth of 150-MeV protons in a cylindrical tank of water of 5 cm radius and 25 cm length. Let the desired spatial resolution be $\Delta r = 0.166$ cm. This problem is driven by the ionization losses of the incoming proton, the rate of which drastically increases as the proton reaches the end of its range, giving rise to the so-called Bragg peak in the proton depth-dose curve, displayed in Fig. 3.1. Protons may undergo a

nuclear inelastic interaction, giving rise to neutrons which will be subsequently tracked and thermalized in water, eventually undergoing a capture reaction with the emission of MeV photons which may contribute to the energy deposition (visible as a dose tail beyond the distal edge of the Bragg peak in the linear scale of Fig. 3.1).

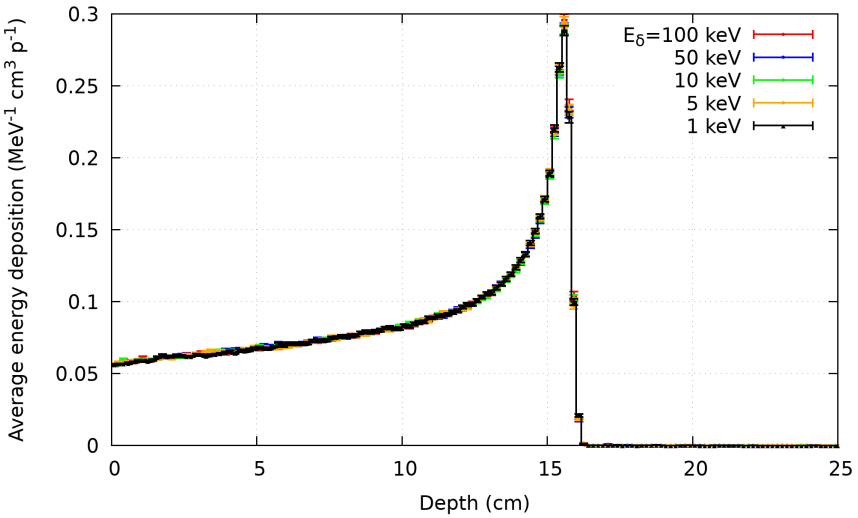

Fig. 3.1: Average energy deposition as a function of depth for 150-MeV protons traversing a cylinder of water (see text) for various values of the delta-ray production threshold.

Since ionization drives this problem, careful attention should be devoted to the treatment of knock-on delta rays. The range of 300 keV electrons in water is ~0.08 cm (about half of the desired resolution). Thus, explicitly tracking lower-energy knock-on electrons will not make an efficient use of CPU time: they would anyway remain within the given $\Delta r = 0.166$ cm with minimum aliasing effects among adjacent bins (a somewhat lower cut-off should be set to minimize these). One can therefore comfortably set a delta-ray production threshold energy as high as $E_\delta = 100 - 200$ keV. Table 3.1 displays, as a function of E_δ, the CPU time needed to simulate (with FLUKA (CERN, 2023, Ahdida et al., 2022, Battistoni et al., 2015)) 8000 primary events for this problem. With $E_\delta = 100$ keV (still much lower than it needs to be), 2.9 seconds execution time suffice to obtain the result using an Intel i9-11900K processor. Lower values of E_δ lead to a drastic increase of the CPU time and a consequent deterioration of the simulation efficiency: $E_\delta = 1$ keV leads to a CPU time of almost an hour, without any tangible benefit in the scored quantity, as can be seen by the identical energy-deposition spectra in Fig. 3.1 for the considered values of E_δ. Consequently, delta-ray production cuts should be carefully set so as to meet the requirements of a given problem, and not much lower, so as to minimize time needlessly wasted in simulating details of the electromagnetic shower that will not be discerned for given spatial resolution requirements.

Another noteworthy parameter is the transport energy (or residual range), below which a particle is no longer tracked: depending on the particle species, various codes opt for depositing energy locally or in an apportioned way as the particle is ranged out. If one is for instance interested in estimating the neutron yield from a spallation target, electron and positron transport can usually be discarded: high transport threshold energies can be prescribed for electrons and positrons, at the benefit of a great reduction in CPU time as elaborated above. Likewise, for the design of the subsequent shielding, special attention should be paid to all processes which contribute to the neutron (down to thermal energies) and photon fluence outside the shielding: electrons and positrons can be

readily discarded well below a few MeV, since they are not expected to substantially emit Bremsstrahlung photons anymore, and charged hadrons below the Coulomb barrier can also be discarded.

Table 3.1: Variation in the CPU time when scoring with FLUKA the energy deposition in a water tank by 150-MeV protons with 8000 primary events (see text for more details). The simulation efficiency, Eq. 3.2, is evaluated for the peak energy deposition value.

E_δ (keV)	CPU time (s)	Efficiency (s^{-1})
100	2.9	2060.7
50	8.1	666.9
10	72.8	94.4
5	175.8	37.4
1	3327.7	2.2

3.4. Biasing techniques

As shown in the foregoing section, a thoughtful choice of MC simulation parameters while considering the basic physics, the dimensions of the scattering geometry, and the resolution of the scoring meshes in a given radiation transport problem pays enormous dividends in terms of spared CPU time. However, there can be scenarios which require further efforts in order to attain reasonably converged MC estimates for the desired physical quantities. For instance, problems driven by a low interaction cross section (e.g., when assessing the production of neutrons as well as material activation under photon irradiation) might require a prohibitively large number of primaries to even begin to sample the relevant events, largely wasting CPU time tracking irrelevant particle histories. Likewise, situations affected by strong attenuation (e.g., in neutron shielding problems) imply that an excessively large number of primary events might need to be sampled in order to to probe the radiation field outside of the shielding region.

To render MC an efficient calculation approach also in such demanding scenarios, a series of methods exist, known as biasing or variance-reduction techniques (García-Pareja et al., 2021). The basic strategy behind any biasing technique consists in applying a distortion of the interaction properties of a given particle (e.g., deliberately shortening its mean free path, forcing scattering preferentially onto a given direction, replacing a particle by many replicas, etc.), accompanied by a corresponding modification in its statistical weight, in such a way that the expectation value of the desired observable is respected. Biasing techniques aim at reducing the variance σ^2 or the simulation time t, in such a way that the simulation efficiency ϵ, Eq. 3.2, is enhanced. In this section, a practical example is discussed which highlights the virtues of biasing techniques, while warning about the care that should be exercised when using them.

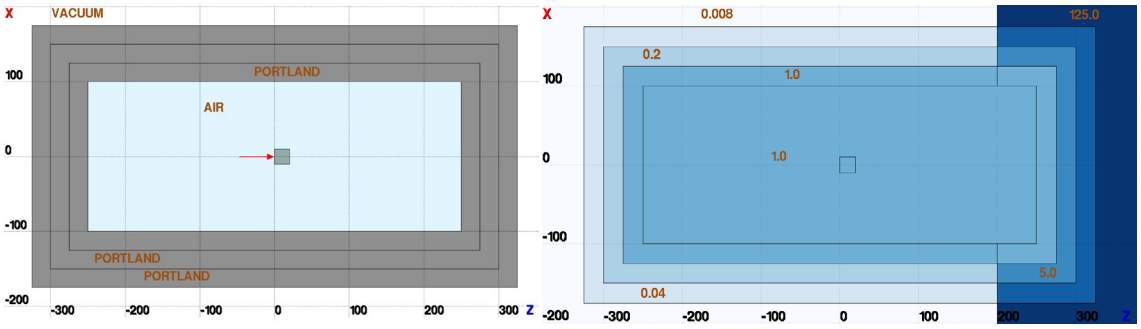

Fig. 3.2: Schematic neutron shielding problem geometry (left, with lengths in cm), region importance assignment (right).

Consider a 500-MeV proton pencil beam emanating from $z = -3$ cm and impinging along the z axis onto the base of a cylindrical tungsten target, surrounded by air and by a coaxial cylindrical layer of concrete, 75 cm thick, as displayed schematically in the left-hand panel of Fig. 3.2, where the red arrow denotes the proton beam impinging on the target. Besides undergoing ionization losses in the material, 500-MeV protons will undergo a nuclear inelastic interaction on average every ~10 cm, whereupon secondary protons, neutrons, possibly heavier nuclear fragments, as well as nuclear de-excitation photons will be emitted. Let the ambient dose equivalent $H^*(10)$ be the quantity to estimate downstream, outside of the shielding. This quantity is typically scored in MC codes by means of fluence-to-dose conversion coefficients. The particle fluence outside of the shielding in this problem is largely due to neutrons and photons, strongly attenuated by the concrete shielding, as displayed in Fig. 3.3. As the neutrons and photons traverse the shielding, their respective population drops exponentially (the shielding works as expected), posing statistical convergence issues on the assessment of $H^*(10)$ outside the shielding: a very low density of particle tracks is observed, as opposed to the dense mapping near the target. The upper row of Fig. 3.4 displays $H^*(10)$, in pSv per primary proton (left), and the statistical uncertainty as a percentage per primary proton (right), both obtained sampling 4000 primary protons. Indeed, in downstream regions outside of the concrete shielding, the statistical uncertainty is nearly 100%, i.e., no statistically meaningful estimate of the ambient dose equivalent can be made with 4000 primaries: a much larger number of primaries would have to be sampled, at a corresponding increase in CPU time.

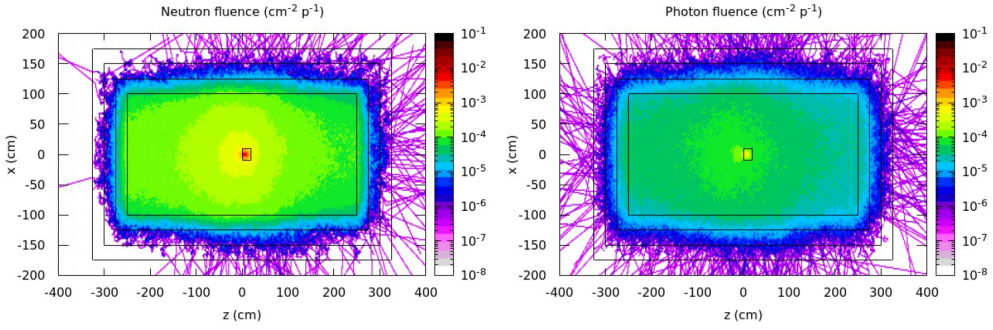

Fig. 3.3: Simulated neutron and photon fluences per primary 500-MeV proton starting at z=-3 cm impinging along the z axis onto the target at the origin of coordinates, scored from 500 primary protons as an example.

Region importance biasing is a technique that is particularly indicated to enhance the simulation efficiency in problems with strong attenuation like the one discussed here. The user assigns a numerical importance to every region in the geometry (higher in regions of interest, lower in less relevant regions). When particles cross a boundary from a region with importance I_1 into a region with a larger importance $I_2 > I_1$, they are split into $\lfloor I_2/I_1 \rfloor$ particles, and their statistical weight is reduced by a factor $\lfloor I_1/I_2 \rfloor$. Conversely, when crossing from a region with importance I_a into a region with lower importance $I_b < I_a$, the Russian roulette technique is applied: particles are discarded with a probability I_b/I_a and their statistical weight is increased by a factor I_a/I_b. A possible choice of importance values in the aforementioned scattering geometry is proposed in the right-hand panel of Fig. 3.2: the target and the surrounding air are given importance 1, as well as the first concrete layer, to ensure that neutrons backscattered from the left to the right are not discarded prematurely. The plane z = 200 cm is intended to effectively separate downstream and upstream sides: importance values are subsequently increased by a factor 5 for downstream regions (where one wishes to score the ambient dose equivalent), and subsequently decreased by the same factor for upstream regions. This scheme has the virtue of strongly suppressing the particle population in the upstream (i.e., left-hand) side of the Fig. 3.2, while enhancing the particle population in the downstream (i.e., right-hand) region, where the ambient dose equivalent is to be scored outside of the shielding. The particle splitting that takes place downstream compensates for the natural attenuation to which neutrons and photons are subject: at every downstream boundary crossing, particles are split into 5 new particles, with a reduction of their statistical weight by a factor 5. As a result, many more particle tracks contribute to the $H^*(10)$ estimate than in an unbiased simulation, allowing the MC estimate to converge much more efficiently.

The lower row of Fig. 3.4 displays the ambient dose equivalent obtained for 4000 primary protons, employing the region-importance biasing scheme detailed above. Whereas the unbiased simulation

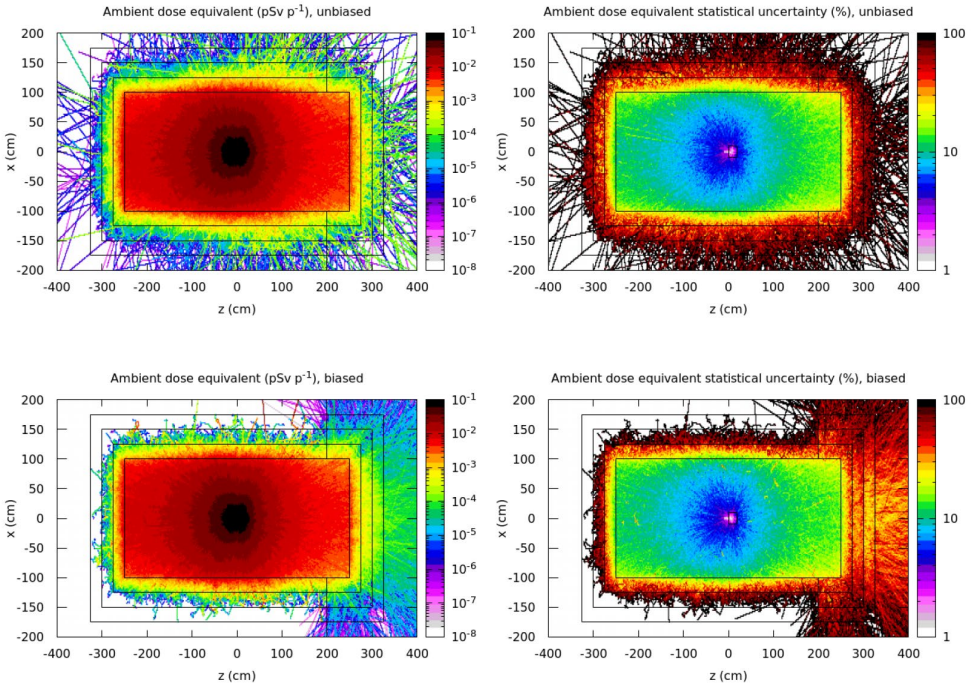

Fig. 3.4: Ambient dose equivalent *(10) (left column) and statistical uncertainty (right column), scored in an unbiased (upper row) and in a biased (lower row) MC simulation with 4000 primaries for the scenario described in the text.

exhibited an uncertainty of 100% outside the shielding, one now obtains estimates with a few 10% uncertainty, well on their way to convergence. While in general the CPU time per primary in a biased simulation may generally differ with respect to that of an unbiased simulation (and possibly even increase), in this particular example the CPU time was ~ 40 seconds for both. The simulation efficiency, however, increases by an order of magnitude, as reported in Table 3.2, thus making a better use of CPU time than an unbiased MC simulation towards statistical convergence of $H^*(10)$. Note however that the evaluation of the efficiency for the unbiased simulation is problematic due to the large statistical uncertainty.

Table 3.2: CPU time comparison for the biased and unbiased shielding calculation described in the text, as well as simulation efficiency for the ambient dose outside the shielding with lowest statistical uncertainty. The estimate without biasing may fluctuate wildly due to the large statistical uncertainty.

Biasing	CPU time (s)	Efficiency $(\mathbf{s^{-1}})$
Off	40.1	0.04
On	41.5	0.63

Further enhancements in the simulation efficiency can be attained by more intensive biasing: segmenting the concrete layers in further coaxial shells allows one to further split particles towards the downstream exit of the shielding. However, a word of caution is in order. When using any biasing technique, simulation effort is sacrificed in some regions of phase space (particle positions and momenta) in favour of other regions. If there is a region of phase space which contributes to the desired observable that is effectively suppressed by a too aggressive biasing, simulation results can be erroneous, in spite of having attained statistical convergence in a very efficient way (Ferrari et al., 2002). Unfortunately, general-purpose MC codes cannot protect against this kind of faux pas: it remains the user's responsibility to employ biasing techniques with due care. Therefore, it is recommended to verify the correct calculation of physical quantities of interest of the biased simulation against the unbiased case and/or validate its results against available experimental measurements. Finally, it is worth noting that if one wishes to simulate situations where space and time correlations matter, biasing should be avoided: indeed, Russian roulette discards particles, leading to the effective loss of correlations in particle showers (note however that MCNP allows for properly correlated biased simulations).

3.5. Parallel computing paradigms and machine learning applications

While the strategies discussed above are well established approaches to drastically enhance the efficiency of MC simulations, further increases in the simulation efficiency can be attained by running distributed or (to a certain degree) parallel MC simulation jobs. Contemporary efforts are devoted to using highly parallel computing architectures to enhance the efficiency of MC simulations in demanding applications, as well to exploring machine learning applications as part of the MC simulation workflow. A very general outlook on a selection of ongoing research projects in these domains is provided here.

MC simulations are naturally distributed computations: n instances of the same simulation can be launched (each with different seed values to initialize the internal random-number generator), and

their results can be readily merged into common statistical estimators. Computer clusters can therefore be exploited without changing a single line of MC code. The simulation efficiency naturally increases by a factor n (at the expense of more power consumption). One may however quickly run out of computer memory, particularly when trying to exploit multiple cores/threads in a single computing node, e.g., in simulations with complex geometries and involved regions, when detailed low-energy neutron cross sections for many isotopes should be loaded (these are in the form of evaluated nuclear data tabulations), large fine-grained scoring grids, etc. For these situations, some MC codes allow the possibility of running simulations with a further degree of parallelization, mostly focusing on sharing memory for geometry and cross section data (but relying on one copy of every scoring per simulation instance) (Allison et al., 2016).

It is problematic to properly exploit massively parallel computing paradigms for MC simulations to the degree in which they can be used for many other problems in physics and mathematics which eventually lead to a linear algebra problem like matrix diagonalization, where multiple threads can be launched, sharing equal workload, performing identical operations (effectively on various corners of the matrix), and advancing towards the problem solution with minimal waste of time, resources, and synchronization overheads. Instead, MC simulations suffer (from the parallel computing point of view) from thread divergence: simulated particle histories can be radically different from each other. The fact that MC simulations access memory in a non-contiguous manner also poses difficulties. These aspects make makes load balancing and synchronization a far from trivial matter when attempting massively parallel MC simulations.

Although requiring considerable code rewriting and often simplified material geometries and radiation-matter interaction physics, several remarkable research and development projects are ongoing, aiming at the exploitation of graphical processing units (GPUs) for MC simulations. These tools typically aim at the parallel processing of many particle histories at the same time, where the effort is focused on a proper workload balancing. Particularly interesting is MPEXS-DNA (Okada et al., 2019), a GPU-based simulator for the modelling of low energy particle interactions and radiolysis, for biomedical applications, claiming further orders of magnitude enhancement in the simulation efficiency (for a reduced interaction physics list and simplified geometry). In the high-energy-physics domain, several projects are ongoing in an attempt to enhance the simulation efficiency where it suffers most: during electromagnetic showers and in complex geometries. Most noteworthy in this activity are the Celeritas (Tognini et al., 2021) and AdePT (https://geant4.web.cern.ch/node/1903) projects, aiming at recasting high-energy-particle transport in a form amenable for treatment with GPUs.

Finally, artificial intelligence has found several interesting applications in internal radiation dosimetry, including the use of convolutional neural networks for dose estimation in radiation therapy and imaging, dose denoising from low-statistics MC estimates, detector modelling, event selection, phase space modelling with generative models, etc. (Sarrut et al., 2021). While deep learning can in many ways complement and improve the performance of MC simulations, and partly replace them, quoting Sarrut et al. (2021): "for the moment, even if it is envisioned that deep learning can improve simulations, it does not seem certain that it can always replace Monte Carlo".

3.6. Conclusions

The efficiency of a Monte Carlo simulation of radiation transport has been introduced as a figure of merit to measure how well simulation effort is spent towards convergence of statistical estimators for desired physical quantities. Several approaches have been considered to maximize the

simulation efficiency in particularly demanding scenarios. First and foremost, a reasonable setting of simulation parameters based on a good understanding of the physics governing a given radiation problem is seen to lead to orders-of-magnitude enhancements (or needless deterioration if set improperly) of the simulation efficiency. Next, biasing techniques have been introduced by way of a shielding example as natural methods to enhance the simulation efficiency by orders of magnitude, while highlighting possible pitfalls. Finally, an overview into parallelization schemes has been given, and an outlook on novel machine learning applications has been briefly presented.

3.7. References

Case, K.M., Zweifel, P.F., 1967. Linear Transport Theory. Addison-Wesley Publishing Company.

CERN, 2023. The Official CERN FLUKA website, https://fluka.cern (accessed 26 October 2023).

Ahdida, C., Bozzato, D., Calzolari, D., Cerutti, F., Charitonidis, N., Cimmino, A., Coronetti, A., D'Allessandro, G.L., Donadon Servelle, A., Esposito, L.S., et al., 2022. New Capabilities of the FLUKA Multi-Purpose Code. Frontiers in Physics, 9, 788253.

Battistoni, G., Boehlen, T., Cerutti, F., Chin, P.W., Esposito, L.S., Fassò, A., Ferrari, A., Lechner, A., Empl, A., Mairani, A., et al., 2015. Overview of the FLUKA code. Annals of Nuclear Energy, 82, 10-18.

Agostinelli, S., Allison, J., Amako., K., et al., 2003. Geant4—a simulation toolkit. Nuclear Instruments and Methods in Physics Research A, 506, 250-303.

Allison, J., Amako, K., Apostolakis, J., Araujo, H., Arce Dubois, P., Asai, M., Barrand, G., Capra, R., Chauvie, S., Chytracek, R., et al., 2006. Geant4 developments and applications. IEEE Transactions on Nuclear Science 53, 270-278.

Allison, J., Amako, K., Apostolakis, J., Arce, P., Asai, M., Aso, T., Bagli, E., Bagulya, A., Banerjee, S., Barrand, G., et al., 2016. Recent developments in GEANT4. Nuclear Instruments and Methods in Physics Research Section A: Accelerators, Spectrometers, Detectors and Associated Equipment, 835, 186-225.

Sato, T., Iwamoto, Y., Hashimoto, S., Ogawa, T., Furuta, T., Abe, S.-I., Kai, T., Tsai, P.E., Matsuda, N., Iwase, H., et al., 2018. Features of Particle and Heavy Ion Transport code System (PHITS) version 3.02. Journal of Nuclear Science and Technology, 55, 684. doi: 10.1080/00223131.2017.1419890.

J.A., Kulesza, Adams, T.R., Armstrong, J.C., Bolding, S.R., Brown, F.B., Bull, J.S., Burke, T.P., Clark, A.R., Forster, R.A., Giron, J.F., et al., 2022. Tech. Rep. LA-UR-22-30006, Rev. 1, Los Alamos National Laboratory, Los Alamos, NM, USA, https://www.osti.gov/biblio/1889957.

Mokhov, N., 2016. Mars15, version 00 (2016), https://www.osti.gov/biblio/1282121.

Salvat, F., 2018. PENELOPE-2018: A Code System for Monte Carlo Simulation of Electron and Photon Transport.

Werner, C.J., Bull, J.S., Solomon, C.J., Brown, F.B., McKinney, G.W., Rising, M.E., Dixon, D.A., Matz, R.L., Hughes, H.G., Cox, L.J., et al., 2018. Tech. Rep. LA-UR-18-20808, Los Alamos National Laboratory, Los Alamos, NM, USA.

García-Pareja, S., Lallena, A.M., Salvat, F., 2021. Variance-reduction methods for Monte Carlo simulation of radiation transport. Frontiers in Physics, 9, 718873.

Ferrari, A., Rubbia, C., Vlachoudis, V., 2002. A Comprehensive Study of the nTOF Background at CERN. Report CERN SL-2002-01-ECT.

Okada, S., Murakami, K., Incerti, S., Amako, K., Sasaki, T., 2019. MPEXS-DNA, a new GPU-based Monte Carlo simulator for track structures and radiation chemistry at subcellular scale. Medical Physics, 46, 1483. doi: 10.1002/mp.13370.

Sarrut, D., Etxebeste, A., Muñoz, E., Krah, N., Létang, J.M., 2021. Artificial Intelligence for Monte Carlo Simulation in Medical Physics. Frontiers in Physics, 9, 738112.

Tognini, S.C., Canal, P., Evans, T.M., Lima, G., Lund, A.L., Johnson, S.R., Jun, S.Y., Pascuzzi, V.R., Romano, P.K., 2021. Celeritas: GPU-accelerated particle transport for detector simulation in High Energy Physics experiments. in: Proc. Snowmass 2021. arXiv:2203.09467 [physics.data-an]. doi: 10.48550/arXiv.2203.09467.

4. Implementation of ICRP computational reference phantoms in different exposure scenarios

Maria Zankl, Helmholtz Zentrum München German Research Centre for Environmental Health (HMGU), Germany; **Jonathan Eakins**, Public Health England (PHE), UK; **José-María Gómez Ros**, CIEMAT – Centro de Investigaciones Energéticas, Medioambientales y Tecnológicas, Spain; **Christelle Huet**, Institut de Radioprotection et de Sûreté Nucléaire (IRSN), France; **Jan Jansen**, Public Health England (PHE), UK; **Montserrat Moraleda**, CIEMAT – Centro de Investigaciones Energéticas, Medioambientales y Tecnológicas, Spain; **Lara Struelens**, SCK CEN – Belgian Nuclear Research Centre, Belgium; **Tomas Vrba**, Czech Technical University in Prague, Czech Republic

Abstract

Working Group 6 "Computational Dosimetry" of the European Radiation Dosimetry Group, EURADOS, has organized an intercomparison study on the usage of the ICRP/ICRU voxel reference computational phantoms together with radiation transport codes. Voluntary participants have been invited to solve specific tasks and provide solutions to the organizers before a certain deadline. The tasks to be solved are of practical interest in occupational, environmental and medical dosimetry. The aims of this training activity were to investigate if the phantoms have been correctly implemented in the radiation transport codes and to give the participants the opportunity to check their own calculations against quality-assured master solutions and improve their approach, if needed. The results of the comparisons were published in a series of articles in a virtual special issue of Radiation Measurements.

4.1. Introduction

Most radiation transport codes are rather complex, and hence many users are applying them as "black boxes", sometimes failing to realize whether the parameters chosen are indeed suitable for the tasks to be solved. This is one of the reasons why EURADOS aims at improving this situation by organizing intercomparison studies (Broggio et al., 2012; Gómez-Ros et al., 2008; Gualdrini et al., 2005; Price et al., 2006; Siebert et al., 2006; Tanner et al., 2004; Vrba et al., 2015; Vrba et al., 2014), in which participants are invited to solve proposed computational tasks. Thus, they can check their results against quality-assured so-called "master solutions" provided by EURADOS.

EURADOS Working Group 6 "Computational Dosimetry" recently organized an intercomparison study on the usage of the ICRP/ICRU adult reference computational phantoms (ICRP, 2009). The exercise aimed to investigate whether participants were able to correctly combine the phantoms with the radiation transport codes used, and if they were able to correctly apply ICRP guidance on the evaluation of specific dosimetric quantities such as organ absorbed and/or equivalent dose and effective dose (ICRP, 2007). The purpose of this article is to characterize the reference phantoms (especially features of the skeleton relevant for bone marrow dosimetry), describe the general aspects of the intercomparison exercise and summarize problems that occurred during the exercise – both on the side of the organizers and on the side of the participants.

4.2. Reference computational phantoms

4.2.1. General characterization

The phantoms employed for the exercise are the male and female adult reference computational phantoms as described in ICRP Publication 110 (ICRP, 2009). The phantoms are based on the voxel models "Golem" (Zankl and Wittmann, 2001) and "Laura" (Zankl et al., 2005), which are in turn based on medical image data of real people whose body height and mass resembled the reference anatomical and physiological parameters for both male and female subjects given in Publication 89 (ICRP, 2002). For construction of the reference phantoms, several modification steps were applied to the segmented phantoms Golem and Laura. These were:

- voxel scaling to match reference height and reference skeleton mass;
- inclusion of further anatomical details, such as a greater number of blood vessels, bronchi, and lymphatic nodes;
- sub-segmentation of the skeleton;
- matching the organ masses of both models to the ICRP data on the adult Reference Male and Reference Female without compromising their anatomic realism;
- adjusting the whole-body masses to 73 and 60 kg for the male and female reference computational phantoms, respectively, by "wrapping" the body with additional layers of adipose tissue.

The phantoms can be downloaded from the ICRP Publications website (https://journals.sagepub.com/doi/suppl/10.1177/ANIB_39_2).

4.2.2. Features of the skeleton

The following radiation-sensitive tissues are located in the skeleton: There is first the red – or active – bone marrow (RBM) located in the marrow cavities. Second, there is the endosteum, also called "bone surface" or "shallow marrow". This is a 50 µm thick layer and covers the surfaces of the bone trabeculae and the cortical surfaces of the medullary cavities in the shafts of all long bones.

The resolution of these tissues is much finer than the voxel resolution. This can be seen in Fig. 4.1 on the left side. There, the fine structure of the bone trabeculae and marrow cavities is shown. It can be seen that the appearance of this structure is like a sponge, and this gives the name to this part of the bone: "spongious bone" or "spongiosa". One can also clearly see that this fine structure cannot be represented on a voxel scale. Therefore, these objects had to be accommodated in the bones at macroscopic level in the homogeneous spongiosa.

In ICRP Publication 70 (ICRP, 1995), the red or active bone marrow content and the marrow cellularity are given for 19 bones and bone groups. The marrow cellularity gives the percentage of marrow in a bone that is still haematopoietically active. From this number the inactive marrow amount can also be assessed for all bones where the cellularity is non-zero. Thus, the entire marrow volume could be assessed for most bones. This marrow volume constitutes one part of the spongiosa volume; and the rest is contributed by the bone trabeculae. This gives a unique bone-dependent relative mixture for the spongiosa part of each of the bone groups. This mixture reflects the amount of active marrow (AM) and inactive marrow and the trabecular bone. On macroscopic level this is realized by the fact that the composition of the homogeneous spongiosa volume is different for different bones.

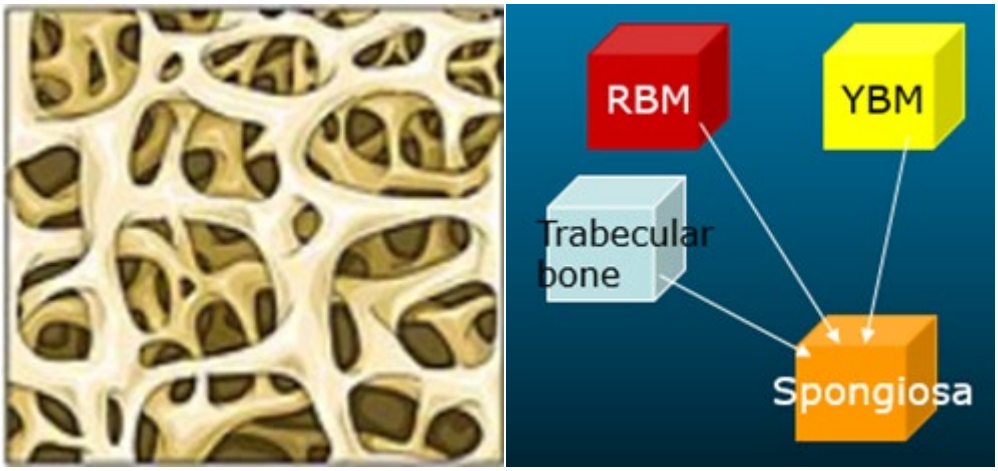

Fig. 4.1: Left: microscopic structure of trabecular bone (from https://en.wikipedia.org/wiki/Trabecula); right: three components making up the spongiosa composition (RBM: red bone marrow, YBM: yellow bone marrow).

4.3. Bone marrow dosimetry (as recommended by ICRP)

4.3.1. Electrons

For electrons as directly ionizing radiation, the method is rather straightforward. Here energy is deposited rather homogeneously in the spongiosa region, and therefore doses to active marrow and endosteum are reasonably approximated by the mean spongiosa doses. Hence, the absorbed dose to active marrow or endosteum in bone site x is estimated as the mean spongiosa absorbed dose in this bone site.

$$D(r_T, x) = D(SP, x) \tag{4.1}$$

Here, $D(r_T,x)$ is the dose to 'target' region r_T in bone site x, with r_T either active marrow, AM, or endosteum, TM_{50}, $D(SP,x)$ is the mean dose to spongiosa of bone site x, and x is one of the 19 distinct bones and bone groups defined within the skeleton.

As already mentioned above, the composition of each spongiosa site has bone-specific relative amounts of active/inactive marrow, endosteum and trabecular bone and, hence, a specific elemental composition. Therefore, it is necessary to evaluate the radiation transport and the energy depositions in each spongiosa site separately. The dose to the target regions in the whole skeleton is then evaluated as a mass-averaged dose to the spongiosa-site specific target region doses:

$$D_{skel}(AM) = \Sigma_x \frac{m(AM,x)}{m(AM)} D(SP, x) \tag{4.2}$$

Here, $D_{skel}(AM)$ is the dose to active marrow in the entire skeleton, $m(AM,x)$ is the active marrow mass in bone site x, and $m(AM)$ is the mass of active marrow in the entire skeleton. For the endosteum, there is an additional contribution from the medullary cavities in the shafts of the long bones:

$$D_{skel}(TM_{50}) = \Sigma_x \frac{m(TM_{50},x)}{m(TM_{50})} D(SP, x) + \Sigma_x \frac{m(TM_{50},x)}{m(TM_{50})} D(MM, x) \tag{4.3}$$

where $D_{skel}(TM_{50})$ is the dose to endosteum in the entire skeleton, $m(TM_{50},x)$ is the endosteum mass in bone site x, $m(TM_{50})$ is the endosteum mass in the entire skeleton, and $D(MM,x)$ is the dose to the medullary marrow in bone site x.

For active marrow, there is no dose contribution from the medullary cavities in the shafts of the long bones, since these do not contain active marrow in the adult reference computational phantoms.

The masses of active/inactive marrow and endosteum of all 19 bones and bone groups are given in Table 4.2 of ICRP Publication 110 (ICRP, 2009), and the elemental compositions of all spongiosa sites are given in Tables B.1 and B.2 of that same ICRP Publication.

4.3.2. Photons and neutrons

For photons and neutrons as indirectly ionizing radiations, the method is different. Here one has to consider that there are energy ranges in which no secondary charged-particle equilibrium exists between the marrow cavities and trabecular bone. During photon irradiation of spongiosa at energies below ~200 keV, there is a greater number of photo-electric events in the denser bone trabeculae than in the less dense marrow tissues. Consequently, the absorbed dose to both active marrow and endosteum is enhanced due to secondary electrons that are generated in bone trabeculae and deposit energy in adjacent marrow tissues (Johnson et al., 2011). Furthermore, the dose enhancement to endosteum is more pronounced than that to active marrow because of its smaller 50 µm thickness and closer proximity to the bone trabeculae surfaces. For neutrons at energies below ~150 MeV, on the other hand, elastic and inelastic collisions in spongiosa result in a greater number of recoil protons generated in the marrow tissues than in the bone trabeculae, due to the higher hydrogen content of marrow, and many of these recoil particles traverse the marrow spaces and deposit their residual energy to surrounding trabeculae. The net result for neutron irradiation over large energy ranges is then a suppression of the absorbed dose to marrow tissues in comparison with that predicted by assuming a kerma approximation (Bahadori et al., 2011; Kerr and Eckerman, 1985).

These effects are reflected in a specific method for bone dosimetry. This has been developed and introduced in ICRP Publication 116 (ICRP, 2010). The method is based on bone- and energy-specific fluence-to-dose response functions for photons and neutrons. The absorbed dose to the active marrow or endosteum in a specific bone site is then determined as the integral of the bone-specific energy-dependent particle fluence multiplied with a bone-specific energy-dependent dose-response function:

$$D(r_T, x) = \int \Phi(E, r_S, x) R(r_T \leftarrow r_S, x, E) dE \tag{4.4}$$

where $D(r_T,x)$ is the absorbed dose to tissue r_T in bone site x, $\Phi(E, r_S, x)$ is the energy dependent photon or neutron fluence through source region r_S in bone site x, and $R(r_T \leftarrow r_S, x, E)$ is the bone-specific energy dependent dose response function.

The dose-response functions are different for photons and neutrons. Again, the skeletal-averaged absorbed dose is then evaluated as the mass-weighted average of the absorbed doses in the individual bones:

$$D_{skel}(r_T) = \Sigma_x \frac{m(r_T,x)}{m(r_T)} D(r_T, x) \tag{4.5}$$

where $D_{skel}(r_T)$ is the dose to target region r_T in the entire skeleton, $m(r_T, x)$ is the mass of target region r_T in bone site x, and $m(r_T)$ is the mass of target region r_T in the entire skeleton. The target region r_T is either active marrow, AM, or endosteum, TM_{50}. For active marrow, the sum over all bone sites x encompasses all spongiosa regions; for the endosteum, additionally the medullary cavities in the shafts of the long bones have to be considered.

The bone-specific dose-response functions for photons and neutrons have been tabulated in ICRP Publication 116 (ICRP, 2010).

4.4. EURADOS intercomparison exercise

In this intercomparison exercise, the ICRP adult reference computational phantoms were simulated in a variety of exposure scenarios. These scenarios were the following:

- A cobalt-60 point source in front of the phantom,
- a 10 keV neutron point source at the same position,
- ground contamination with Am-241,
- exposure in a N-16 cloud,
- two common x-ray examinations, namely chest PA and abdomen AP, and
- internal dosimetry. Here monenergetic photons, monoenergetic electrons and two specific radionuclides were considered for four frequent source organs and six target organs.

One main purpose of the intercomparison exercise was to find out if participants were able to correctly combine the ICRP/ICRU reference computational phantoms with their radiation transport programs. A further aim was to examine their understanding of a series of dose quantities, namely organ absorbed dose, organ absorbed dose rate, effective dose, and – for internal dosimetry – absorbed fractions, specific absorbed fractions and S-values. Furthermore, it should be tested if users were able to apply the methods for red bone marrow dosimetry as recommended by the ICRP, and finally their understanding of specific normalization quantities, such as air kerma free in air, kerma-area product and activity concentration, should be examined.

4.4.1. Approach chosen

Each task was supervised by a member of EURADOS Working Group 6. The responsible person established a master solution, the correctness of which was confirmed by second and sometimes third calculations by other members supporting the task.

When all master solutions had been confirmed, the task specifications were announced on the EURADOS website and distributed to several mailing lists. Through these channels, participants were invited to solve one or several tasks. This selection varied due to the knowledge and interest of the participants, and of course also due to the time that they could devote to the participation.

The task leaders provided templates for each task in the form of EXCEL sheets in which the solutions should be entered. This facilitated the evaluation of the results, since this is much easier when all solutions have the same structure and format. These templates had to be sent to the responsible person of each task.

Each task leader evaluated the participants' solutions and provided feedback to the participants concerning the degree to which their solution agreed or disagreed with the master solution. In case of larger discrepancies, the participants were also encouraged to provide revised solutions.

Furthermore, the different tasks, their master solutions and the solutions provided were to be published in a literature journal, and the participants were invited to co-author the respective publications. After completion of the exercise, the results were published in a series of articles in a virtual special issue of Radiation Measurements, (Eakins et al., 2021; Gómez-Ros et al., 2021; Huet et al., 2022; Rabus et al., 2022; Zankl et al., 2021a; Zankl et al., 2021b; Zankl et al., 2021c).

4.4.2. Participation

Concerning participation, the intercomparison exercise was obviously well-received by the computational community: 32 participants or teams from 17 countries solved at least one of the tasks, and some participants solved several or even all tasks.

The following Monte Carlo codes were used: FLUKA, Geant4, codes from the MCNP family, PenEasy, TRIPOLI and VirtualMonteCarlo.

4.4.3. Solutions

The agreement of the initial solutions with the master solutions was very variable. Some initial solutions agreed within a few percent. On the other hand, there were also many deviations by factors or even orders of magnitude.

Many problems could be solved by feedback between the participants and the responsible person of each task. The initial errors were mainly due to a variety of reasons, including simple carelessness, misunderstandings concerning the normalization quantities, lacking knowledge of dose quantities, such as for example effective dose, and quite often lacking knowledge of the bone dosimetry methods recommended by ICRP.

If revised solutions were provided, these were in most cases in much better agreement with the master solutions. Unfortunately, however, this was not always the case. Sometimes a revision was better in some aspects and worse in others.

4.4.4. Problems

There were two sources of problems – first, on the side of the organizers, and second, on the side of the participants.

On the side of the organizers, there were problems with the task specifications and the timetable:

- For the two tasks involving point sources, the source definition was given in relation to the phantom (e.g., "1 meter in front of the phantom"), without detailing if this was meant to be in front of the skin or in front of the phantom array.
- The internal dosimetry task had several weaknesses: First of all, it was too extensive, leading to issues with the evaluation of the solutions and thus feedback times. Second, source and target organ pairs were partly too distant from each other, leading to issues with computation times and/or statistical uncertainties.
- Due to the complexity of some of the tasks, the planned timetable was too ambitious. First, there were deadline extensions necessary due to an initially weak participation. Second, in some cases, the feedback to participants was also delayed, leading to issues with the follow-up of abnormal results, since participants did not exactly remember their procedures. Third, the total duration of the exercise was finally longer than the time interval that a junior researcher typically stays at a given institute, leading to issues with the follow-up of abnormal results due to the change of personnel.

The problems with the solutions provided by the participants were the following:

For some of the solutions one could clearly see that obviously no reasonable quality control had been performed. Here are a few examples:

- There were several situations where more or less simple plausibility considerations would have helped to identify wrong results. For example, exposure to ground contamination is a rather homogeneous exposure condition. This means that all organ doses should have a similar magnitude, and extreme outliers must be wrong.
- When there are values to be evaluated for several energies, it can be expected that results for intermediate energies are not entirely outside the range of the values for all other energies.
- Furthermore, for many of the tasks, there are similar values available in the literature, even if the situations are not exactly the same. When the exposure situation is rather similar, then also the magnitude of results can be expected to be similar. The possibility of such comparisons with literature values was also neglected by several participants. Otherwise they would have realized that their results have a wrong magnitude.

There was also another quite different problem: Some participants provided revised results, but they did not disclose what they had changed in the computational procedure to arrive at the corrected values. This makes it impossible to judge if the measures that they have applied are appropriate.

This means also that the reasons for the initially wrong results remain unclear. Thus, no additional insights can be gained that could be given as hints to other participants. These might either be participants in the same exercise or participants in future similar exercises who might make the same sort of mistakes.

4.5. Conclusions

EURADOS carried out an intercomparison exercise with different tasks. These describe exposure situations of practical interest in medical physics, occupational and environmental radiation protection. The correct simulation of the proposed tasks requires knowledge of the physical quantities involved and the ability to combine the IRCP/ICRU reference phantoms correctly with radiation transport codes.

The main scope of the intercomparison exercise was to offer an open forum for discussion and training in the field of computational dosimetry.

In some cases, no knowledge about potential misunderstandings could be gained, since the participants did not disclose how they improved their computational procedure. Sometimes, a lack of awareness was found of the necessity for quality assurance of computational results. This means that sometimes simple plausibility checks were not performed, and comparisons with available literature data of similar conditions were not made.

Nevertheless, it can be said that such studies are in principle quite beneficial to the field of computational dosimetry. First, there is the possibility of direct training of participants through feedback with the task organizers. Second, the publication of the task results leads to the availability of additional representative dose values for a variety of exposure conditions. This may aid future novice users in the quality assurance of their methods.

4.6. References

Bahadori, A.A., Johnson, P., Jokisch, D.W., Eckerman, K.F., Bolch, W.E., 2011. Response functions for computing absorbed dose to skeletal tissues from neutron irradiation. Physics in Medicine and Biology, 56(21), 6873.

Broggio, D., Bento, J., Caldeira, M., Cardenas-Mendez, E., Farah, J., Fonseca, T., Konvalinka, C., Liu, L., Perez, B., Capello, K., Cowan, P., Cruzate, J.A., Freire, L., Gómez-Ros, J.M., Gossio, S., Heide, B., Huikari, J., Hunt, J., Kinase, S., Kramer, G.H., Kurihara, O., Kyrieleis, A., Lebacq, A.L., Leone, D., Li, C., Li, J., Mihailescu, L.C., Moraleda, M., Navarro, J.F., Oliveira, C., Puerta, N., Reichelt, U., Simões, C., Sommer, D., Takahashi, M., Teles, P., Vanhavere, F., Vrba, T., Franck, D., Gualdrini, G., Lopez, M.A., 2012. Monte Carlo modelling for the in vivo lung monitoring of enriched uranium: Results of an international comparison. Radiation Measurements, 47(7), 492-500.

Eakins, J., Huet, C., Brkić, H., Capello, K., Desorgher, L., Epstein, L., Hunt, J.G., Kim, H.S., Krstic, D., Lee, Y.K., Manohari, M., Nikezic, D., Shukrun, R.H., Souza-Santos, D., Tymińska, K., 2021. Monte Carlo calculation of organ and effective dose rates from ground contaminated by Am-241: Results of an international intercomparison exercise. Radiation Measurements, 148, 106649.

Gómez-Ros, J.M., Carlan, L.d., Franck, D., Gualdrini, G., Lis, M., A.M., L., Moraleda, M., Zankl, M., Badal, A., Capello, K., Cowan, P., Ferrari, P., Heide, B., Henniger, J., Hooley, V., Hunt, J., Kinase, S., Kramer, G.H., Löhnert, D., Lucas, S., Nuttens, V., Packer, L.W., Reichelt, U., Vrba, T., Sempau, J., Zhang, B., 2008. Monte Carlo modelling of Germanium detectors for the measurement of low energy photons in internal dosimetry: results of an international comparison. Radiation Measurements, 43(2-6), 510-515.

Gómez-Ros, J.M., Moraleda, M., Arce, P., Bui, D.-K., Dang, T.-M.-L., Desorgher, L., Kim, H.S., Krstic, D., Kuć, M., Le, N.-T., Lee, Y.-K., Nguyen, N.-Q., Nikezic, D., Tymińska, K., Vrba, T., 2021. Monte Carlo calculation of the organ equivalent dose and effective dose due to immersion in a 16N beta source in air using the ICRP reference phantoms. Radiation Measurements, 145, 106612.

Gualdrini, G., Agosteo, S., Ménard, S., Price, R.A., Chartier, J.-L., Großwendt, B., Kodeli, I., Leuthold, G.P., Siebert, B.R.L., Tagziria, H., Tanner, R.J., Terrissol, M., Zankl, M., 2005. QUADOS intercomparison: a summary of photon and charged particle problems. Radiation Protection Dosimetry, 115(1-4), 587-599.

Huet, C., Eakins, J., Zankl, M., Gómez-Ros, J.M., Jansen, J., Moraleda, M., Struelens, L., Akar, D.K., Borbinha, J., Brkić, H., Bui, D.K., Capello, K., Linh Dang, T.M., Desorgher, L., Di Maria, S., Epstein, L., Faj, D., Fantinova, K., Ferrari, P., Gossio, S., Hunt, J., Jovanovic, Z., Kim, H.S., Krstic, D., Le, N.T., Lee, Y.-K., Murugan, M., Nadar, M.Y., Nguyen, N.-Q., Nikezic, D., Patni, H.K., Santos, D.S., Tremblay, M., Trivino, S., Tymińska, K., 2022. Monte Carlo calculation of organ and effective doses due to photon and neutron point sources and typical X-ray examinations: Results of an international intercomparison exercise. Radiation Measurements, 150, 106695.

ICRP, 2002. Basic anatomical and physiological data for use in radiological protection: reference values. ICRP publication 89. Annals of the ICRP 32, 5.

ICRP, 2007. The 2007 Recommendations of the International Commission on Radiological Protection. ICRP Publication 103. Annals of the ICRP, 37(2-4).

ICRP, 2009. Adult reference computational phantoms. ICRP Publication 110. Annals of the ICRP, 39(2).

ICRP, 2010. Conversion Coefficients for Radiological Protection Quantities for External Radiation Exposures. ICRP Publication 116. Annals of the ICRP, 40(2-5).

Johnson, P.B., Bahadori, A.A., Eckerman, K.F., Lee, C., Bolch, W.E., 2011. Response functions for computing absorbed dose to skeletal tissues from photon irradiation - an update. Physics in Medicine and Biology, 56(8), 2347–2365.

Kerr, G.D., Eckerman, K.F., 1985. Neutron and photon fluence-to-dose conversion factors for active marrow of the skeleton. in: Schraube, H., et al., (Ed.), Fifth Symposium on Neutron Dosimetry. Luxembourg: Commission of the European Communities, 133-145.

Price, R.A., Gualdrini, G., Agosteo, S., Ménard, S., Chartier, J.-L., Großwendt, B., Kodeli, I., Leuthold, G.P., Siebert, B.R.L., Tagziria, H., Tanner, R.J., Terrissol, M., Zankl, M., 2006. Pitfalls and modelling inconsistencies in computational radiation dosimetry: lessons learnt from the QUADOS intercomparison. Part II: Photons, electrons and protons. Radiation Protection Dosimetry, 118(2), 155-166.

Rabus, H., Zankl, M., Gómez-Ros, J.M., Villagrasa, C., Eakins, J., Huet, C., Brkić, H., Tanner, R., 2022. Lessons learnt from the recent EURADOS intercomparisons in computational dosimetry. Radiation Measurements, 156, 106822.

Siebert, B.R.L., Tanner, R.J., Chartier, J.-L., Agosteo, S., Großwendt, B., Gualdrini, G., Ménard, S., Kodeli, I., Leuthold, G.P., Price, R.A., Tagziria, H., Terrissol, M., Zankl, M., 2006. Pitfalls and modelling inconsistencies in computational radiation dosimetry: lessons learnt from the QUADOS intercomparison. Part I: Neutrons and uncertainties. Radiation Protection Dosimetry, 118(2), 144-154.

Tanner, R.J., Chartier, J.L., Siebert, B.R.L., Agosteo, S., Grosswendt, B., Gualdrini, G., Kodeli, I., Leuthold, G.P., Menard, S., Price, R.A., Tagziria, H., Terrissol, M., Zankl, M., 2004. Intercomparison on the usage of computational codes in radiation dosimetry. Radiation Protection Dosimetry, 110(1-4), 769-780.

Vrba, T., Broggio, D., Caldeira, M., Capello, K., Fantínová, K., Franck, D., Gómez-Ros, J.M., Hunt, J., Kinase, S., Leone, D., Lombardo, P.A., Manohari, M., Marzocchi, O., Moraleda, M., Nogueira, P., Ośko, J., Arron, S., Suhl, S., Takahashi, M., Teles, P., Tremblay, M., Tymińska, K., Lopez, M.A., Tanner, R., 2015. EURADOS intercomparison exercise on MC modelling for the in-vivo monitoring of AM-241 in skull phantoms (Part II and III). Radiation Physics and Chemistry, 113, 59-71.

Vrba, T., Nogueira, P., Broggio, D., Caldeira, M., Capello, K., Fantínová, K., Figueira, C., Hunt, J., Leone, D., Murugan, M., Marzocchi, O., Moraleda, M., Shutt, A., Suh, S., Takahashi, M., Tymińska, K., Antonia Lopez, M., Tanner, R., 2014. EURADOS intercomparison exercise on MC modeling for the in-vivo monitoring of Am-241 in skull phantoms (Part I). Radiation Physics and Chemistry, 104, 332-338.

Zankl, M., Becker, J., Fill, U., Petoussi-Henß, N., Eckerman, K.F., 2005. GSF male and female adult voxel models representing ICRP Reference Man - the present status, The Monte Carlo Method: Versatility Unbounded in a Dynamic Computing World. La Grange Park, USA: American Nuclear Society, Chattanooga, TN, USA.

Zankl, M., Eakins, J., Gómez Ros, J.-M., Huet, C., 2021a. The ICRP recommended methods of red bone marrow dosimetry. Radiation Measurements, 146, 106611.

Zankl, M., Eakins, J., Gómez Ros, J.-M., Huet, C., Jansen, J., Moraleda, M., Reichelt, U., Struelens, L., Vrba, T., 2021b. EURADOS intercomparison on the usage of the ICRP/ICRU adult reference computational phantoms. Radiation Measurements, 145, 106596.

Zankl, M., Gómez Ros, J.-M., Moraleda, M., Reichelt, U., Akar, D.K., Borbinha, J., Desorgher, L., Di Maria, S., El Bakkali, J., Fantinova, K., Ferrari, P., Gossio, S., Hunt, J., Jovanovic, Z., Kim, H.S., Krstic, D., Lee, Y.-K., Nadar, M.Y., Nikezic, D., Patni, H.K., Murugan, M., Triviño, S., 2021c. Monte Carlo calculation of organ dose coefficients for internal dosimetry: Results of an international intercomparison exercise. Radiation Measurements, 148, 106661.

Zankl, M., Wittmann, A., 2001. The adult male voxel model "Golem" segmented from whole body CT patient data. Radiation and Environmental Biophysics, 40, 153-162.

5. Unfolding Neutron Spectra from Bonner Sphere Measurements

Carles Domingo Miralles, Autonomous University of Barcelona, Spain

Abstract

Bonner Sphere Spectrometry (BSS) is the most commonly used technique for neutron spectrometry for radiation protection purposes. Provided there exists a well-established response matrix and adequate irradiation conditions, the most delicate part of the BSS is the unfolding process. Some relevant general aspects of the unfolding procedure are discussed and some practical advice to the user, in view of the results of the recent EURADOS unfolding exercise, is given. It is expected that this will help to improve the user's abilities and self-criticism when analysing results of unfolding processes.

5.1. Introduction

Among the many available neutron spectrometry techniques, the multi-sphere or Bonner sphere spectrometer (BSS) is the most commonly used for radiation protection purposes (Thomas and Alevra, 2002). This type of spectrometer, first described by Bramblett, Ewing and Bonner (1960), consists of a thermal neutron detector placed at the centre of a number of different diameter moderating spheres. The main advantageous characteristics that make this type of spectrometers widely used are (Thomas, 2010):

- Their almost isotropic response.
- The wide neutron energy range it can cover, extending from thermal to GeV neutrons.
- The large variety of active or passive thermal sensors that can be used, allowing to adapt the sensitivity to the specific workplace.
- Their capability to discriminate between the gamma rays and the neutron component.
- Their ability to cope with pulsed fields using passive detectors.

Disadvantages of BSSs are their relatively poor energy resolution, which does not allow the appreciation of fine structures such as narrow peaks, their weight, and the need to sequentially irradiate the spheres. This requires, in general, long exposure periods. In addition, a relevant drawback of BSS is the uncertainty in the spectrum unfolding (Reginatto, 2010). Despite these drawbacks, no other spectrometric system is able to provide operational neutron spectrometry over more than 12 energy decades in reasonable measurement times.

Provided a well-established response matrix and adequate irradiation conditions exist (Alevra and Thomas, 2003), the most delicate part of the BSS-based spectrometry is the unfolding process. Many computerized BSS unfolding codes have been developed, which are in general complex to use, which need expert usage and require realistic prior information, such as a "default spectrum" as close as possible to the spectrum to be obtained (Thomas, 2004). Unfolding codes, hence, cannot be used as "black boxes" because they require some guidance from the user to converge to realistic meaningful solutions. The user's skills, therefore, have a relevant impact on the significance of the solution found.

In this chapter, some relevant general aspects of the unfolding procedure are discussed, the particularities of some of the most used codes are explained and some practical advice to the user, in view of the results of the recent EURADOS unfolding exercise, is given. It is expected that this will help to improve the user's abilities and self-criticism when analysing results of unfolding processes.

5.2. Unfolding

5.2.1. Basics

To start from a simple academic situation, assume a monoenergetic neutron field of total fluence Φ and energy E_0 impinging on a given sphere, i, of a BSS, which produces a reading M_i in the related measuring instrument. The fluence response $R_i(E_0)$ of the sphere i to these monoenergetic neutrons is, by definition, $R_i(E_0) = M_i/\Phi$.

Realistic neutron fields are far from being monoenergetic, so that they are characterized by an energy distribution of their fluence $\phi_E(E) \equiv \frac{d\phi}{dE}(E)$. Obviously, the total fluence Φ is its integral over all energies

$$\Phi = \int_E \phi_E(E)dE \tag{5.1}$$

This energy distribution $\phi_E(E)$ is generally called the "neutron spectrum". It is also common to introduce the unit energy distribution, or "unit neutron spectrum", $\varphi_E \equiv \frac{\phi_E(E)}{\Phi}$, so that

$$\Phi = \int_E \phi_E(E)dE = \Phi \int_E \varphi_E(E)dE \tag{5.2}$$

and

$$\int_E \varphi_E(E)dE = 1 \tag{5.3}$$

Let $R_i(E)$ represent the response function of the i-th sphere of a BSS. The reading M_i from this sphere is related to the neutron spectrum through this response function.

$$M_i = \int_E R_i(E)\phi_E(E)dE = \Phi \int_E R_i(E)\varphi_E(E)dE \tag{5.4}$$

A given BSS composed of m spheres will be therefore characterized by m response functions, constituting the so-called response matrix of the BSS. Fig. 5.1 displays the response matrix of a hypothetic BSS, with a ^{3}He proportional counter as thermal detector at the centre of the spheres, as provided to the participants in the past EURADOS unfolding exercise (Gómez-Ros et al., 2018, 2022)

Some of the basic principles of Bonner Sphere spectrometry (Thomas and Alevra, 2002) are illustrated in Fig. 5.1, where the peak in the response function moves to higher energies as the sphere size increases. The degree of neutron moderation in small spheres is small, so that low-energy neutrons reaching the sphere have a reasonable probability of reaching the thermal sensor and being detected, whereas fast neutrons tend to escape the sphere before being thermalized. Larger spheres lead to more capture probability of low-energy neutrons, so that they are absorbed in the polyethylene before reaching the thermal detector, and also to more moderation, allowing higher energy neutrons to slow down before arriving to the thermal sensor. In this situation, it is the high-energy neutrons reaching the sphere that have the highest probability of being detected.

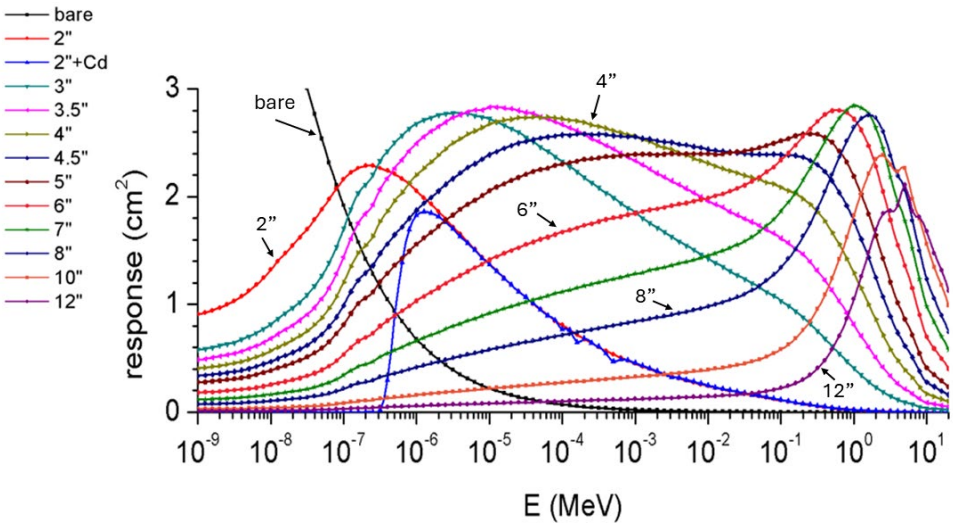

Fig. 5.1: Response matrix of a hypothetic BSS. The different curves represent the response functions of spheres of different diameter and correspond to the rows of the response matrix. (Note that the sphere diameter is conventionally given in inches - symbol " - with 1" = 2.54 cm.)

The problem of unfolding is conceptually simple. From a set of m equations of type (4), one must find the total fluence Φ and the neutron unit spectrum $\varphi_E(E)$ that better suits the m experimental measurements M_i. The first noticeable and unavoidable difficulty is having to obtain a continuous function $\varphi_E(E)$, extending over more than 12 energy decades, from a finite number of equations m, usually of the order of 10-15. Discretizing the energies is necessary, so that neutron spectrum $\phi_E(E)$ and unit spectrum $\varphi_E(E)$ are converted to n-bins histograms, respectively as ϕ_j and φ_j, and the set of response functions $R_i(E)$ becomes a matrix, R_{ij}. In this way, Eq. 5.4 is transformed into (Matzke, 2003; Thomas, 2010)

$$M_i = \sum_{j=1}^{n} R_{ij}\phi_j = \Phi \sum_{j=1}^{n} R_{ij}\varphi_j \tag{5.5}$$

"Clever" energy binning is needed to cover the complete energy range of the neutron field under study without losing relevant information. The number of bins n must be big enough to have relevant information about the spectrum structure, but treatable in practice. Typical values of n are in the range 50-200. Equispaced energy bins would have the drawback that all information about the structure of the thermal peak and epithermal spectrum would fall into the first bin. For this reason, binning is normally not linear, and logarithmic equidistantly spaced binning is commonly used.

At this point, we can summarize the unfolding problem to obtain the n values of ϕ_j from a set of m measurements M_i, related with m equations of type (5) through the response matrix R_{ij}. The problem arises from the fact that the number of equations m (typically 10-15) is much lower than the number of unknowns n (typically 50-200). Fig. 5.2 shows a schematic representation of the unfolding process.

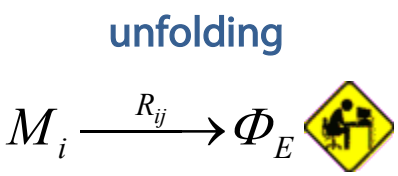

Fig. 5.2: Schematical representation of the unfolding process (and of the unfolder point of view)

5.2.2. Underdetermination, pre-information and uncertainty

The fact that the number of equations is much lower than the number of unknowns ($m < n$) makes unfolding an undetermined problem, with an infinite number of mathematically possible solutions. Of these functions that could mathematically satisfy the problem, only a limited number are physically acceptable. Additional information needs to be used, including the fact that fluence cannot be negative in any of the energy bins, and that the most commonly known neutron spectra do not display sharp peaks. In any case, these pieces of information are not enough to break the underdetermination of the method.

A valuable piece of information to be considered is a "start spectrum", based on prior knowledge about the primary source of neutrons and the amount of shielding or moderation present. Different unfolding codes and methods make use of different approaches to obtain this start spectrum. Reginatto (2010) presents an extensive review of unfolding methods, while a more up-to-date review is found in Zhu et al., (2019). Without trying to be exhaustive, as there are many other reports describing unfolding codes and dealing with their particularities (Reginatto, Goldhagen and Neumann, 2002; Lacoste et al., 2007; Reginatto, 2010; Barros et al., 2014), there are two main possible approaches:

- Methods where the spectrum is directly modelled using the n energy groups of the binning. In this case, a "guess spectrum", as close as possible to the spectrum to be obtained, is needed to start the unfolding procedure. This guess spectrum may be obtained by computer simulation, by prior knowledge of similar spectra in similar neutron irradiation cases or, even, from artificial intelligence methods. Example of unfolding methods using this approach use the maximum entropy principle or Bayesian methods (Matzke and Weise, 1985; Weise and Matzke, 1989; Weise and Woger, 1993; Kuusela and Panaretos, 2015). Example of such codes is MAXED (Reginatto and Goldhagen, 1999), which at the same time is part of the UMG package (Reginatto et al., 2004) available from the NEA data bank.
- Methods where the spectrum is modelled as a function of a set of physically meaningful parameters. Parametric codes eliminate the non-physical solutions by modelling the neutron spectrum as a superposition of elementary spectra, parameterized in terms of a small number (about ten) of physical parameters. Initial guess values for the parameters are needed in this case, which are normally derived from the physical conditions expected for the measured spectrum. Some codes that use this approach are PHYSTAT (Adye, 2011), FRUIT (Bedogni et al., 2007) or HEPRO (Matzke, 1994).

Examples of different approaches to unfolding are a method based on the singular value decomposition of the response matrix (Půlpán and Králík, 1993), the usage of artificial neural

networks (Vega-Carrillo et al., 2006), or the so-called genetic algorithms (Freeman, Ray Edwards and Bolon, 1999).

It is difficult to determine the uncertainty associated with the unfolding process itself and how this uncertainty affects the resulting spectra. Many codes take into consideration during the unfolding process, at least, the measurement uncertainties of M_i, and some of them are also able to consider uncertainties in the calculation of the response matrix R_{ij}. Nevertheless, in many cases these uncertainties only affect the unfolding convergence criteria but are not used to determine the uncertainty of the resulting spectrum, as they appear only in the equations of the parameters used for probing convergence. FRUIT makes an estimation of this uncertainty from a variability analysis of the parameters characterizing the solution spectrum, whereas Bayesian methods are able to calculate the uncertainty of the resulting spectrum from conditional probability inference.

5.2.3. Number and diameter of spheres

One question which may arise is whether increasing the number of spheres increases the information available for unfolding, so that the energy resolution of the resulting spectra is improved. Thomas and Alevra (2002) pose the question "how many spheres, and which diameters, should be used for optimal performance?". They also give the answer: "as many spheres as possible, provided the shapes of their response functions differ sufficiently". The fact is that readings from the different spheres are not fully independent, as the energy intervals where different spheres have a non-zero response may be partially superposed. For instance, the response functions of the big spheres are very similar in shape and energy interval (see Fig. 5.1), leading to redundant information and limiting their resolving power.

A reduced number of spheres (4-5 well-chosen ones in the thermal to 20 MeV region) already contain all possible spectrometric information on the neutron field. Every added sphere brings new information on the neutron spectrum, but the amount of added information decreases for every added sphere. Deriving the spectrum from few "effective" spheres with partially overlapped and similar responses, will unavoidably lead to loss of information (spectral details) and to give a "foggy" view of the reality (real spectrum). This is especially true for energy regions where the resolving power is low.

Nevertheless, using additional "redundant" spheres helps to prevent errors. In fact, the count profile curves should be smooth if the following conditions apply to the measurements: they are performed under stable conditions, are not subject to supplementary uncertainties of unexplained origin, and the right monitors are used (Alevra and Thomas, 2003). Then, outliers can be easily detected and excluded, which otherwise could bias the unfolding process. This is illustrated in Fig. 5.3, where the counts provided to the participants of the EURADOS unfolding exercise (Gómez-Ros et al., 2018, 2022) are shown graphically for all scenarios. Smooth behaviour of the counts as a function of the sphere diameter is apparent in all cases, except in the skyshine scenario. Redundancy of the information provided by the different spheres helps to identify that the result for the 6-inch sphere is a possible outlier. In this case, this was done in purpose for the participants to detect it.

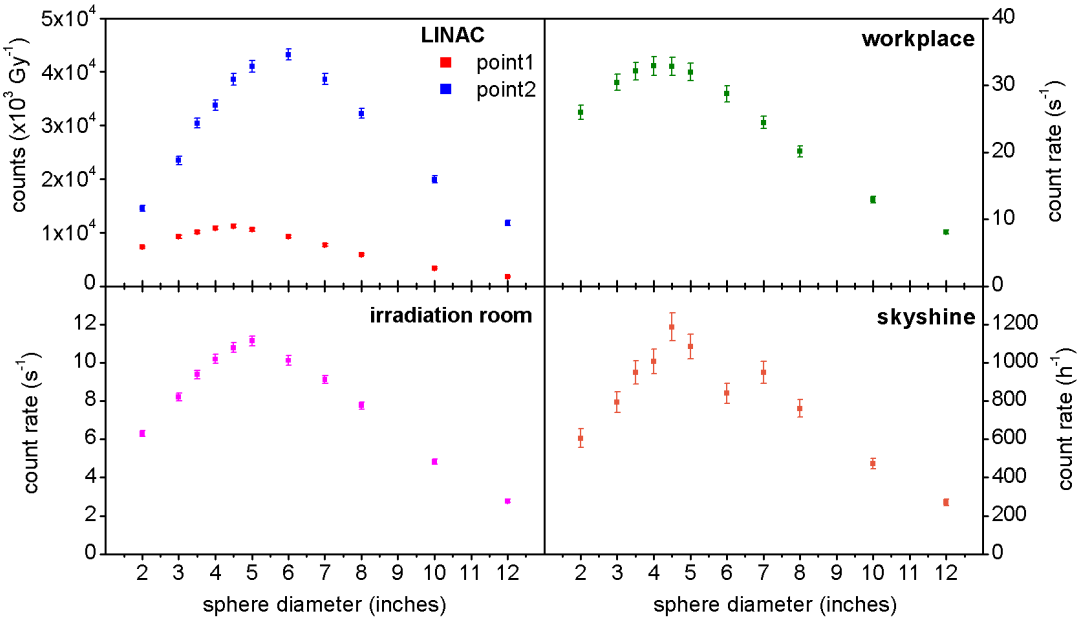

Fig. 5.3: Count rates provided to the participants of the EURADOS unfolding exercise for all scenarios (Gómez-Ros et al., 2018, 2022).

5.2.4. General unfolding procedure

It is difficult to give a detailed description of the steps followed by a generic unfolding procedure as each method uses specific approaches and has its own particularities. Fig. 5.4 tries to summarize the steps that most of the unfolding codes follow in order to obtain a solution. The unfolding starts from an initial guess spectrum ("trial solution" in Fig. 5.4). A "trial count array" is obtained by applying the response matrix to the trial solution, which is compared to the "measured count array". (A "count array" is the set of counts M_i for all spheres of a given BSS.) This gives an "error signal" representative of how different the compared arrays are. If the "error signal" is small enough compared to uncertainties, then the process finishes and the "trial solution" becomes the "solution". The convergence criterion of the particular unfolding method in use stablishes when an "error signal" is small enough to finalize the process.

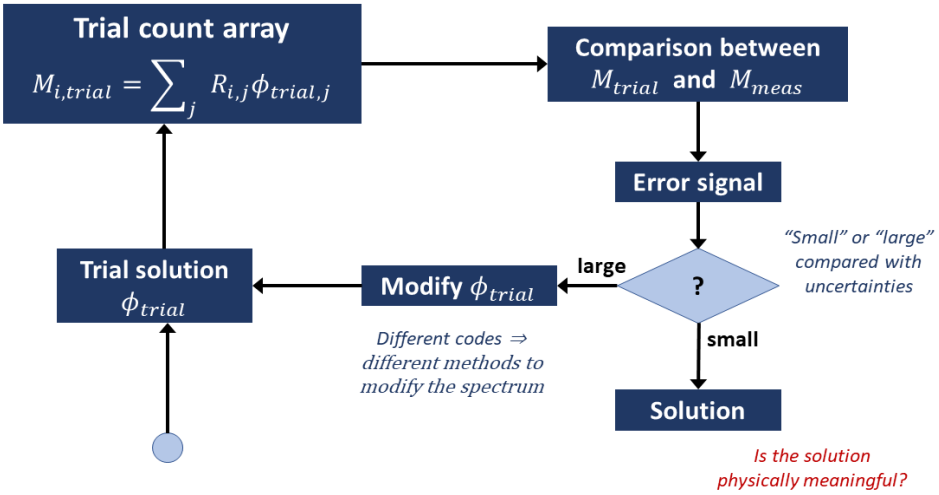

Fig. 5.4: Schematic representation of a general unfolding procedure.

It is very important to emphasize that one must check that the final solution obtained is physically consistent and meaningful. A few aspects to consider:

- The values of all components of the final fluence vector φ_j must be non-negative.
- Knowing the radiation environment where measurements were performed enables to establish reasonable hypothesis about the upper and lower limits for the energy of the neutrons recorded. For instance, no neutrons above 12 MeV may be found around an ^{241}Am-Be source, or no thermal neutrons should appear in measurements around a radionuclide source with suppressed scatter (e.g., shadow cone technique)
- Thermal neutrons always have a Maxwellian distribution.
- The final spectrum should be smooth, if the guess spectrum is so. Fine structures can appear in the result only if included in the pre-information.

5.2.5. Preparing pre-information

Some of the aspects in the last subsection indicate the relevance of having the right pre-information introduced into the unfolding procedure. Pre-information should be accurately chosen and assembled, and all available a-priori data should be implemented. For instance, implementing zero thermal neutrons in measurements of radionuclide source terms with shadow cones or imposing lower/upper energy thresholds for maximum/minimum energies should be included in the pre-information stage.

As an illustrative example, the process of assembling a guess spectrum for a scenario where thermal, epithermal, and fast components are present (for instance, an irradiation room with a radionuclide neutron source) is shown. A "Guess 0" spectrum, shown in Fig. 5.5, is built with the following characteristics:

- The "fast" component is taken from a similar known scenario or from a simple Monte Carlo simulation, not considering the room walls.
- The thermal component is taken as a generic Maxwellian distribution, centred in the right temperature.

- A flat continuous distribution fills the space between the fast and the thermal components.
- No attention is given to the "proportions" of the three components. The unfolding process is unable to add any structures not included in the guess but should be able to correct the proportions and shapes of existing structures.

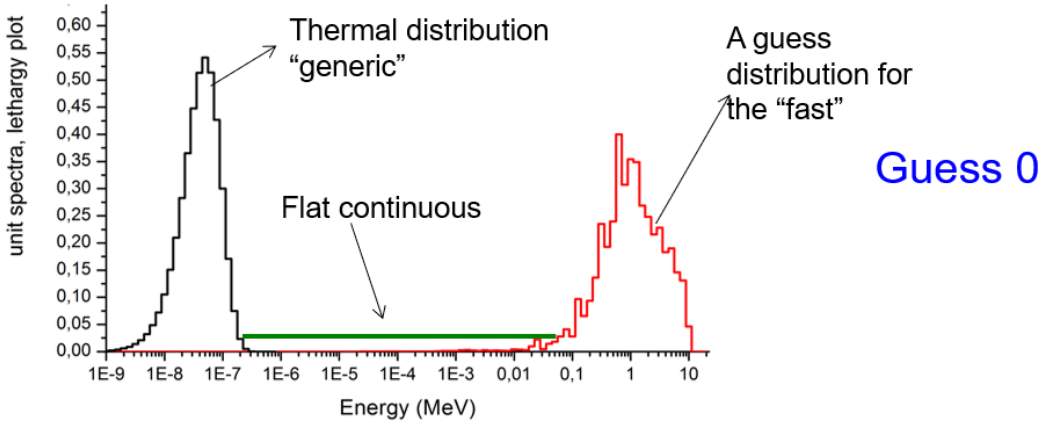

Fig. 5.5: Building of the "Guess 0" spectrum, first step of the preparation of the guess spectrum specified in the text.

A more accurate guess ("Guess 1") is built after parametric unfolding of the measurements performed. Parametric unfolding does not have the resolution to provide the fine structure of the peak in the fast region, but it is likely to provide the right proportions and shape of the thermal and epithermal components. So, "Guess 1" is built with the same approach as "Guess 0" for the fast part and from the results of parametric unfolding for the thermal and epithermal (see Fig. 5.6).

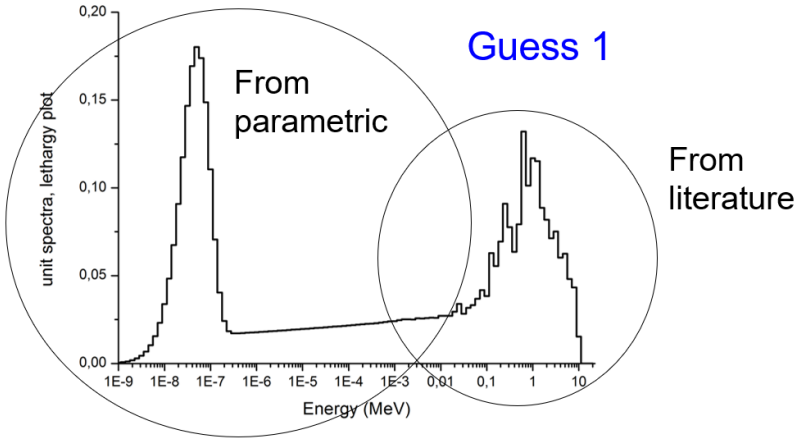

Fig. 5.6: Building of "Guess 1", using the same approach as "Guess 0" for the fast part and results from parametric unfolding for thermal and epithermal regions.

Finally, Fig. 5.7 displays (in red) the spectra obtained from unfolding using "Guess 0" (left) and "Guess 1" (right). The corresponding guess spectra are shown in black, whereas the reference spectrum is shown in green. Although the final results are apparently very similar, close observation and accurate calculation indicate that results obtained using "Guess 1" are closer to the reference spectrum, and fewer iterations were needed to reach the final result.

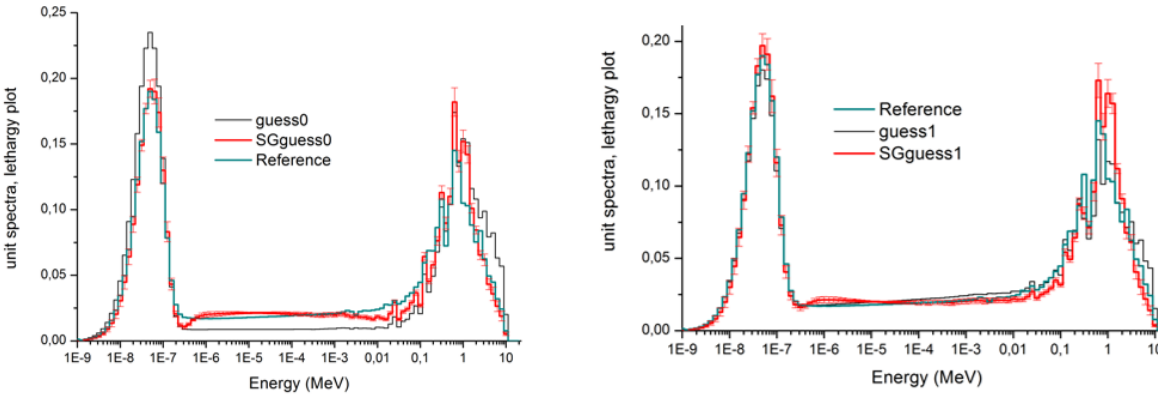

Fig. 5.7: Spectra unfolded using "Guess 0" (left) and "Guess 1" (right). Guess spectra are displayed in black, reference spectrum id shown in green, and results from unfolding are displayed in red.

5.4. The EURADOS unfolding exercise

The results of the EURADOS WG6 unfolding exercise have recently been published (Gómez-Ros et al., 2018, 2022). The details of the exercise and the results obtained are not presented in detail in this report, as they can be found in the referenced publications. Nevertheless, there are some aspects and conclusions arising from the exercise results that are worthy of comment, some of them being very basic warnings to users of unfolding methods.

The problems posed in the exercise were intended to represent realistic workplace situations that unfolding users may encounter in their day-to-day practice. Four different scenarios, one of them with spectra acquired in two different measurement places, were proposed. Different levels of information were given for the scenarios, according with the information likely to be available in a realistic situation. The participants could solve any number of scenarios they wanted, and 64 solutions from 20 participants were collected. A variety of unfolding codes was used, the UMG package being the most widely used code (11 participants), followed by FRUIT (3 participants), and a variety of codes, some of the self-made, used by only one participant.

Some of the output from the exercise is summarized in the following:

- The agreement between the solutions provided by the participants and the reference spectra did not depend on the unfolding code used. There were "good" results and "bad" results from all codes used by more than one person.
- Many of the participants did not check their results visually, so that in some cases negative values appeared, as well as thermal peaks shifted to unrealistic energies or spectra with double thermal peaks.
- Some of the anomalous solutions were submitted by participants who used "self-made" or "non-standard" codes. While "standard" unfolding codes are referenced and benchmarked in many situations, thus providing a reasonable guarantee of their ability to give correct solutions whenever correctly used, "self-made" and "non-standard" codes would require an initial verification process about their capability to correctly solve the problem and to converge to a correct solution. In most cases, no sufficient information was provided by the participants for this purpose.

- No participant provided results from the simple check of folding the response matrix with the obtained spectrum to compare the result with the provided BSS counts.
- Amazing results in neutron spectra unfolding are usually not big discoveries about strange physical phenomena, but tend to be incorrect or inaccurate results

5.5. Summary and conclusions

A summary of several aspects related to unfolding neutron spectra from measurements using a Bonner Sphere Spectrometer (BSS) has been presented.

It must be noticed that BSS unfolding is un underdetermined problem, so that additional information is required to get a physically meaningful solution. Having the right pre-information introduced into the unfolding procedure is unquestionably needed to obtain correct results. Pre-information should be accurately chosen and assembled, and all available a-priori data should be implemented.

Many times, the pre-information is introduced in the form of an initial guess spectrum, or with initial values of the parameters characterizing the spectrum. In any case, the guess needs to be sufficiently close to the actual values, otherwise the unfolding procedure can converge to a mathematically correct, but physically unrealistic solution.

Also, it is vital that the response functions are as near correct as possible, unfolding codes must not be treated as black boxes and energy resolution is always going to be poor. In this last point, it should, however, be possible to combine BS data with high-resolution measurements to produce a spectrum with good resolution in the region where it is important.

And, finally, keep in mind that amazing results in neutron spectra unfolding are usually not big discoveries about strange physical phenomena. They are rather incorrect or inaccurate results.

5.6. References

Adye, T., 2011. Unfolding algorithms and tests using RooUnfold. Proceedings of the PHYSTAT 2011 Workshop on Statistical Issues Related to Discovery Claims in Search Experiments and Unfolding, 313–318. Available at: https://arxiv.org/abs/1105.1160v1 (Accessed: 16 July 2023).

Alevra, A. V., Thomas, D. J., 2003. Neutron spectrometry in mixed fields: multisphere spectrometers. Radiation Protection Dosimetry, 107, 37-72.

Barros, S. et al., 2014. Comparison of unfolding codes for neutron spectrometry with Bonner spheres. Radiation Protection Dosimetry, 161, 46–52. doi: 10.1093/rpd/nct353.

Bedogni, R. et al., 2007. FRUIT: An operational tool for multisphere neutron spectrometry in workplaces. Nuclear Instruments and Methods in Physics Research Section A: Accelerators, Spectrometers, Detectors and Associated Equipment, 580, 1301-1309. doi: 10.1016/j.nima.2007.07.033.

Bramblett, R. L., Ewing, R. I., Bonner, T. W., 1960. A new type of neutron spectrometer. Nuclear Instruments and Methods, 9, 1-12. doi: 10.1016/0029-554X(60)90043-4.

Freeman, D. W., Ray Edwards, D. and Bolon, A. E. (1999) Genetic algorithms - a new technique for solving the neutron spectrum unfolding problem. Nuclear Instruments and Methods in Physics Research, Section A: Accelerators, Spectrometers, Detectors and Associated Equipment, 425(3), 549–576. doi: 10.1016/S0168-9002(98)01427-2.

Gómez-Ros, J. M. et al., (2018) International comparison exercise on neutron spectra unfolding in Bonner spheres spectrometry: problem description and preliminary analysis. Radiation Protection Dosimetry, 180, 70–74. doi: 10.1093/rpd/ncy002.

Gómez-Ros, J. M. et al., 2022. Results of the EURADOS international comparison exercise on neutron spectra unfolding in Bonner spheres spectrometry. Radiation Measurements, 153, 106755. doi: 10.1016/j.radmeas.2022.106755.

Kuusela, M., Panaretos, V. M., 2015. Statistical unfolding of elementary particle spectra: Empirical bayes estimation and bias-corrected uncertainty quantification. Annals of Applied Statistics, 9, 1671–1705. doi: 10.1214/15-AOAS857.

Lacoste, V. et al., 2007. Bonner sphere neutron spectrometry at nuclear workplaces in the framework of the EVIDOS project. Radiation Protection Dosimetry, 125, 304–308. doi: 10.1093/rpd/ncm161.

Matzke, M., 1994. Unfolding of pulse height spectra : the HEPRO program system. Available at: https://cds.cern.ch/record/275528 (Accessed: 16 July 2023).

Matzke, M., 2003. Unfolding procedures. Radiation Protection Dosimetry, 107, 155–174. Available at: http://rpd.oxfordjournals.org/content/107/1-3/155.short.

Matzke, M. and Weise, K. (1985) Neutron spectrum unfolding by the Monte Carlo method. Nuclear Inst. and Methods in Physics Research A, 234, 324–330. doi: 10.1016/0168-9002(85)90924-6.

Půlpán, J., Králík, M., 1993. The unfolding of neutron spectra based on the singular value decomposition of the response matrix, Nuclear Inst. and Methods in Physics Research A, 325, 314–318. doi: 10.1016/0168-9002(93)91032-I.

Reginatto, M. et al., (2004) UMG 3.3, Analysis of data measured with spectrometers using unfolding techniques. Available at: https://www.oecd-nea.org/tools/abstract/detail/nea-1665 (Accessed: 16 July 2023).

Reginatto, M., 2010. Overview of spectral unfolding techniques and uncertainty estimation. Radiation Measurements, 45, 1323–1329. doi: 10.1016/j.radmeas.2010.06.016.

Reginatto, M., Goldhagen, P., 1999. MAXED, a computer code for maximum entropy deconvolution of multisphere neutron spectrometer data. Health Physics, 77, 579–583. doi: 10.1097/00004032-199911000-00012.

Reginatto, M., Goldhagen, P., Neumann, S., 2002. Spectrum unfolding, sensitivity analysis and propagation of uncertainties with the maximum entropy deconvolution code MAXED. Nuclear Instruments and Methods in Physics Research, Section A: Accelerators, Spectrometers, Detectors and Associated Equipment, 476, 242–246. doi: 10.1016/S0168-9002(01)01439-5.

Thomas, D., Alevra, A., 2002. Bonner sphere spectrometers—a critical review. Nuclear Instruments and Methods in Physics Research Section A: Accelerators, Spectrometers, Detectors and Associated Equipment, 476, 12–20. doi: 10.1016/S0168-9002(01)01379-1.

Thomas, D. J., 2004. Neutron spectrometry for radiation protection. Radiation Protection Dosimetry, 110, 141–149. doi: 10.1093/rpd/nch204.

Thomas, D. J., 2010. Neutron spectrometry. Radiation Measurements, 45(10), 1178–1185. doi: 10.1016/j.radmeas.2010.04.016.

Vega-Carrillo, H. R. et al., 2006. Neutron spectrometry using artificial neural networks. Radiation Measurements, 41, 425–431. doi: 10.1016/j.radmeas.2005.10.003.

Weise, K., Matzke, M., 1989. A priori distributions from the principle of maximum entropy for the Monte Carlo unfolding of particle energy spectra. Nuclear Instruments and Methods in Physics Research A, 280, 103–112. doi: 10.1016/0168-9002(89)91277-1.

Weise, K., Woger, W., 1993. A Bayesian theory of measurement uncertainty. Measurement Science and Technology, 4(1), 1–11. doi: 10.1088/0957-0233/4/1/001.

Zhu, H. et al., 2019. A Hierarchical Bayesian Approach to Neutron Spectrum Unfolding with Organic Scintillators. IEEE Transactions on Nuclear Science, 66, 2265–2274. doi: 10.1109/TNS.2019.2941317.

6. EURADOS Intercomparisons in Computational Dosimetry

Rick Tanner, UK Health Security Agency, United Kingdom; **Hans Rabus**, Physikalisch-Technische Bundesanstalt; Germany, **Hrvoje Brkić**, Strossmayer University of Osijek (MEFOS), Croatia; **Jonathan Eakins**, UK Health Security Agency, United Kingdom; **José Maria Gómez-Ros**, Centro de Investigaciones Energéticas, Medioambientales y Tecnológicas (CIEMAT), Spain; **Christelle Huet**, Institut de Radioprotection et de Sûreté Nucléaire (IRSN), France; **Carmen Villagrasa**, Institut de Radioprotection et de Sûreté Nucléaire (IRSN), France; **Maria Zankl**, Helmholtz Zentrum München German Research Centre for Environmental Health (HMGU), Germany.

Abstract

This chapter reviews the contributions of EURADOS Working Group 6 "Computational Dosimetry" and the history of intercomparisons in computational dosimetry organized by it. The last section reproduces the summary paper from a recent Virtual Special Issue in Radiation Measurements on EURADOS intercomparisons in computational dosimetry, which highlights common issues and the lessons learnt from these exercises.

6.1. Introduction

EURADOS has had a Working Group (WG) on Computational Dosimetry (WG6) since it was founded in 1982, which makes it the only WG that has been ever present in EURADOS. It was needed because in the 1980s computational dosimetry was the domain of a few experts, often working alone with their own code, Monte Carlo or deterministic, which provided little opportunity for collaboration, dissemination or more importantly comparison. It was, however, already recognized that computational methods were becoming increasingly important for developments in radiation protection and dosimetry, and that the other EURADOS WGs would benefit from the capability offered by scientists with computational skills.

Home-made codes had many benefits which derived from the scientist writing the code needing to be an expert in exactly how it worked. They could also be more efficient because the originator could include only the physics and data that they required for their problem, at a time when memory and cpu requirements placed significant restrictions on the modelling that could be performed. Home-made codes also offered independent results (Siebert and Schuhmacher, 1995, Grosswendt, 1990, Zankl et al., 1988, Siebert and Schuhmacher, 1994, Shrimpton et al., 1986) which avoided problems that might arise where widely available codes could produce similar biases in solutions from various scientists working in different laboratories.

The authors of the home-made codes could not use them as "black boxes", and instead needed to understand exactly how they worked, and all the physics contained within. However, these "in-house" codes also suffered from limitations of available developer hours, and the codes also often retired with their originator. The limitations on the developer time tended to make it hard for the originator to produce coupled codes for multiple particle types, which left them restricted to one or few particles.

In the 1980s, users struggled to get calculations to run because of memory limits and computational speed. The memory limits were particularly problematic for neutron calculations because of the need for cross-section data that span many logarithmic decades of energy with complex energy

dependences for many different reaction channels. This was often addressed by using group cross-sections for less important isotopes or simplifying material specifications. Additionally, since all computation was performed on mainframe computers, competing for CPU with other users' slowed progress. Now, running the most widely used codes on PCs or PC Clusters is routine, and users seem less focussed on applying variance reduction methods to get convergence in their results: in the past, users were forced to consider variance reduction methods to obtain results within a reasonable timeframe.

In the 40+ years since the *Computational Dosimetry* Working Group was formed, the behemoth codes with huge teams of developers have taken over. These cover all particle types that can possibly be relevant to radiation protection and dosimetry. They can also be run easily on a variety of operating systems and computers. They are much easier to install and implement, and the user does not need to understand the physics they are applying to use the code. Consequently, far more scientists are using Monte Carlo as a tool, without it being the most important part of their working life. The use of computational methods has hence spread to all other EURADOS Working Groups, so it is not just a capability found within WG6.

In the period of over 40 years in which the Working Group has existed, there have only been five chairs: Siegfried Wagner, Bernd Siebert, Gianfranco Gualdrini, Rick Tanner and now Hans Rabus. Membership of the working group has also had a regular flow of scientists in and out, so there are too many members to list here.

During this period, intercomparisons have become a central part of the *Computational Dosimetry* WG work programme, but they are also now a major part of what EURADOS does. Most EURADOS WGs include intercomparisons in their work programme, which enables EURADOS to support the accreditation of many services, since the EN ISO/IEC 17025:2017 (Petrovic et al., 2020, ISO, 2017) requires Interlaboratory and Intralaboratory comparisons.

The first Computational Dosimetry Working Group intercomparison (Alevra et al., 1990) involved unfolding methods rather than deterministic or Monte Carlo radiation transport modelling. Though in practice, computational modelling was necessary to calibrate the Bonner Sphere sets (Bramblett et al., 1960, Hertel and Davidson, 1985) used for the measurements. At that stage unfolding methods for neutron spectroscopy were relatively undeveloped so the scientists in the WG developed methods via interlaboratory comparisons which were subsequently employed in a EURADOS measurement programme in Swedish nuclear reactors (Lindborg et al., 1995).

6.1.1. What is an Intercomparison?

Whilst this might sound a simple question, within WG6 this has been an evolving concept. Broadly speaking, there are two distinct types of intercomparison that WG6 has run, with the main distinguishing feature being the relative complexity of the problem. Where the problem is very complex (Type 1), WG6 members have worked together to produce an agreed best solution. For simpler problems (Type 2), to assess the competence of computational modellers working in the field, problem sets have been distributed for anyone in the radiation protection and dosimetry community to attempt. There is some blurring of the distinction between Type 1 and Type 2 on occasions, but this is a useful distinction to maintain in this work.

6.1.2. What Is the "right" answer?

For Type 1 intercomparisons, the "right" answer is essentially what the participants are trying to work out together. Though, of course, there are many uncertainties and potential biases that mean that we can never determine the exact "right" answer. Monte Carlo statistical uncertainties are commonly used to imply high precision on a calculated result, but the uncertainty is not just a matter of the computational statistics, there are also uncertainties associated with the input data and the models used. Those uncertainties are harder to evaluate and control. In general, for Type 1 intercomparisons convergence on the optimum agreed solution is the best we can aspire for.

Type 2 intercomparisons need a reference solution against which the participants' solutions can be compared. This is a slightly contentious process because the choice of the reference solution is not straightforward. The scientist who proposed the problem should, in principle, be very familiar with the modelling required and highly competent. However, there can be no expectation that their solution is indeed the "best", if best is even a meaningful term in this context.

WG6 has commonly used the "author's" solution as a reference, and sometimes used other WG members to verify that solution. In the sections below where this is done, it is not intended to imply that the author of the problem produced the best solution. However, it is anticipated that their solution is high quality, and in practice the deviations from the authors solution that matter are not particularly sensitive to the accuracy of that solution: discussions about a few % difference between good solutions are pretty immaterial when some solutions deviate by factors more than 2, or even in cases more than 10 or even 100. Taking an average of the "best solutions" might seem appealing, but in practice it is hard to determine what solutions would be good enough to include in determining the reference. This would be especially problematic where there is good agreement over part of the energy range, for example, but large disagreement elsewhere.

6.2. ICRU Report 57/ICRP Publication 74

The publication of the International Commission on Radiation Measurement, and Units (ICRU) Reports 39 (ICRU, 1985) and 51 (ICRU, 1987), and ICRP Publication 60 (ICRP, 1991) led to a situation where national legislations would require radiation protection from external sources of radiation to be performed using dose quantities for which conversion coefficients from fluence or air kerma to dose equivalent or effective dose had not yet been evaluated. The ICRU and ICRP asked the EURADOS Computational Dosimetry WG to assist, which resulted in the data for protection and operational quantities that are tabulated in ICRU Report 57 (ICRU, 1998) and ICRP Publication 74 (ICRP, 1996). This work was co-ordinated by WG6, but there were inputs from outside EURADOS.

In the early 1990s voxel phantoms were being developed (Zankl et al., 1988), but they were not yet approved by the ICRP or sufficiently ready for the calculation of reference effective dose conversion coefficients. There were also insufficient laboratories with the expertise, so effective quality control on the results was not then possible. Simpler phantoms were hence required for the computation of effective dose.

Several members of the Working Group had implemented geometric phantoms, such as that proposed in MIRD Pamphlet No 5 (Snyder et al., 1969), and had significant experience of using them to calculate *effective dose equivalent*, which was the then current protection quantity. It was hence natural that the WG would use these simpler geometric phantoms to calculate the *equivalent dose* and *effective dose* conversion coefficients required to implement the newly published ICRP

Publication 60 (ICRP, 1991). However, each implementation of the MIRD phantoms was unique, so the process required comparisons of the results from each participating laboratory.

The WG also contained much Monte Carlo expertise which enabled calculation of the operational quantities: $H_p(d, q)$, $H^*(10)$ and $H'(d, q)$. These needed to be recalculated following their redefinition (ICRU, 1980, ICRU, 1985, ICRU, 1987) and to account for the changes to the quality factor (ICRP, 1991) and the stopping powers of protons and alpha particles (ICRU, 1993).

The process of generating the new conversion coefficients was in effect a Type 1 intercomparison, in which the WG members presented their results at WG meetings, differences were discussed, mistakes, such as failure to implement the best thermal neutron transport, were uncovered, and a degree of convergence between the solutions was reached. The full ICRU Report 57 (ICRU, 1998) and ICRP Publication 74 (ICRU, 1998) include many tables of data for photons, neutrons and electrons with the data for the operational quantities still being in use today, whilst the equivalent dose and effective dose have been superseded by values from more modern voxel phantom calculations (ICRP, 2010).

Data for the neutron equivalent dose to the female liver for right lateral, plane parallel irradiation (Fig. 6.1) show the good final agreement for four laboratories. The final dataset was taken from a fitted evaluation, since conversion coefficients could not be taken from a tabulation of the data from the five datasets, but in this instance the relatively small deviations from the fitted curve give good confidence that the computations were reliable.

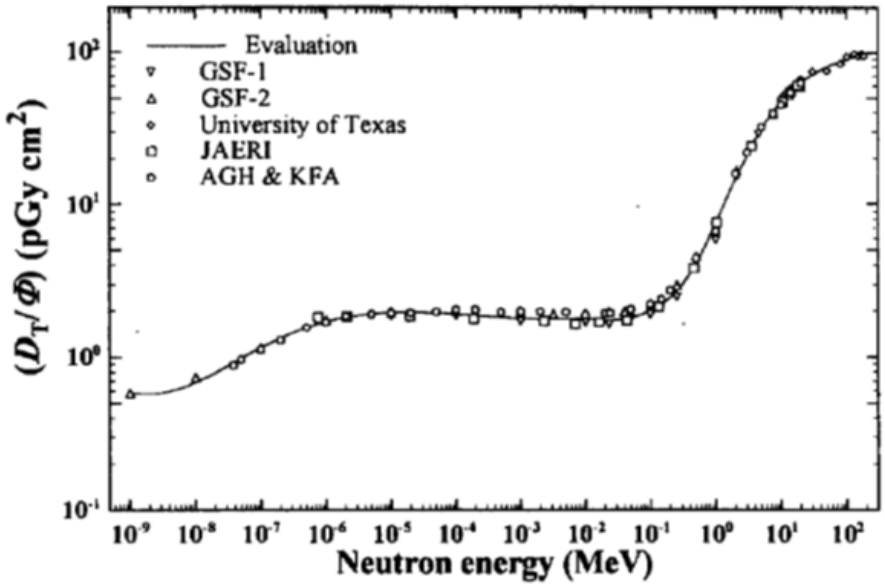

Fig. 6.1: Equivalent dose conversion coefficients for neutrons, per unit fluence, for the female liver for irradiation from the right using a plane parallel beam (ICRP, 1996, ICRU, 1998).

Final agreement was not always so good, with the final data for the male colon for right lateral irradiation using neutrons showing significant divergence (Fig. 6.2). Good agreement could not be obtained in this instance because of the ill-defined nature of the colon, which meant that the dose equivalent deposited in the colon was very variable. Without good, official, reference computational phantoms, this could not be resolved.

Despite the operational quantities being defined in simple phantoms, with easy to define geometries and materials, there remained significant divergences between the datasets for conversion coefficients, especially for electrons and neutrons. The poor quality of the available electron transport and the absence of coupled photon/electron codes meant that divergences of ±10% were seen, and for neutrons difficulties with thermal neutron transport caused even bigger divergences between datasets. The over-riding conclusions were that:

- Electron and neutron Monte Carlo were not yet accurate enough.
- Anthropomorphic phantoms needed to be consistent.
- The best thermal neutron transport needed to be invoked.
- The kerma approximation needed to be applied to make the calculations feasible.

There were additional issues with the definitions of the operational quantities at a point in tissue. Point detectors exist in many Monte Carlo codes, but there are conceptual difficulties that require spheres of exclusion. There is also the issue raised in the final bullet above: the operational quantities are defined in terms of dose equivalent, not kerma, but dose equivalent requires coupled photon-electron or neutron-photon-electron transport and scoring of the dose deposited along the paths of charged particles in tissue. This requires, sophisticated codes, a volume to score in, not a point, and for the early 1990s vast computational power. So, participants had to select small volumes to score the operational quantities, and also score kerma not dose equivalent. This then cause difficulties when different volumes were selected by different laboratories, simply to ensure the quantity could be calculated. However, these data are still in use today as the reference conversion coefficients for many of the operational quantities.

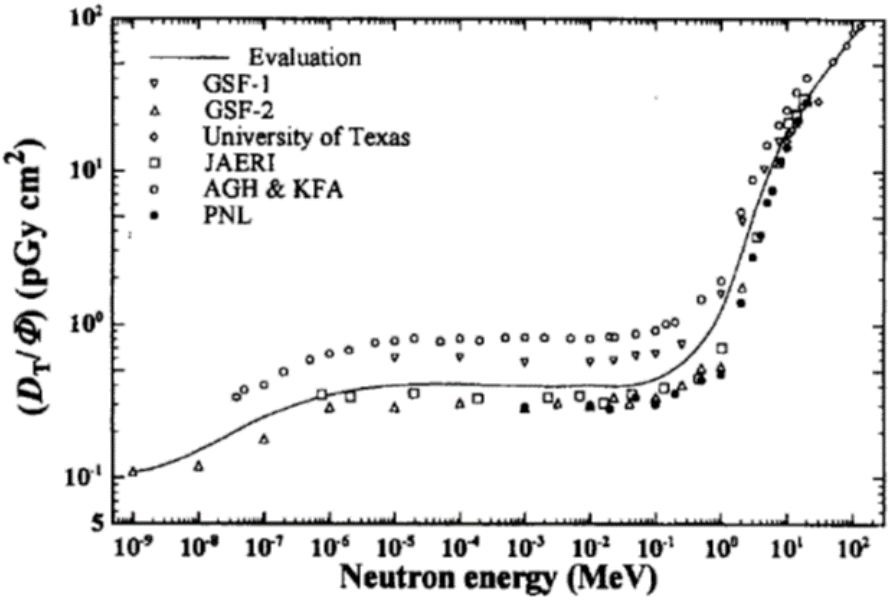

Fig. 6.2: Equivalent dose conversion coefficients for neutrons, per unit fluence, for the female liver for irradiation from the right using a plane parallel beam (ICRP, 1996, ICRU, 1998).

6.3. QUADOS Intercomparison

It had become apparent that there was a need to evaluate how well numerical methods were being applied in the workplace, so the WG submitted a Concerted Action (FIGD-CT-2000-20062) to the European Commission called **QU**ality **A**ssurance of computational tools for **DOS**imetry: QUADOS. This involved scientists from Germany, France, Italy, Slovenia and the United Kingdom.

The objectives of the Concerted Action were defined: "*Computational tools, especially transport codes, are essential for radiation dosimetry. Their quality is generally high, but many casual users do not exploit the full potential of these codes, treat them as black boxes and are prone to erroneous results. These users are seldom familiar with sensitivity analysis and uncertainty assessment, which are required for a quality assured use of codes. The Concerted Action (12 members from universities and research institutions in 5 countries) will invite casual users to participate in an Intercomparison Study (IS). We distribute Bench Mark problems, evaluate and discuss the returns with the participants and summarise the IS in a report. In addition, we will compile and publish reports on Advanced Computational Tools (AT) and Sensitivity Analysis and Uncertainty Assessment (SA). These reports will provide theoretical background and examples of practical applications for AT and SA*."

This was the first formal definition in the WG programme of an "Intercomparison Study". It recognized that the wider dissemination of computation methods was leading to concerns about the quality of results. It was not restricted solely to Monte Carlo methods, but would be open to anyone, from anywhere in the world, to participate. The intended outcomes could be further summarized:

- Provide a snapshot of the methods and codes currently in use.
- Furnish information on the methods used to assess the reliability of computational results.
- Disseminate "good practice" throughout the radiation dosimetry community.
- Provide users with an opportunity to quality assure their procedures.
- Inform the community about the benefits of sensitivity and uncertainty analysis.
- Inform the community about more sophisticated approaches that may be available to them.

The limitations of the intercomparison and the normalization of the participants' data were also further defined:

- Not intended as a comparison of codes.
- Intended as a comparison of usage.
- Solutions normalized, where appropriate to the authors' solutions.
- It is not intended to imply that the author got the correct result.
- Use of an average would be impractical.
- None of the problems have good experimental data.
- Taking an average of the "good" solutions is not practical.

This distinction between it being an intercomparison of usage rather than of codes was important, because WG6 could not draw judgements on the merits of different codes on the basis of results submitted by non-expert users of those codes.

Selection of the problem set was the first major issue, because the problems had to be relevant to radiation protection and dosimetry, stretching for novice users, but also within the capabilities of those less experienced users. Of course, expert users were also welcomed. The full list of eight problems was:

P1: Brachytherapy - anisotropy/depth-dose of ^{192}Ir γ-source
P2: Endovascular: dose profile of a ^{32}P β- source
P3: Eye therapy with 50 MeV proton beam
P4: TLD-albedo dosemeter response and backscatter
P5: Photon phantom backscatter for ISO x-ray beams
P6: ^{252}Cf-source and shadow cone in a calibration room
P7: Ge pulse height detector for 15 keV to 1 MeV photons

P8: Simplified ^{3}He instrument in a consistency jig

The set of problems covered photons, neutrons, electrons and protons. None of the problems were very simple, but P3 on proton eye therapy was beyond the capabilities of most codes at that time, and P6 simulating a neutron calibration room with a shadow cone was computationally very demanding. The results are summarized in four publications (Tanner et al., 2004, Gualdrini et al., 2005, Siebert et al., 2006, Price et al., 2006) and were discussed in detail at a workshop hosted by ENEA in Bologna, Italy in 2003 (Gualdrini and Ferrari, 2004). The proceedings of that workshop provide the most complete analysis and discussion of this, probably the first ever large scale intercomparison of computational methods in dosimetry. They include additional material on uncertainties associated with numerical methods.

Full discussion of all of the problems is not possible here. Some problems were clearly more demanding or less interesting than others, which led to lower uptake. Conversely, some attracted a lot of participants.

The scale of the problems encountered by some participants can be seen from the divergent solutions submitted for a TLD albedo dosemeter problem. This simple problem was based on a 4-element design widely used in Germany (Piesch and Burgkhardt, 1988), that had simple geometry and well-defined materials. The participants needed to calculate the response to both photons and neutrons with the dosemeter mounted on a simple slab phantom. Photon response calculations were much more reliable than those for neutrons, which showed divergences of up to three orders of magnitude over and under estimation (Fig. 6.3).

The conclusions from the QUADOS report were:

- The intercomparison drew solutions from a wide range of countries and areas of work.
- Approximately 80 participants took part overall.
- MCNP family codes dominated amongst the codes used.
- Agreement with the authors' solutions was in general very satisfactory.
- Some solutions had large systematic errors.
- Many participants required substantial help to get "good agreement" with the "authors solutions".
- Statistical uncertainties were almost always quoted, but there was little other consideration of uncertainty.

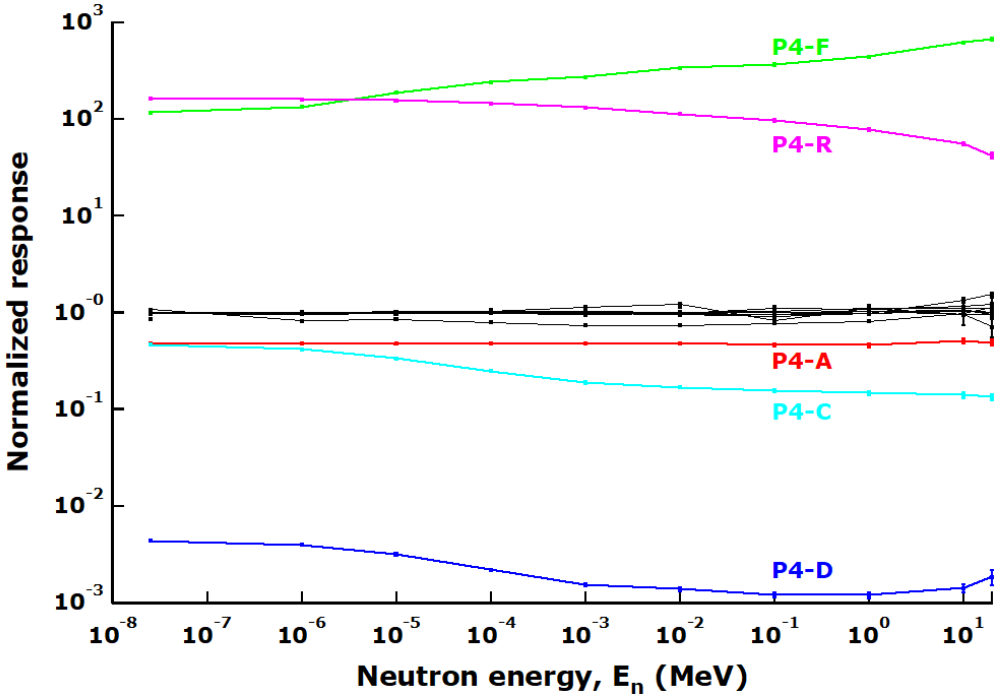

Fig. 6.3: Normalized neutron response for all 17 solutions submitted for the response of a 4-element TLD albedo dosemeter. "Good" solutions are depicted in black.

The work performed within the QUADOS Concerted Action made it clear that further intercomparisons were warranted to try to improve standards in the application of computation methods in the radiation protection and dosimetry community.

6.4. CONRAD WP4 Uncertainty Assessment in Computational Dosimetry

The success and outputs from the QUADOS Concerted action led to a follow up project in the CONRAD EURATOM VI Framework Programme, CONRAD WP4 Computational Dosimetry. The main task of this project team was to conduct an intercomparison: "Uncertainty Assessment in Computational Dosimetry: A comparison of Approaches." The Full Members of this team were: Gianfranco Gualdrini, ENEA, Italy (Chairman), Robert Price, City University, UK (Secretary), Bernd R. L. Siebert, PTB – Germany; Bernd Großwendt, PTB – Germany; Maria Zankl, GSF – Germany; Jean Louis Chartier, – France; Michel Terrissol, CPAT-Toulouse – France; Loic de Carlan, CEA-Saclay France; Rick Tanner, HPA – UK; Ivo Kodeli, NEA-DB France; Stefano Agosteo, Politecnico Milano – Italy; Jean Marc Bordy, CEA – Saclay – France; Jose Maria Gomez Ros, – CIEMAT – Spain; Sofia Rollet, ARCS Austria; and Frank Schultz, TU Delft – The Netherlands.

The 8 problems set spanned two sets of problems, those which were more computationally demanding, and those that were considered suitable for more detailed uncertainty analysis:

- Stochastic Uncertainties only
    - P1 Proton Recoil Telescope
    - P2 Bonner Sphere Spectrometer
    - P3 SIGMA neutron field

- Expressing overall uncertainty
    - P4 Photon irradiation facility
    - P5 Manganese Bath
    - P6 Iron sphere experiments
    - P7 Energy response of a RADFET
    - P8 Recoil proton telescope

These problems were summarized in two papers (Gualdrini et al., 2008, de Carlan et al., 2008), along with a third that discussed an intercomparison performed by members of EURADOS WGs 6 (Computational Dosimetry) and 7 (Internal Dosimetry); these papers were presented at the 2007 EURADOS Winter School in Madrid.

6.4.1 P2 Bonner Sphere Spectrometer

P2 of this set returned to the original intercomparison and focussed on Bonner spheres, in this case asking the participants to simulate the responses of a realistic Bonner sphere set (Fig. 6.4) and then unfold the spectrum of a ^{252}Cf source in a realistic calibration laboratory using their own response functions (Fig. 6.5). Thirteen participants were able to tackle this Monte Carlo problem but only nine of them could complete the subsequent unfolding. The results showed a significant scatter in the calculated response functions, but a bigger scatter in the unfolded fields (Fig. 6.5).

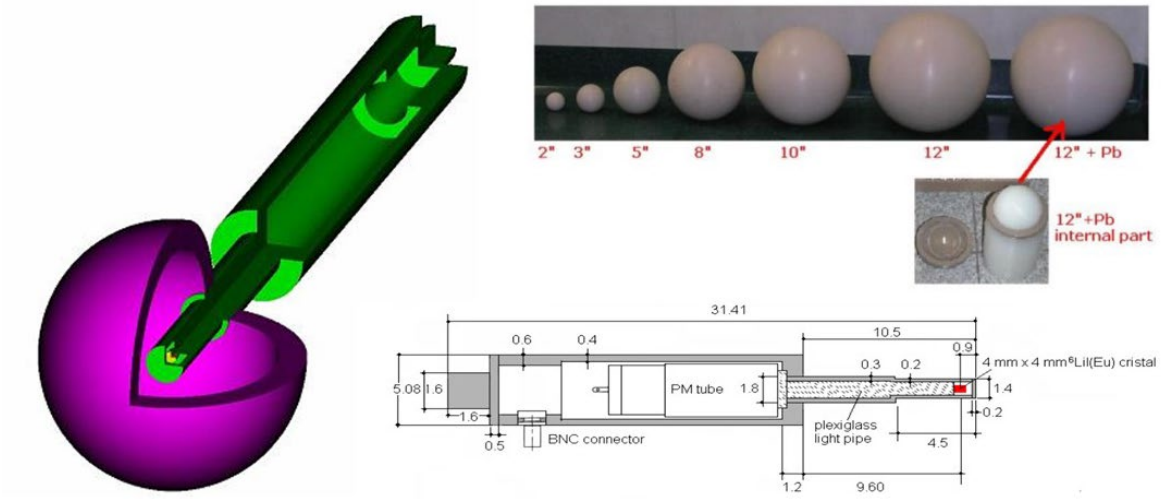

Fig. 6.4: A Bonner sphere set, a drawing of the detector and the Monte Carlo geometry.

6.4.2. CONRAD Conclusions

The problem set was much more demanding than in the QUADOS Intercomparison. This had led to considerable issues with agreeing the "authors'" solutions for comparison with the submitted solutions. However, the improved capability evident in the results showed that the participants were more competent than at the time of the earlier intercomparison.

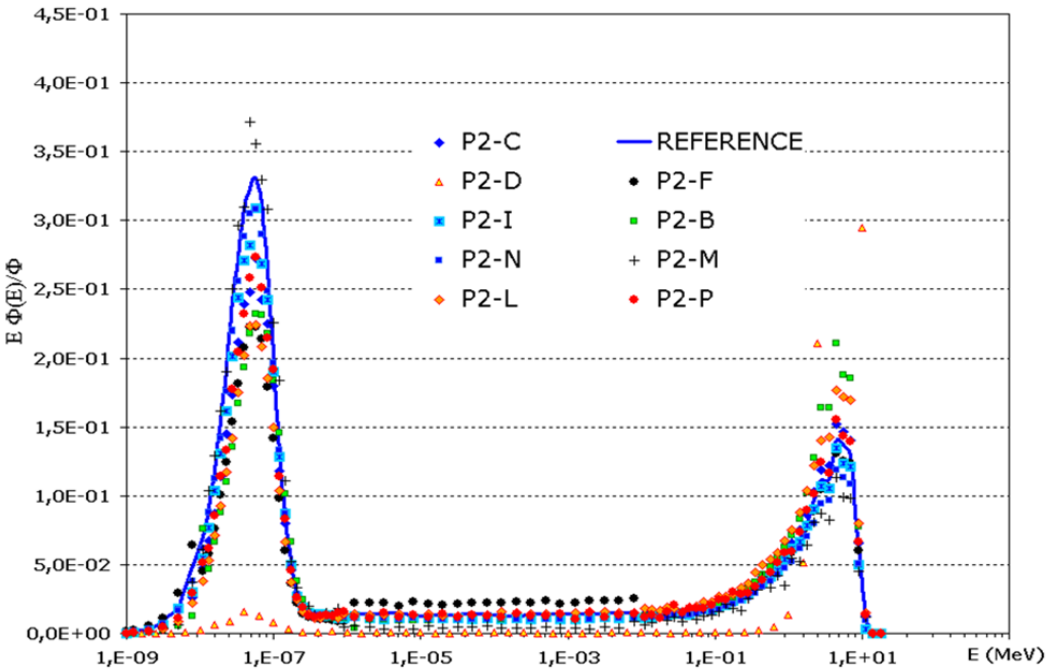

Fig. 6.5: The fluence spectrum unfolded by the participants in CONRAD P2.

The organizing group lamented the dominance of a single code in the solutions. At the time of this intercomparison, the MCNP family of codes were becoming dominant, whilst previously well-established codes such as the EGS family, MCBEND and the home-made and deterministic codes were not much used. The greater usage of FLUKA, GEANT and PHITS had not really taken off, so it was a time interval when MCNP was very dominant. There was no implied criticism of MCNP intended, but the over-reliance in the community on a single code was not considered to be ideal.

Some good solutions were submitted for all problems. Despite the greater computational demands required of participants, there seemed less evidence that participants could not get their solutions to converge. However, there were still poor solutions submitted for all problems. The value of this follow-up intercomparison was evident in the results sets.

6.5. Intercomparisons conducted after the end of the CONRAD project

Following the CONRAD period of funding, EURADOS Working Group 6 continued to participate in and run intercomparisons. Reports on the most recent intercomparisons were published in a series of articles (De Saint-Hubert et al., 2021, 2022; Eakins et al., 2021; Gómez-Ros et al., 2021, 2022; Huet et al., 2022; Rabus et al., 2021b; Villagrasa et al., 2022; Zankl et al., 2021a, 2021b, 2021c). that have been collected in a virtual special issue of Radiation Measurements, on "EURADOS WG 6 Intercomparisons in Computational Dosimetry" (2022). An article from this special issue on the lessons learnt from these intercomparisons is reproduced as the last four sections of this chapter.

Three further intercomparisons conducted earlier and, hence, not included in the virtual special issue of Radiation Measurements, are described below in this section of the chapter. Two of these were run jointly with another Working Group: one with WG7, *Internal Dosimetry*, and the other with WG11, *High Energy Fields*. The third intercomparison on modelling of a linac was run by WG6, *Computational Dosimetry*.

6.5.1. Internal Dosimetry Intercomparisons (with WG7)

These intercomparison involved the use of voxelized phantoms for internal dosimetry problems and the modelling and measurement of a skull phantom contaminated with ^{241}Am (Vrba et al., 2014, 2015, Nogueira et al., 2015, Lopez et al., 2019). These experiments hence provided measured data for comparison with the Monte Carlo results. The computational dosimetry part of this comparison exercise was aimed at comparing approaches to using of Monte Carlo techniques in calibrating the detection efficiency of body monitoring systems. Three tasks of varying degree of difficulty had to be solved which all consisted in the simulation of the response of a detector and of the radiation emitted by a skull phantom. The simulations in the first task related to a specified detector and a well-defined semi-skull phantom, where all parameters entering the simulation were set, such as photon yield, material composition and geometrical dimensions. The second and third tasks required modelling of a real detector and an individual geometry of the skull phantom.

Fig. 6.6 shows as an example results from the first task for the spectral detection efficiency of the Germanium detector for photons up to 65 keV. The shaded area represents the range between the minimum and the maximum values reported by the participants, whereas the solid line represents the results of measurements. The large spread of results was due to seven of the 16 submitted solutions that were corrected by the participants after feedback on their results. With their revised results the overall dispersion between participants as well as the deviation from the measurements were significantly reduced (right panel of Fig. 6.6).

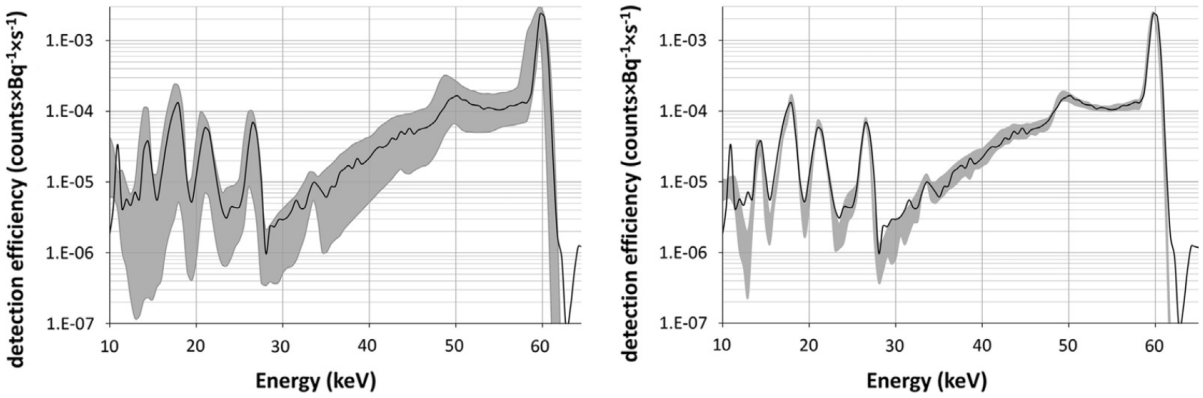

Fig. 6.6: Range of the detection efficiency results (grey shaded area) initially reported by the participants (left) and after correction of the results by 7 of 16 participants (right) compared to measured results (black line). From Radiation Physics and Chemistry, Vol. 104, Vrba, T. et al., "EURADOS intercomparison exercise on MC modeling for the in-vivo monitoring of Am-241 in skull phantoms (Part I)", 332–338, Copyright Elsevier (2014). Doi: 10.1016/j.radphyschem.2013.12.010. [License Number 5654721021136, License date Oct 23, 2023].

6.5.2. Bonner sphere unfolding for high energies (with WG11)

The intercomparison comprised four codes based on different unfolding techniques as well as an approach based on Bayesian parameter estimation. The unfolding methods were used to extract neutron spectra from measurements of secondary neutrons from cosmic radiation taken at the Environmental Observatory 'Schneefernerhaus' on the Zugspitze mountain in Germany. The Bonner sphere spectrometer used in the experimental reference had 16 measuring channels with ^{3}He

proportional counters. Apart from minor differences in height and position of the peaks, agreement was found for the shapes of the spectra obtained with different codes. Integral values of fluence and ambient dose equivalent rate were in excellent agreement with maximum of 5 % and 9 %, respectively. Measured and unfolded count rates agreed within uncertainties (Barros et al., 2014).

6.5.3. Linac modelling

The goal of this exercise was to probe the state of the art with Monte Carlo (MC) approaches to characterizing medical LINACs (Caccia et al., 2017). A further aim was to provide material for learning-by-doing self-training of novice MC users helping them to develop their skills in setting up a MC simulation of a real linear accelerator and performing a benchmarking dosimetric analysis by comparison with measured data (Caccia et al., 2020).

Participants had to solve two tasks. In the first task, the photon fluence spectra of a linear accelerator operated at CEA LIST Laboratoire National Henri Becquerel (LNHB) were to be simulated based on the known geometry and material composition of the linac head and limited information on the electron source. This corresponds to a typical scenario of the extent of information available from LINAC manufacturers. The outcome of the simulations of the photon field produced by the LINAC therefore also depends on assumptions to be made by the user about the properties of the electron source, where measurement data in a homogeneous water phantom under standard reference conditions were available for optimizing the electron-beam parameters.

Using phase space files of emitted photons simulated for the optimized configuration in the simulations for the second task, the relative absorbed dose in different dosimetric phantoms was to be calculated. The phantoms consisted of a water tank containing four different configurations of heterogeneous tissue equivalents (lung and/or bone). In contrast to the good agreement between the different simulated photon spectra emitted from the LINAC (Caccia et al., 2017), significant deviations were found in the local dose, particularly near interfaces between water and the tissue-equivalent materials of higher or lower densities (Caccia et al., 2017,2020).

6.6. Lessons learnt from recent EURADOS intercomparisons in computational dosimetry

This section of the present chapter of the EURADOS report is the reproduction of an article in the Virtual Special Issue of Radiation Measurements, on "EURADOS WG 6 Intercomparisons in Computational Dosimetry" published in Radiation Measurements, Vol. 156, Hans Rabus, Maria Zankl, José Maria Gómez-Ros, Carmen Villagrasa, Jonathan Eakins, Christelle Huet, Hrvoje Brkić, Rick Tanner, "Lessons learnt from the recent EURADOS intercomparisons in computational dosimetry", 106822, Copyright The Authors. Published by Elsevier (2022) under Creative Commons Attribution License (CC BY). Doi: 10.1016/j.radmeas.2022.106822. The article has been edited to match the layout of this report, abstract and introduction have been omitted, one figure has been moved from the supplement of the published article to the main text, the supplement has been removed, and the list of references has been merged with those of the rest of the chapter.

6.6.1. Overview of the exercises covered by the special issue of Radiation Measurements

The exercises can be divided roughly into two classes depending on the nature of their solutions. The first class comprised six exercises on the use of ICRP computational reference phantoms (ICRP, 2009; Zankl et al., 2021b) and one on unfolding of neutron spectra from Bonner sphere measurements (Gómez-Ros et al., 2022). The former will be referred to as "voxel-phantom exercises" throughout this article, the latter as the "Bonner sphere exercise". Despite the quite different nature

of the problems to be solved, these exercises had in common that they required the application of well-known methodologies and established computational tools. This allowed the organizers to establish prior reference solutions that could be used to validate the results subsequently submitted by the participants in the exercise.

The second class are exercises where no reference solutions could be established, since one of the objectives of the exercises was evaluating the possible influence of different cross-section models in the codes used by the participants. Two of these exercises were code intercomparisons, one dealing with the calculation of microdosimetric and nanodosimetric quantities (Villagrasa et al., 2019, 2022), and the other with the effects of gold nanoparticles on dose deposition at the microscopic scale (Li et al., 2020a, 2020b; Rabus et al., 2021b, 2021c); the former is called the "uncertainty exercise" in this article and the latter the "nanoparticle exercise". The other two exercises in this class dealt with out-of-field dose calculations. One was about calculating the dose to the foetus during maternal proton therapy treatment and the other was about calculating the secondary neutron fluence. (De Saint-Hubert et al., 2021, 2022). These two exercises are referred to as "foetus dose exercises".

It is important to note that none of the exercises was intended to be a code competition. Rather, the aim was to investigate the dispersion of results when the same problem was solved by different people using different approaches and different codes or the same code with different options. The first class of exercises focused on identifying the state of the art in the application of common methods in computational dosimetry. The second class was more exploratory in nature and aimed to assess the state of the art in terms of the capabilities of codes and approaches. All classes contained tasks of different complexity, and thus different demands on the participants' skills.

The exercises were organized and run by ad-hoc teams composed of EURADOS WG 6 members. In general, the preparation of the exercises involved independent simulations by several team members, with their respective results then cross-referenced to identify potential pitfalls in the proposed exercise definitions and to check whether the tasks were solvable based on the information to be provided. For the exercises with reference solutions, the results of these test simulations were also used to establish those values, (e.g., by taking the mean), as well as gain a handle on the typical levels of uncertainty that may be considered acceptable for them.

In some exercises, templates for reporting results were also provided to the participants.

6.6.1.1. ICRP reference voxel phantom exercises

Of the voxel-phantom exercises, two involved exposures to an external point source, emitting either ^{60}Co gamma photons or 10 keV neutrons respectively (Huet et al., 2022). The task to be solved was to calculate the organ absorbed doses and the effective dose for a given exposure duration and activity of the source.

A third voxel-phantom exercise also dealt with point source geometries, but for cases of typical X-ray examinations (Huet et al., 2022). Here the task was more complex, as participants were required to determine the position of the radiation point source in relation to the phantom. In addition, the results were to be presented as conversion coefficients to organ absorbed doses, both from air kerma and kerma area product. This exercise was thus linked to a potential practical application in which the latter quantities are determined as part of the quality assurance of radiological equipment, and the conversion coefficients sought would enable an assessment of the dose absorbed by the patient during the X-ray examination.

The fourth voxel-phantom exercise considered a uniform planar source of 60 keV photons beneath the phantom (mimicking ground contamination by ^{241}Am) and required participants to calculate organ absorbed dose rates and the effective dose rate for a given area density of the emission rate (Eakins et al., 2021). In the fifth voxel-phantom exercise, a mixed radiation field of gaseous ^{16}N was considered, emitting beta and high energy gamma radiation from both inside (lung) and outside the human body (Gómez-Ros et al., 2021); the ratios of organ equivalent dose rates to activity concentration were to be determined.

The most extensive voxel-phantom exercise involved an idealized case of internal dosimetry (Zankl et al., 2021c). For the sake of simplicity, hypothetical radionuclides were considered that were uniformly distributed in specified organs and emitted monoenergetic photon or electrons. Here, absorbed fractions and specific absorbed fractions of energy in the "source" organ and in specified "target" organs were to be determined as well as *S*-values for the resulting source and target organ combinations for two specific radionuclides.

6.6.1.2. Bonner sphere spectra unfolding exercise

The tasks were defined by the counts measured by a set of twelve Bonner spheres of different diameters and known sensitivities (as determined by the organizers with radiation transport simulations), located at a measurement point in one of four known environments: inside the bunker of a medical linac; near a radioactive source; in a simulated workplace field within a neutron calibration facility; or outside a nuclear power plant. The count rates measured by the Bonner spheres were determined by the organizers through Monte Carlo radiation transport simulations of the respective complete measurement setup for each Bonner sphere within its environment. In addition, and to recreate a realistic situation, the count rate from one of the Bonner spheres in one of the scenarios was intentionally given an incorrect value in order to test the participants' ability to detect an erroneous measurement and exclude it when applying the deconvolution procedure (Gómez-Ros et al., 2018, 2022)

6.6.1.3. Micro- and nanodosimetric uncertainty exercise

In its first phase, this exercise included a microdosimetric and a nanodosimetric intercomparison (Villagrasa et al., 2019). In the frame of the former, frequency distributions of specific energy were to be determined within a microscopic water sphere for different distributions of a low-energy electron emitter with an energy spectrum derived from the internal-conversion Auger emitter ^{125}I. In the nanodosimetry part, ionization cluster size distributions were to be determined in target spheres of different sizes located at different distances from a point source with the same energy spectrum as in the microdosimetry part. A sensitivity analysis was also performed on the variation of inelastic cross-sections and its consequences for the calculated ionisation cluster size distributions (Villagrasa et al., 2022). In the second phase of the exercise (in preparation), the focus will be on a comparison of the cross-section datasets for low-energy electron transport and a consideration of their impact on the dispersion of nanodosimetric results.

6.6.1.4. Nanoparticle exercise

In the nanoparticle exercise, the dose enhancement from a gold nanoparticle, as well as the energy spectrum of electrons emitted from it, were to be determined when irradiated with two low-energy X-ray spectra. The geometry was simply a gold sphere in water irradiated with a parallel beam from a plane photon source, the cross-sectional area of which was slightly larger than that of the nanoparticle. Two different nanoparticle diameters were considered, and the dose enhancement

was to be determined in spherical water shells around the nanoparticle. (Li et al., 2020a, 2020b; Rabus et al., 2021b, 2021c)

6.6.1.5. Foetal dose during maternal proton therapy

This exercise consisted of two parts. The first part dealt with the effects of different calculation phantoms for pregnant women, and different code versions of MCNP, on the predicted dose to the foetus during maternal brain proton therapy. The second part dealt with the dependence of the secondary neutron spectra on the Monte Carlo radiation transport codes and nuclear models that were used, and their effects on the calculated and measured neutron doses during proton therapy. (De Saint-Hubert et al., 2021, 2022)

6.6.2. Experiences from the exercises

6.6.2.1. Observations on participants' results

In general, the ensemble of participants' results that were submitted initially showed a large scatter. In the exercises for which a reference solution was available, excellent agreement within the expected statistical fluctuations was found in some cases, while others showed significantly larger deviations, which in some individual cases ranged by up to several orders of magnitude. For the tasks without a reference solution, a subset of the reported results also agreed with each other to some extent, while others deviated significantly from this group. In both classes of exercise, the occurrence of extreme outliers was not correlated with the complexity of the problem.

Some of the deviations were attributable to simple errors, such as copy-and-paste mistakes or incorrect arrangement of the results in the given template. Others resulted from misunderstanding how the final results should be normalised (e.g., normalising to the correct quantity but at a different distance from the source than was required). In the voxel-phantom exercise for the case of X-ray examinations, some participants normalized to the value of air kerma free in air at a specific distance from the source or to the entrance surface dose (which includes backscatter) instead of to air kerma free in air at the skin as was requested. In the microdosimetric and nanodosimetric intercomparisons, the normalisation to 'one decay of the electron source' was not always understood by the participants and was also sometimes difficult to implement for some Monte Carlo codes. The use of a logarithmic scale for the microdosimetric quantity (specific energy distribution) also caused problems with proper normalisation.

Many major deviations were caused by the fact that the participants' simulations deviated from the specifications in terms of geometrical dimensions or the quantities to be determined. One example of this was the "nanoparticle" exercise, where only two out of eleven participants implemented the requested geometry correctly, which consisted of a gold sphere irradiated in water by a collimated parallel photon beam of given dimensions. Another example was the voxel phantom exercise on internal dosimetry, where some participants used organ masses that included blood instead of those given in ICRP Publication 110, as was stated in the exercise definition. In some of the voxel-phantom exercises, the choice of the location of the source was also sometimes a problem due to deviation from the correct reference point (e.g., the edge of the phantom array instead of the phantom's skin).

Other causes of major deviations were that some participants were not familiar with certain concepts, such as the normalization quantity "kerma area product" (in the voxel-phantom X-ray exercise) or effective dose; mistakes for the latter included not applying tissue weighting factors

correctly, not averaging and summing over the defined set of organs, neglecting to sex-average, or neglecting to apply the correct energy-dependent radiation weighting factor for neutron exposures.

In the voxel-phantom exercises, many participants had problems applying the method recommended for bone marrow dosimetry in (ICRP, 2010). This finding stimulated writing an article to better explain this approach (Zankl et al., 2021a).

As already mentioned, participants whose results differed from the reference solution (class 1) or from the majority of other participants' solutions (class 2) were informed of this fact and asked to revise their solutions. Not all contacted participants responded to this invitation or provided the requested information on details about their simulations.

Of those participants who submitted a revised solution, some did not indicate what they had changed in their computational procedure to arrive at their revised results. This therefore does not give any additional insight into possible similar errors to be expected in future similar exercises, or hints that could have been communicated to the other participants.

In the nanoparticle exercise, where some inconsistencies became evident after the first publication of the results (Li et al., 2020a) and required a thorough re-evaluation (Li et al., 2020b), consistency checks provided clear indications of the causes of the discrepancies for some results. Nevertheless, some of the participants concerned did not provide revised solutions (Rabus et al., 2021b). However, it must be also stressed that the majority of participants were very supportive of the re-analysis of the results and were eager to clarify the origin of the discrepancies found initially.

6.6.2.2. Issues with omitted quality assurance of results

Many of the anomalies found in the reported data could have been detected by the participants themselves, e.g., through simple plausibility checks of their results. Examples are briefly discussed in the following.

For example, a very general plausibility consideration is that if the irradiation conditions are quite homogeneous, it may be expected that all organ doses will be of broadly similar magnitudes; a single organ dose result differing by several orders of magnitude from the rest of a given participant's dataset ought therefore to be immediately apparent to them as being potentially erroneous. Similarly, if multiple energies are considered, it is unlikely that the value for a single intermediate energy will be entirely outside the range of values for all other energies.

In the Bonner sphere exercise, there were cases of reported results with negative values for the neutron fluence. These physically impossible values, as well as anomalous spectral shapes, could have been identified by simply plotting the results. Some of the reported spectra differed from the reference solutions by several orders of magnitude; such anomalies could have been easily detected if the unfolded spectra had been convolved with the given sensitivities of the Bonner spheres, to verify that the given count rate was then achieved.

In the voxel phantom exercise for internal dosimetry, a simple plausibility check would have been that the absorbed fraction for electrons and low-energy photons must be close to unity in a source organ and quite small for other organs, since these radiations have a short range in condensed matter and therefore deposit their energy close to the point of release. Moreover, some participants in this exercise reported results for absorbed fractions and specific absorbed fractions for which the ratio of these two quantities varied between different energies of the particles emitted from the (monoenergetic) source. However, since this ratio is simply the mass of the organ, it cannot depend on the energy.

In addition, for many of the tasks in the voxel phantom exercises, literature values are available for fairly similar exposure conditions that could have been used for comparison, at least as a first approximation to indicate the expected magnitudes of the results.

When dealing with voxel phantom simulation, one of the simplest checks might be to visualise the problem in order to ensure the proper positioning of the beam, though it is noted that some software packages struggle due to the sizes of these input files. If one is using any variance reduction it should also be ensured that simulations with and without application of these techniques reproduce the same results, albeit with differing statistical uncertainties.

6.6.2.3. Issues with exercise definitions

In some cases, inadequacies in exercise definitions became apparent while they were already running. In the nanoparticle exercise, for example, one of the quantities to be reported by the participants was the energy spectrum of electrons "in spherical shells" around the nanoparticle, with the radii of the bounding spherical surfaces given.

Most of the participants interpreted this physically undefined quantity as the energy distribution of the electrons entering the respective volume. However, one participant determined the energy distribution of the balance of the number of electrons traversing the surfaces of the respective volume and withdrew her results on the assumption that the observed negative frequencies indicated an error that she could not locate.

Another problem with this part of the nanoparticle exercise was that there was no default energy binning, so participants chose very different values for the bin size, with some using logarithmic binning and others using linear binning. The large statistical variations in the results obtained with small energy bin sizes masked the variations between the different results when plotted together (Li et al., 2020a).

In the exercise on Bonner sphere spectrum unfolding, it was found during the analysis that in one of the scenarios considered, there was an interference of the Bonner sphere response due to backscattering of neutrons from a nearby concrete wall (Gómez-Ros et al., 2018).

In the voxel phantom exercises featuring ^{60}Co photons and 10 keV neutrons, the instruction given to participants for the location of the point source was to place it '100 cm from the surface of the chest', which could be interpreted differently. In response, the organizers performed small sensitivity analyses to quantify the impact from the ambiguity of this parameter, the outcomes from which were used to imply appropriate 'tolerances' that could be applied to the submitted results (Huet et al., 2022).

The voxel phantom exercise on internal dosimetry was not wisely designed in several respects. The tasks to be solved were too extensive, which also made evaluation challenging and led to delays in feedback to the participants. For electrons and low-energy photons, the source and target organs were sometimes too far apart, which led to very large statistical uncertainties even in the reference solution. Therefore, the degree of deviation between participant and master solutions could not be reliably quantified in some situations.

In the uncertainty exercise, the use of a multi-energy electron source that was similar to the ^{125}I decay but did not take into account the variability of the actual decay, complicated the understanding of the problem on one hand and, on the other hand, did not favour the analysis of the sensitivity study on the variation of the cross sections. Indeed, the use of monoenergetic electrons would have helped in both aspects.

In the foetal dose exercise, atomic numbers of the elements, mass numbers of the nuclides, and cross-section identifiers had not been fixed for all materials used in the simulations, so participants made their own (different) choices, which caused some of the discrepancies initially noted.

6.6.2.4. Issues with the timetable of the exercises

Most exercises were planned with a timetable, which in almost all cases proved to be too ambitious and optimistic. This was partly because for many exercises the initial number of participants was lower than was expected and considered adequate for the purpose, so submission deadlines were postponed several times to increase participation after further publicity for the exercises. Further deadline extensions became necessary at the request of the participants.

After an initial analysis of the submitted solutions, participants whose results differed by more than expected from either the reference solution or from most other participants' solutions (as appropriate) were informed on this fact and invited to revise their solutions. Deadlines for the submission of revised results also had to be postponed several times.

As a result, the total duration of the exercises exceeded the typical length of stay of junior researchers at a given institute, making it difficult, if not impossible, to follow-up on abnormal results in some cases.

6.6.3. Lessons learnt

6.6.3.1. Problem specification

The participants, as well as the organisers of the exercises, are committed to EURADOS and the intercomparisons in addition to their daily work. Therefore, the topics of the intercomparison exercises must be relevant to the participants' fields of work, and the tasks to be solved should not be overly demanding in terms of setup time. CPU resource requirements may also need to be considered but should generally be less of an issue.

To meet the workload requirements, some of the exercises were designed with simplified idealistic geometric setups and irradiation conditions. Examples include the voxel phantom exercises for monoenergetic point sources, the uncertainty exercise in micro- and nanodosimetry (idealised energy spectrum), and the nanoparticle exercise (simplistic geometry). These simplifications have sometimes raised concerns among reviewers about the usefulness of the respective comparisons but seem justified given the aforementioned time constraints.

Regardless of the complexity of a task, a complete description of the problem to be solved with all relevant information must always be given. For Monte Carlo simulation exercises, this means that the radiation source, simulation geometry and materials must be comprehensively specified. On the other hand, it should generally not be specified exactly how the Monte Carlo simulation, or the unfolding are to be carried out. The path to the solution, as well as the tools to be used, must be decided at the discretion of the participant. The participant must determine, for example, whether and which variance reduction techniques can or should be used, whether the transport of secondary charged particles should be simulated or how the thermal neutron transport should be performed.

However, depending on the aim of the exercise, a more detailed specification of intermediate steps or procedures may be advisable. For instance, whenever the performance of codes or their differences is to be assessed, it may be wise also to specify some of the aforementioned aspects of

the simulations to ensure that the differences between results from different participants only reflect the differences in the codes that one is interested in.

6.6.3.2. Reporting of results

The task definition should include very precise instructions for reporting results, and templates should be provided where possible. Providing such a template, where the participants were requested to fill in their results in a pre-defined format, not only helps clarify exactly what output is required from them in each case, but also greatly facilitated the evaluation of the results in the respective exercises. This is especially important when spectral information is to be reported, where a lack of specification of bin division can make synopsis quite cumbersome when different participants use different bin sizes and/or linear and logarithmic equidistant bins.

In addition, asking for redundant information can help to identify potential problems with participants' data. Examples of this were: the voxel phantom exercise for internal dosimetry, where absorbed fractions and specific absorbed fractions were to be reported (differing by only one factor, i.e., organ mass); or the voxel phantom exercise for the X-ray examinations, where the results were to be reported normalised to both kerma free-in-air and kerma area product, which again differ by only one factor. In the case of the nanoparticle exercise, only reporting of results normalised to the number of primary particles was required. If normalisation to the area density of the emitted primary photons from the source had also been reported, the incorrect implementations of the simulation geometry would have been detected much earlier during the exercise.

6.6.3.3. Timing of the exercise

Regarding the problems encountered with non-responding participants at the revision of results stage, it is planned to set up rules in future exercises to get a more formal commitment from participants. The rules to be established concern deadlines, participation in the feedback loop, and requirements for co-authorship to potential manuscripts.

In addition, more timely feedback to the participants might improve their preparedness to disclose details of their computational procedures and improvements. Long feedback intermissions make it difficult for the participants to recall exactly what was done and even what the exercise was about. It should be kept in mind that the organizers, as well as all participants, are performing these exercises alongside their daily duties.

In the reanalysis of the nanoparticle exercise, a set of hierarchical MS Excel templates were used that allowed a fast assessment of the internal consistency of the results reported by participants (in an Excel-template provided to them) as well as a 'live' synopsis via hyperlinks. As an illustration of this approach, Fig. 6.7 show a screenshot of the "Synopsis" worksheets with easy-to-assess graphs and calculated figures of merit (integral quantities normalised so that their expected values are close to unity).

Using these templates to assess the consistency of a participant's results took only a few minutes and required only copying and pasting the results from the Excel templates completed by the participant into the template used for the analysis. In many cases, this enabled feedback in less than an hour. Of course, it was more time-consuming to identify the more sophisticated deviations from the exercise specifications.

Another issue with timing is that calculations with voxel phantoms may require large amounts of time. With some codes, even the visualisation of them can take up to several hours, and the

production calculations even weeks. Some codes have ability to skip the geometry check at the beginning of production calculations (e.g., DBCN card in MCNP) and in this way speed up the calculations significantly.

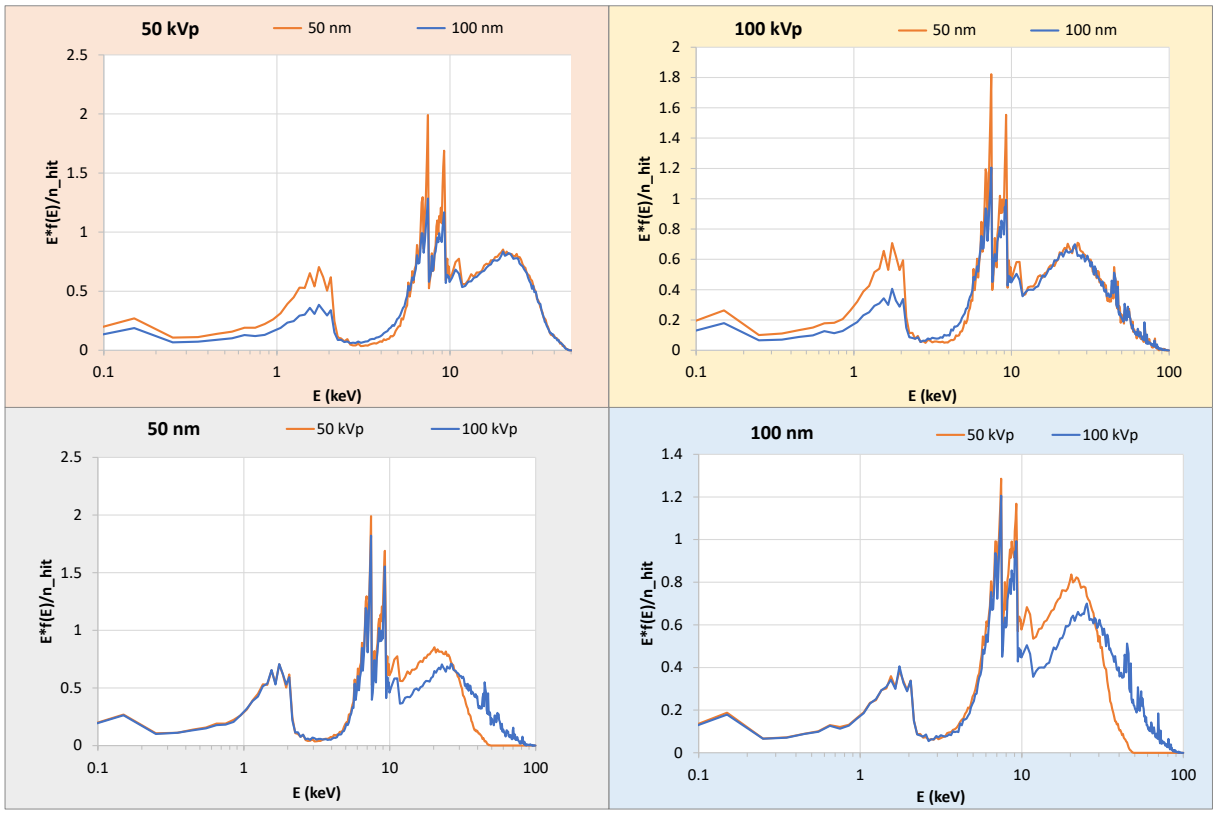

Fig. 6.7: Screenshot of the section with the diagrams in the "Synopsis" worksheet of the Microsoft Excel template used in the nanoparticle exercise to test the internal consistency of the results reported by a participant for the energy spectrum of electrons emitted from the gold nanoparticle for the four combinations of nanoparticle size and X-ray spectrum. The plots show comparisons of the energy distributions of the number of emitted electrons (normalised to the average number of photon interactions in the gold nanoparticle). The two plots in the upper row compare different nanoparticle sizes for the same radiation quality, where similar values are expected for high-energy electrons and higher frequencies for low-energy electrons for the smaller nanoparticle. The bottom row shows the comparison for the same nanoparticle size and different energy spectra, where one expects similar values for low electron energies because the range of these electrons is smaller than the size of the nanoparticle. The data shown have been calculated from the participants data by rebinning and normalization to the expected number of photon interactions in the nanoparticle. They are plotted in “microdosimetry style” such that the area under the curves is proportional to the number of electrons emitted per photon interaction in the respective energy interval. The data for emitted electrons correspond to one of the cases where the participant correctly applied the required geometry. Examples of how different the respective graphs look for the case of deviating geometry can be found in Rabus et al. (2021c).

6.6.3.4 Quality assurance of results

As indicated in Section 6.6.2.2, in all exercises some of the participants seemed to have submitted their results without first carrying out adequate quality control of their solutions, e.g., by simple plausibility checks or by comparison with literature data, if available. Approaches such as the one mentioned in Section 6.6.3.2 could allow for faster identification of outliers and more timely feedback to participants. This could alleviate some of the problems, such as where there was a lack of response from participants following feedback regarding abnormal results.

However, a significant degradation in the quality of results may persist, as the evolution of many computational tools towards greater ease of use also allows their use without a certain level of expertise, which may still be required for meaningful results. Interaction with some exercise participants who reported unreasonable results revealed a lack of understanding of several fundamental aspects. For example, that the results of calculations are not just numbers, but physical quantities (which have dimensions).

Some participants were also unaware that there are different ways of specifying the categorical variable of a histogram (lower or upper limit of the bin or the bin centre), which can vary between different codes and affect the comparison of results, such as when reported with different definitions of the meaning of the values on the x-axis. This could be countered by requiring both the lower and upper bin limits to be reported.

There were also cases where participants determined ratios with a finer bin size than specified in the task, and then re-binned their results for reporting by averaging the ratios over the larger bins instead of calculating the ratio between the sum of the numerators and the sum of the denominators. Detection of such elementary mistakes requires access to the original results, so their origins were not always immediately apparent to the organizers.

Considering that most exercises will lead to publications in the form of EURADOS reports or journal articles, compliance with the principles of FAIR data (an acronym for findability, accessibility, interoperability, and reusability, (Wilkinson et al., 2016)) is also a matter that should be given more emphasis in the future. This is, of course, the responsibility of each participant, but appropriate commitments can be included in the application forms. Examples are shown as Figs. 1 and 2 in the Supplement of Rabus et al., (2022). As a minimum requirement, participants should provide documentation on where the following files are stored and backed up:

- data files containing the reported results
- data files with the raw simulation output
- files used for their production (material data or other input files, code, etc.)
- log files and other supplementary output files of the simulations.

This information is essential when participants need to review their work for possible errors. However, in the exercises, delayed responses from participants were sometimes explained by difficulties in finding data, uncertainty about which version of a code was used, and similar such problems. Therefore, it may be useful for the organisers to collect this information – or even the files containing the metadata of the simulations – as part of the reporting of the results. This might be the case especially for participants who are inexperienced users of simulation codes, who may not be aware that the log files etc. generated by their codes contain information that complements their simulation results and is important for their quality.

It was not uncommon for files of original simulation results, which were shared by participants with the organisers during the feedback loops, to contain only columns of numbers. A header indicating which quantities are listed and which units have been used, and ideally also containing information on the code used and its version, as well as the date when the file was written, would be minimum requirements for the useability of these data files. In addition, the aforementioned auxiliary information is also needed.

6.6.4. Conclusions

Beyond doubt, the reported EURADOS exercises are beneficial to the field of computational dosimetry. They directly contribute to the training of the participants by improving their computational procedures through feedback with the task organisers. They lead also to the availability of representative dose values for various exposure conditions that may aid future novice users in the quality assurance of their methods. In addition, they also provide a snapshot of how well (or otherwise) the computational techniques are being applied within the community in general, and how well some of the concepts recommended by organizations such as ICRP are understood; the observed difficulties in correctly defining and evaluating effective doses (Eakins et al., 2021; Huet et al., 2022), or in determining bone marrow doses (Zankl et al., 2021a), are clear examples of the latter.

The obvious question of what could be done better in future exercises has been partly addressed in Section 6.6.3. A general answer to this question is not easy since it depends on the objective of the exercises. The question will therefore continue to be the subject of discussion within EURADOS Working Group 6 when new exercises are prepared.

To avoid participants wasting their time on the tasks of an exercise in cases where they are prone to give incorrect results, due to a wrong idea of the task or ignorance of the dosimetric quantities to be determined, several modifications of the exercises can be considered. One could be to define explicitly the dosimetric quantities and normalisation quantities to be used. Another possibility would be to include in the definition of the task a list of checks to be made by the participants on the results, or even provide them with templates like those used in the reanalysis of the nanoparticle exercise.

Such changes to the exercises would mitigate the risk of potential errors by the participants. However, while this closer guidance may lead to improved results, this better agreement will only reflect the participants' capability to follow detailed instructions and not their actual state of expertise or their performance in real-world applications. Moreover, concepts like effective dose are widely used and already well-defined elsewhere; arguably, it should not therefore be the role of EURADOS WG6, which focusses on computational dosimetry, to coach radiation professionals on the basic concepts that underpin radiological protection.

Most of the exercises were the types of tasks that the participants may be confronted with in their professional activities or in research. Generally, they then would have to perform the simulation or unfolding, and calculate the dosimetric quantities of interest, without specific guidance. A supervisor of an early-stage researcher, or a reviewer of potential papers arising from such work, can be a source of feedback that hopefully reveals major non-plausibilities in the results, if any. However, as discussed by (Rabus et al., 2021c), these potential quality filters often seem to have failed for simulation studies on nanoparticles so far.

A better option could therefore be to create a questionnaire to assess the knowledge of the participants, and then give more detailed instructions to the less experienced participants. One could also start the exercise with a webinar explaining what is expected, what participants should do, and explaining the importance of quality assurance. A recording of the webinar could also be made available on the EURADOS website so that participants who join the exercise later can refer to it.

Another potential improvement for some of the exercises, if repeated, could be to include several reporting steps in the exercise. For example, in the voxel phantom exercise for the X-ray examinations, participants could first need to report their results for the position of the radiation source in relation to the phantom; they could then get feedback if it is outside the uncertainty band of the reference value and be invited to report a revised value. On request they could also get the correct positions as feedback and run their simulations for these. Alternatively, such future exercises could have a first step with as few specifications as possible, a second with plausibility checks to be performed by the participants, and a third with feedback on the submitted results and a request for revision.

6.7. References

Alevra, A., Siebert, B., Aroua, A., Buxerolle, M., Grecescu, M., Matzke, M., Perks, C., Schraube, H., Thomas, D., Zaborowski, H., 1990. Unfolding Bonner-Sphere data: a European intercomparison of computer codes. Report PTB-1, 22-90-1.

Barros, S., Mares, V., Bedogni, R., Reginatto, M., Esposito, A., F. Gonçalves, I., Vaz, P., Rühm, W., 2014. Comparison of unfolding codes for neutron spectrometry with Bonner spheres. Radiation Protection Dosimetry, 161, 46–52. doi: 10.1093/rpd/nct353.

Bramblett, R. L., Ewing, R. I., Bonner, T., 1960. A new type of neutron spectrometer. Nuclear Instruments and Methods, 9, 1-12.

Broggio, D., Bento, J., Caldeira, M., Cardenas-Mendez, E., Farah, J., Fonseca, T., Konvalinka, C., Liu, L., Perez, B., Capello, K., Cowan, P., Cruzate, J.-A., Freire, L., Gómez-Ros, J.-M., Gossio, S., Heide, B., Huikari, J., Hunt, J., Kinase, S., Kramer, G.H., Kurihara, O., Kyrieleis, A., Lebacq, A.-L., Leone, D., Li, C., Li, J., Mihailescu, L.-C., Moraleda, M., Navarro, J.-F., Oliveira, C., Puerta, N., Reichelt, U., Simões, C., Sommer, D., Takahashi, M., Teles, P., Vanhavere, F., Vrba, T., Franck, D., Gualdrini, G., Lopez, M.-A., 2012. Monte Carlo modelling for the in vivo lung monitoring of enriched uranium: Results of an international comparison. Radiation Measurements, 47, 492–500. doi: 10.1016/j.radmeas.2012.04.020.

Caccia, B., Le Roy, M., Blideanu, V., Andenna, C., Arun, C., Czarnecki, D., El Bardouni, T., Gschwind, R., Huot, N., Martin, E., Zink, K., Zoubair, M., Price, R., De Carlan, L., 2017. EURADOS intercomparison exercise on Monte Carlo modelling of a medical linear accelerator. Ann. Dell Ist. Super. Sanita, 53, 314–321. doi: 10.4415/ANN_17_04_07.

Caccia, B., Blideanu, V., Le Roy, M., Rabus, H., Tanner, R., 2020. A model validation scheme for Monte Carlo simulations of a medical linear accelerator: geometrical description and dosimetric data used in the "Linac Action". EURADOS Report 2020-05, ISSN 2226-8057. European Radiation Dosimetry Group e. V., Neuherberg, Germany. doi: 10.12768/9rvp-fq82.

De Carlan, L., Price, R., Chartier, J.-L., Kodeli, I., Siebert, B., Henninger, J., Posselt, J., Gualdrini, G., Agosteo, S., Bedogni, R., Bordy, J.-M., Cassette, P., Ferrari, P., Gomez Ros, J.-M., Großwendt, B., Lacoste, V., Pola, A., Rollet, S., Schultz, F., Simakov, S. P., Tanner, R., Terrissol, M., Zankl, M., 2008. Analysis of

computational problems expressing the overall uncertainties: photons, neutrons and electrons. Radiation Protection Dosimetry, 131, 15-23.

De Saint-Hubert, M., Farah, J., Klodowska, M., Romero-Expósito, M.T., Tyminska, K., Mares, V., Olko, P., Stolarczyk, L., Trinkl, S., 2022. The influence of nuclear models and Monte Carlo radiation transport codes on stray neutron dose estimations in proton therapy. Radiation Measurements, 150, 106693. doi: 10.1016/j.radmeas.2021.106693.

De Saint-Hubert, M., Tymińska, K., Stolarczyk, L., Brkić, H., 2021. Fetus dose calculation during proton therapy of pregnant phantoms using MCNPX and MCNP6.2 codes. Radiation Measurements, 149, 106665. doi: 10.1016/j.radmeas.2021.106665.

Eakins, J., Huet, C., Brkić, H., Capello, K., Desorgher, L., Epstein, L., Hunt, J.G., Kim, H.S., Krstic, D., Lee, Y.-K., Manohari, M., Nikezic, D., Shukrun, R.H., Souza-Santos, D., Tymińska, K., 2021. Monte Carlo calculation of organ and effective dose rates from ground contaminated by Am-241: Results of an international intercomparison exercise. Radiation Measurements, 148, 106649. doi: 10.1016/j.radmeas.2021.106649.

Gómez-Ros, J.M., Bedogni, R., Domingo, C., Eakins, J.S., Roberts, N., Tanner, R.J., 2018. International comparison exercise on neutron spectra unfolding in bonner spheres spectrometry: problem description and preliminary analysis. Radiation Protection Dosimetry, 180, 70–74. doi: 10.1093/rpd/ncy002.

Gómez-Ros, J.M., Bedogni, R., Domingo, C., Eakins, J.S., Roberts, N., Tanner, R.J., 2022. Results of the EURADOS international comparison exercise on neutron spectra unfolding in Bonner spheres spectrometry. Radiation Measurements, 153, 106755. doi: 10.1016/j.radmeas.2022.106755

Gómez-Ros, J.M., Moraleda, M., Arce, P., Bui, D.-K., Dang, T.-M.-L., Desorgher, L., Kim, H.S., Krstic, D., Kuć, M., Le, N.-T., Lee, Y.-K., Nguyen, N.-Q., Nikezic, D., Tymińska, K., Vrba, T., 2021. Monte Carlo calculation of the organ equivalent dose and effective dose due to immersion in a ^{16}N beta source in air using the ICRP reference phantoms. Radiation Measurements, 145, 106612. doi: 10.1016/j.radmeas.2021.106612.

Grosswendt, B., 1990. Dependence of the photon backscatter factor for water on source-to-phantom distance and irradiation field size. Physics in Medicine and Biology, 35, 1233.

Gualdrini, G., Agosteo, S., Ménard, S., Price, R.A., Chartier, J.-L., Großwendt, B., Kodeli, I., Leuthold, G.P., Siebert, B.R.L., Tagziria, H., Tanner, R.J., Terrissol, M., Zankl, M., 2005. QUADOS intercomparison: a summary of photon and charged particle problems. Radiation Protection Dosimetry, 115, 587–599. doi: 10.1093/rpd/nci197.

Gualdrini, G., Ferrari, P., 2004. Intercomparison on the Usage of Computational Codes in Radiation Dosimetry: Bologna, Italy International Workshop Proceedings, July 14-16, 2003, ENEA.

Gualdrini, G., Tanner, R.J., Agosteo, S., Pola, A., Bedogni, R., Ferrari, P., Lacoste, V., Bordy, J.-M., Chartier, J.-L., de Carlan, L., Gomez Ros, J.-M., Großwendt, B., Kodeli, I., Price, R.A., Rollet, S., Schultz, F., Siebert, B., Terrissol, M., Zankl, M., 2008. Analysis of the CONRAD computational problems expressing only stochastic uncertainties: neutrons and protons. Radiation Protection Dosimetry, 131, 7–14. doi: 10.1093/rpd/ncn241.

Harrison, R.M., Ainsbury, E., Alves, J., Bottollier-Depois, J.-F., Breustedt, B., Caresana, M., Clairand, I., Fantuzzi, E., Fattibene, P., Gilvin, P., Hupe, O., Knežević, Ž., Lopez, M.A., Olko, P., Olšovcová, V., Rabus, H., Rühm, W., Silari, M., Stolarczyk, L., Tanner, R., Vanhavere, F., Vargas, A., Woda, C., 2021. Eurados

Strategic Research Agenda 2020: Vision for the Dosimetry of Ionising Radiation. Radiation Protection Dosimetry, 194, 42–56. doi: 10.1093/rpd/ncab063.

Hertel, N. E., Davidson, J. W., 1985. The response of Bonner spheres to neutrons from thermal energies to 17.3 MeV. Nuclear Instruments and Methods in Physics Research Section A: Accelerators, Spectrometers, Detectors and Associated Equipment, 238, 509-516.

Huet, C., Eakins, J., Zankl, M., Gómez-Ros, J.M., Jansen, J., Moraleda, M., Struelens, L., Akar, D.K., Borbinha, J., Brkić, H., Bui, D.K., Capello, K., Linh Dang, T.M., Desorgher, L., Di Maria, S., Epstein, L., Faj, D., Fantinova, K., Ferrari, P., Gossio, S., Hunt, J., Jovanovic, Z., Kim, H.S., Krstic, D., Le, N.T., Lee, Y.-K., Murugan, M., Nadar, M.Y., Nguyen, N.-Q., Nikezic, D., Patni, H.K., Santos, D.S., Tremblay, M., Trivino, S., Tymińska, K., 2022. Monte Carlo calculation of organ and effective doses due to photon and neutron point sources and typical X-ray examinations: Results of an international intercomparison exercise. Radiation Measurements, 150, 106695. doi: 10.1016/j.radmeas.2021.106695

ICRP, 1991. 1990 Recommendations of the International Commission on Radiological Protection. ICRP Publication 60. Annals of the ICRP, 21.

ICRP, 1996. Conversion coefficients for use in radiological protection against external radiation. ICRP Publication 74. Annals of the ICRP, 26.

ICRP, 2009. ICRP Publication 110: Adult Reference Computational Phantoms. Annals of the ICRP 39, 1-164. doi: 10.1016/j.icrp.2009.09.001.

ICRP, 2010. ICRP Publication 116. Conversion coefficients for radiological protection quantities for external radiation exposures. Annals of the ICRP 40, 1-257. doi: 10.1016/j.icrp.2011.10.001

ICRU, 1980. Radiation Quantities and Units. ICRU Report 33.

ICRU, 1985. Determination of Dose Equivalents Resulting from External Radiation Sources. ICRU Report 39. Bethesda, Maryland: ICRU.

ICRU, 1987. Quantities and Units in Radiation Protection Dosimetry, ICRU Report 51.

ICRU, 1993. Stopping powers and ranges for protons and alpha particles, Bethesda, USA, International Commission on Radiation Units and Measurements.

ICRU, 1998. Conversion Coefficients for use in Radiological Protection Against External Radiations. ICRU Report 57. Bethesda, Maryland: ICRU.

ISO, 2017. General requirements for the competence of testing and calibration laboratories. Brussels: CEN-CENELEC.

Li, W.B., Belchior, A., Beuve, M., Chen, Y.Z., Maria, S.D., Friedland, W., Gervais, B., Heide, B., Hocine, N., Ipatov, A., Klapproth, A.P., Li, C.Y., Li, J.L., Multhoff, G., Poignant, F., Qiu, R., Rabus, H., Rudek, B., Schuemann, J., Stangl, S., Testa, E., Villagrasa, C., Xie, W.Z., Zhang, Y.B., 2020a. Intercomparison of dose enhancement ratio and secondary electron spectra for gold nanoparticles irradiated by X-rays calculated using multiple Monte Carlo simulation codes. Physica Medica 69, 147–163. doi: 10.1016/j.ejmp.2019.12.011.

Li, W.B., Beuve, M., Maria, S.D., Friedland, W., Heide, B., Klapproth, A.P., Li, C.Y., Poignant, F., Rabus, H., Rudek, B., Schuemann, J., Villagrasa, C., 2020b. Corrigendum to "Intercomparison of dose enhancement ratio and secondary electron spectra for gold nanoparticles irradiated by X-rays calculated using multiple Monte Carlo simulation codes" [Phys. Medica 69 (2020) 147-163]. Physica Medica 80, 383–388. doi: 10.1016/j.ejmp.2020.10.008.

Lindborg, L., Bartlett, D. T., Drake, P., Klein, H., Schmitz, T., Tichy, M., 1995. Determination of Neutron and Photon Dose Equivalent at Workplaces in Nuclear Facilities in Sweden (A joint SSI-EURADOS Comparison Exercise). Radiation Protection Dosimetry, 61, 89-100.

Lopez, M. A., Nogueira, P., Vrba, T., Tanner, R. J., Ruhm, W., Tolmachev, S. Y., 2019. Measurements and Monte Carlo Simulations of 241Am Activities in Three Skull Phantoms: EURADOS-USTUR Collaboration. Health Phys, 117, 193-201.

Nogueira, P., Rühm, W., Lopez, M. A., Vrba, T., Buchholz, W., Fojtík, P., Etherington, G., Broggio, D., Huikari, J., Marzocchi, O., Lynch, T., Lebacq, A. L., Li, C., Ośko, J., Malátova, I., Franck, D., Breustedt, B., Leone, D., Scott, J., Shutt, A., Hauck, B., Capello, K., Pérez-López, B., Navarro-Amaro, J. F., Pliszczyński, T., Fantínová, K., Tolmachev, S. Y., 2015. EURADOS 241Am skull measurement intercomparison. Radiation Measurements, 82, 64-73.

Petrovic, B., Roed, H., Martín, R., Romero, A. M., Askounis, P., Buchanan, L., Rossi, F., Bernat, R., Alves, J. G., 2020. ISO/IEC 17025 Guidance for IMS: Suggestions on How to Interpret and Implement the Requirements Including Examples from Accredited Laboratories.

Piesch, E., Burgkhardt, B., 1988. Albedo dosimetry system for routine personnel monitoring. Radiation Protection Dosimetry, 23, 117-120.

Price, R.A., Gualdrini, G., Agosteo, S., Ménard, S., Chartier, J.-L., Großwendt, B., Kodeli, I., Leuthold, G.P., Siebert, B.R.L., Tagziria, H., Tanner, R.J., Terrissol, M., Zankl, M., 2006. Pitfalls and modelling inconsistencies in computational radiation dosimetry: lessons learnt from the QUADOS intercomparison. Part II: Photons, electrons and protons. Radiation Protection Dosimetry, 118, 155–166. doi: 10.1093/rpd/ncl014.

Rabus, H., Gómez-Ros, J.M., Villagrasa, C., Eakins, J., Vrba, T., Blideanu, V., Zankl, M., Tanner, R., Struelens, L., Brkić, H., Domingo, C., Baiocco, G., Caccia, B., Huet, C., Ferrari, P., 2021a. Quality assurance for the use of computational methods in dosimetry: activities of EURADOS Working Group 6 `Computational Dosimetry'. J. Radiol. Prot. 41, 46-58. doi: 10.1088/1361-6498/abd914.

Rabus, H., Li, W.B., Nettelbeck, H., Schuemann, J., Villagrasa, C., Beuve, M., Di Maria, S., Heide, B., Klapproth, A.P., Poignant, F., Qiu, R., Rudek, B., 2021b. Consistency checks of results from a Monte Carlo code intercomparison for emitted electron spectra and energy deposition around a single gold nanoparticle irradiated by X-rays. Radiation Measurements, 147, 106637. doi: 10.1016/j.radmeas.2021.106637.

Rabus, H., Li, W.B., Villagrasa, C., Schuemann, J., Hepperle, P.A., Rosales, L. de la F., Beuve, M., Maria, S.D., Klapproth, A.P., Li, C.Y., Poignant, F., Rudek, B., Nettelbeck, H., 2021c. Intercomparison of Monte Carlo calculated dose enhancement ratios for gold nanoparticles irradiated by X-rays: Assessing the uncertainty and correct methodology for extended beams. Physica Medica 84, 241–253. doi: 10.1016/j.ejmp.2021.03.005.

Rabus, H., Zankl, M., Gómez-Ros, J.M., Villagrasa, C., Eakins, J., Huet, C., Brkić, H., Tanner, R., 2022. Lessons learnt from the recent EURADOS intercomparisons in computational dosimetry. Radiation Measurements, 156, 106822. doi: 10.1016/j.radmeas.2022.106822

Rollet, S., Agosteo, S., Fehrenbacher, G., Hranitzky, C., Radon, T., Wind, M., 2009. Intercomparison of radiation protection devices in a high-energy stray neutron field, Part I: Monte Carlo simulations. Radiation Measurements, 44, 649-659.

Rühm, W., Ainsbury, E., Breustedt, B., Caresana, M., Gilvin, P., Knežević, Ž., Rabus, H., Stolarczyk, L., Vargas, A., Bottollier-Depois, J.F., Harrison, R., Lopez, M.A., Stadtmann, H., Tanner, R., Vanhavere, F., Woda, C., Clairand, I., Fantuzzi, E., Fattibene, P., Hupe, O., Olko, P., Olšovcová, V., Schuhmacher, H., Alves, J.G., Miljanic, S., 2020. The European radiation dosimetry group – Review of recent scientific achievements. Radiation Physics and Chemistry168, 108514. doi: j.radphyschem.2019.108514.

Rühm, W., Fantuzzi, E., Harrison, R., Schuhmacher, H., Vanhavere, F., Alves, J., Bottollier Depois, J. F., Fattibene, P., Knezevic, Z., Lopez, M. A., Mayer, S., Miljanic, S., Neumaier, S., Olko, P., Stadtmann, H., Tanner, R., Woda, C., 2016. EURADOS strategic research agenda: vision for dosimetry of ionising radiation. Radiation Protection Dosimetry*,* 168**,** 223-34.

Rühm, W., Bottollier-Depois, J.F., Gilvin, P., Harrison, R., Knežević, Ž., Lopez, M.A., Tanner, R., Vargas, A., Woda, C., 2018. The work programme of EURADOS on internal and external dosimetry. Annals of the ICRP 47, 20–34. doi: 10.1177/0146645318756224.

Shrimpton, P. C., Wall, B. F., Jones, D. G., Fisher, E. S., Hillier, M. C., Kendall, G. M., Harrison, R. M., 1986. Doses to patients from routine diagnostic X-ray examinations in England. The British Journal of Radiology, 59, 749-758.

Siebert, B. R. L., Schuhmacher, H., 1994. Calculated Fluence-to-Directional and Personal Dose Equivalent Conversion Coefficients for Neutrons. Radiation Protection Dosimetry, 54, 231-238.

Siebert, B., Schuhmacher, H., 1995. Quality factors, ambient and personal dose equivalent for neutrons, based on the new ICRU stopping power data for protons and alpha particles. Radiation Protection Dosimetry, 58, 177-183.

Siebert, B.R.L., Tanner, R.J., Chartier, J.-L., Agosteo, S., Großwendt, B., Gualdrini, G., Ménard, S., Kodeli, I., Leuthold, G.P., Price, R.A., Tagziria, H., Terrissol, M., Zankl, M., 2006. Pitfalls and modelling inconsistencies in computational radiation dosimetry: lessons learnt from the QUADOS intercomparison. Part I: Neutrons and uncertainties. Radiation Protection Dosimetry, 118, 144–154. doi: 10.1093/rpd/ncl013.

Silari, M., Agosteo, S., Beck, P., Bedogni, R., Cale, E., Caresana, M., Domingo, C., Donadille, L., Dubourg, N., Esposito, A., 2009. Intercomparison of radiation protection devices in a high-energy stray neutron field. Part III: Instrument response. Radiation Measurements, 44, 673-691.

Snyder, W., Ford, M., Warner, G., Fisher, H., Pamphlet, M., 1969. Revised Estimates of Absorbed Fractions for Monoenergetic Photon Sources Uniformly Distributed in Various Organs of a Heterogeneous Phantom. J. Nucl. Med, 10, 7-52.

Tanner, R.J., Chartier, J.-L., Siebert, B.R.L., Agosteo, S., Großwendt, B., Gualdrini, G., Kodeli, I., Leuthold, G.P., Ménard, S., Price, R.A., Tagziria, H., Terrissol, M., Zankl, M., 2004. Intercomparison on the usage of computational codes in radiation dosimetry. Radiation Protection Dosimetry, 110, 769–780. doi: 10.1093/rpd/nch228.

Villagrasa, C., Bordage, M.-C., Bueno, M., Bug, M., Chiriotti, S., Gargioni, E., Heide, B., Nettelbeck, H., Parisi, A., Rabus, H., 2019. Assessing the contribution of cross-sections to the uncertainty of Monte Carlo calculations in micro- and nanodosimetry. Radiation Protection Dosimetry, 183, 11–16. doi: 10.1093/rpd/ncy240.

Villagrasa, C., Rabus, H., Baiocco, G., Perrot, Y., Parisi, A., Struelens, L., Qiu, R., Beuve, M., Poignant, F., Pietrzak, M., Nettelbeck, H., 2022. Intercomparison of micro- and nanodosimetry Monte Carlo simulations: An approach to assess the influence of different cross-sections for low-energy electrons

on the dispersion of results. Radiation Measurements, 150, 106675. doi: 10.1016/j.radmeas.2021.106675.

Vrba, T., Nogueira, P., Broggio, D., Caldeira, M., Capello, K., Fantínová, K., Figueira, C., Hunt, J., Leone, D., Murugan, M., Marzocchi, O., Moraleda, M., Shutt, A., Suh, S., Takahashi, M., Tymińska, K., Lopez, M.A., Tanner, R., 2014. EURADOS intercomparison exercise on MC modeling for the in-vivo monitoring of Am-241 in skull phantoms (Part I). Radiation Physics and Chemistry, 104, 332–338. doi: 10.1016/j.radphyschem.2013.12.010.

Vrba, T., Broggio, D., Caldeira, M., Capello, K., Fantínová, K., Franck, D., Gómez-Ros, J.M., Hunt, J., Kinase, S., Leone, D., Lombardo, P.A., Manohari, M., Marzocchi, O., Moraleda, M., Nogueira, P., Ośko, J., Arron, S., Suhl, S., Takahashi, M., Teles, P., Tremblay, M., Tymińska, K., Lopez, M.A., Tanner, R., 2015. EURADOS intercomparison exercise on MC modelling for the in-vivo monitoring of AM-241 in skull phantoms (Part II and III). Radiation Physics and Chemistry, 113, 59–71. doi: 10.1016/j.radphyschem.2015.04.009.

Wiegel, B., Agosteo, S., Bedogni, R., Caresana, M., Esposito, A., Fehrenbacher, G., Ferrarini, M., Hohmann, E., Hranitzky, C., Kasper, A., Khurana, S., Mares, V., Reginatto, M., Rollet, S., Rühm, W., Schardt, D., Silari, M., Simmer, G., Weitzenegger, E., 2009. Intercomparison of radiation protection devices in a high-energy stray neutron field, Part II: Bonner sphere spectrometry. Radiation Measurements, 44, 660-672.

Wilkinson, M.D., Dumontier, M., Aalbersberg, Ij.J., Appleton, G., Axton, M., Baak, A., Blomberg, N., Boiten, J.-W., da Silva Santos, L.B., Bourne, P.E., Bouwman, J., Brookes, A.J., Clark, T., Crosas, M., Dillo, I., Dumon, O., Edmunds, S., Evelo, C.T., Finkers, R., Gonzalez-Beltran, A., Gray, A.J.G., Groth, P., Goble, C., Grethe, J.S., Heringa, J., 't Hoen, P.A.C., Hooft, R., Kuhn, T., Kok, R., Kok, J., Lusher, S.J., Martone, M.E., Mons, A., Packer, A.L., Persson, B., Rocca-Serra, P., Roos, M., van Schaik, R., Sansone, S.-A., Schultes, E., Sengstag, T., Slater, T., Strawn, G., Swertz, M.A., Thompson, M., van der Lei, J., van Mulligen, E., Velterop, J., Waagmeester, A., Wittenburg, P., Wolstencroft, K., Zhao, J., Mons, B., 2016. The FAIR Guiding Principles for scientific data management and stewardship. Sci. Data 3, 160018. doi: 10.1038/sdata.2016.18.

Zankl, M., Eakins, J., Gómez Ros, J.-M., Huet, C., 2021a. The ICRP recommended methods of red bone marrow dosimetry. Radiation Measurements, 146, 106611. doi: 10.1016/j.radmeas.2021.106611.

Zankl, M., Eakins, J., Gómez Ros, J.-M., Huet, C., Jansen, J., Moraleda, M., Reichelt, U., Struelens, L., Vrba, T., 2021b. EURADOS intercomparison on the usage of the ICRP/ICRU adult reference computational phantoms. Radiation Measurements, 145, 106596. doi: 10.1016/j.radmeas.2021.106596.

Zankl, M., Gómez Ros, J.-M., Moraleda, M., Reichelt, U., Akar, D.K., Borbinha, J., Desorgher, L., Di Maria, S., EL Bakkali, J., Fantinova, K., Ferrari, P., Gossio, S., Hunt, J., Jovanovic, Z., Kim, H.S., Krstic, D., Lee, Y.-K., Nadar, M.Y., Nikezic, D., Patni, H.K., Murugan, M., Triviño, S., 2021c. Monte Carlo calculation of organ dose coefficients for internal dosimetry: Results of an international intercomparison exercise. Radiation Measurements, 148, 106661. doi: 10.1016/j.radmeas.2021.106661.

Zankl, M., Veit, R., Williams, G., Schneider, K., Fendel, H., Petoussi, N., Drexler, G., 1988. The construction of computer tomographic phantoms and their application in radiology and radiation protection. Radiation and environmental biophysics, 27, 153-164.

7. OpenDose3D, a clinical dosimetry software for nuclear medicine

Manuel Bardiès[1,2], [1]Institut de Recherches en Cancérologie de Montpellier, UMR 1194, INSERM Université de Montpellier, F-34298, Montpellier, France, [2]Institut Régional du Cancer de Montpellier, Montpellier, F-34298, France

Abstract

OpenDose3D is open source, freely available software designed for image-based, patient specific clinical dosimetry in nuclear medicine. It is based on 3D Slicer, and therefore benefits from already developed features such as DICOM import, image visualisation and processing, registration, and segmentation. The modular nature of the clinical dosimetry workflow allowed developing additional features required for the purpose, such as absorbed dose calculation or time dependent variable fitting and integration. Additional modules were developed to allow considering the calibration process, which is an essential part of the clinical dosimetry procedure. The validation of the software is still ongoing, and a first official release is planned at the end of summer 2024.

7.1. Introduction

Therapeutic nuclear medicine applications use either radiopharmaceuticals (radiopharmaceutical therapy or RPT) or radioactive medical devices (selective internal radiotherapy or SIRT) to treat (most often) cancer targets. The generic term molecular radiotherapy (MRT) will be used here to group all therapeutic nuclear medicine applications.

MRT aims at delivering specific irradiation to target volumes while sparing organs at risk (OAR). As for any radiotherapy, EURATOM Directive 2013/59 states that "exposures of target volumes shall be individually planned, and their delivery appropriately verified" (Council of the European Union, 2014). To fulfil that requirement, clinical dosimetry tools are increasingly available, with the recent advent of commercial software with CE marking that can be used in clinical routine. This raises the question of their benchmarking.

Comparison of available software shows that these tools are far from being standardised (Mora-Ramirez et al., 2020). Many of them cover only some specific parts of the clinical dosimetry workflow (CDW). In addition, the algorithms implemented in these codes and the order with which they are executed in sequence vary from one software to the next (Della Gala et al., 2021). For example, registration can be rigid or elastic, segmentation manual or (more or less) automatic, absorbed dose can be computed using several algorithms etc. In addition, the way temporal variables are dealt with (time-dependant variable fitting and integration) can also vary. Activity (MBq or equivalent) can be assessed at each time point, the time activity curve fitted, and time integrated activity computed (in MBq.s or equivalent) before the absorbed dose calculation step. Alternatively, absorbed dose rates (Gy s^{-1} or equivalent) can be computed at each time point, before fitting and integrating in time.

In addition to the different ways to integrate the steps of the CDW, a review of existing software (Mora-Ramirez et al., 2020) allowed the identification of "must" or "nice to have" features that increase the traceability of clinical dosimetry:

- Storing intermediary results not only allows stopping and resuming a clinical dosimetry study, but also allows the possibility of exporting/importing intermediary files, for external

processing or evaluation. These *checkpoints* may help in identifying the most variable steps of the CDW. DICOM RT input/output of structures such as volumes of interest or absorbed dose(rate) maps is essential. Giving access to input data (emission data from each radioisotope, voxel S values, etc.) is also important.

- Establishing internal *sanity checks* is also a tremendous help in identifying potential errors. Interrupting the process when abnormal settings are identified, or aberrant results are computed should be generalised. For example. in case of variable acquisition settings (duration), or when spectrometry, image format, gamma camera collimation vary between patient acquisitions, or if a calculated effective half-life is greater than the physical half-life. As can be seen, this may trigger anything from simple warning messages to fatal errors.

All these features ("must-have" and "nice to have") helped in defining OpenDose3D specifications.

7.2. Materials and Methods

OpenDose3D (OD3D) is based on 3D Slicer (Fedorov 2012). More precisely, OD3D is an official extension of 3D Slicer, meaning it can be downloaded directly from inside 3D Slicer using the *Extensions manager* module.

3D Slicer is a *software application* for medical image visualization and analysis, a research *software platform* which allows researchers to quickly develop and evaluate new methods and distribute them to clinical users and a *product development platform*, which allows companies to quickly prototype and release products to users. 3D Slicer is completely free and distributed under a BSD-style open source.

When it comes to nuclear medicine dosimetry, 3D Slicer already includes features that make it an excellent choice to build a dosimetry module:

- DICOM (RT) import/export
- Multimodality visualisation
- Registration tools
- Segmentation tools

Also, although not directly within the scope of OD3D, 3D Slicer extensions designed for nuclear medicine (PET or SPECT) already exist.

Therefore, from already existing modules/features of 3D Slicer to OD3D, it was "just" needed to develop missing features, namely:

- The workflow, i.e., the way the different modules are arranged in sequence.
- The fitting and integration of time-dependent variables (activity or absorbed dose rates)
- The calculation of energy deposited in target volumes using a range of radiation transport and energy deposition algorithms

Then, along the development and test process, additional features were integrated: *Checkpoints* and *Sanity checks*. In addition, a *Calibration module* was eventually designed as a companion to OD3D.

7.3. Results

The development was carried out mostly by Alex Vergara Gil during his PhD (Vergara Gil, 2022), even though some parts of OD3D were developed by him earlier (Milano et al., 2021) as part of a different research project. Most of the development process was supported by the MEDIRAD project (www.medirad-project.eu), even though several additional collaborators contributed to the

development within the frame of the OpenDose collaboration (Chauvin et al., 2020). Currently the development is mostly performed by Jose Alejandro Fragoso Negrin within the frame of his PhD.

At the moment, OD3D is in a pre-release stage (Vergara Gil et al., 2020), as it's already a fully functional application but some developments are still ongoing. We are presenting here the most used features. Some of the figures are extracted from the future (not yet released) version 1 of the software.

The first step is to select patient images that compose the clinical dosimetry study. These are usually a sequence of SPECT/CT images acquired at different times. These can be loaded using the *Add DICOM Data* 3D Slicer module. Then the OD3D module is selected.

As can be seen in Fig. 7.1, the first panel on the home screen of OPenDose3D contains data that are either automatically read or manually entered. The selection of the workflow is made at that level, with (in the current state of development) 2 choices: *Activity* or *Absorbed Dose Rate* workflows. This determines the sequence of operations performed to go from count-indexed images to absorbed doses in user-defined VOIs. This is illustrated in Fig. 7.2 (from Della Gala et al. (2021)).

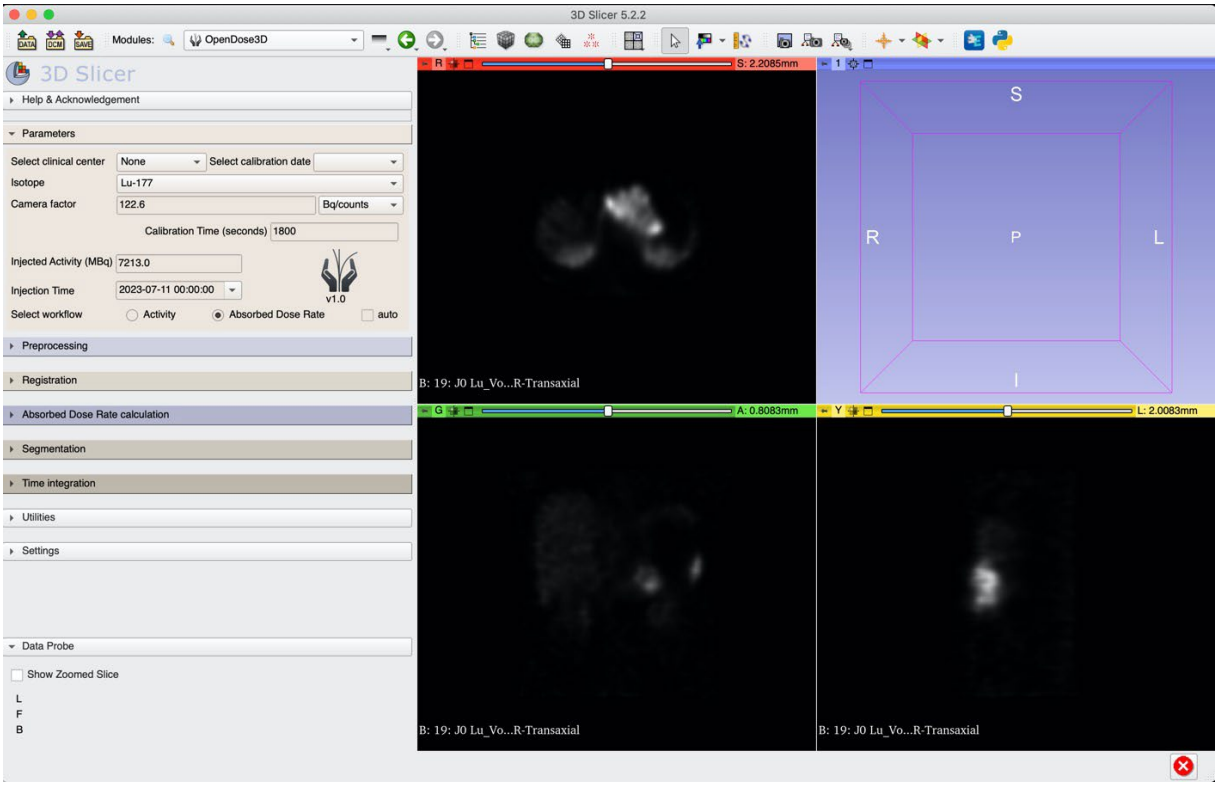

Fig. 7.1: Main panel of OpenDose3D. The different step modules are activated in sequence.

All workflows start from time-indexed patient images. Then, in the activity workflow, the time integrated activity is calculated before the absorbed dose calculation part, whereas in the absorbed dose rate (ADR) workflow, absorbed dose rates are computed first, and then integrated in time. Both workflows ended with the calculation of the absorbed dose, however the sequence of operations in OD3D varies depending on the workflow selected.

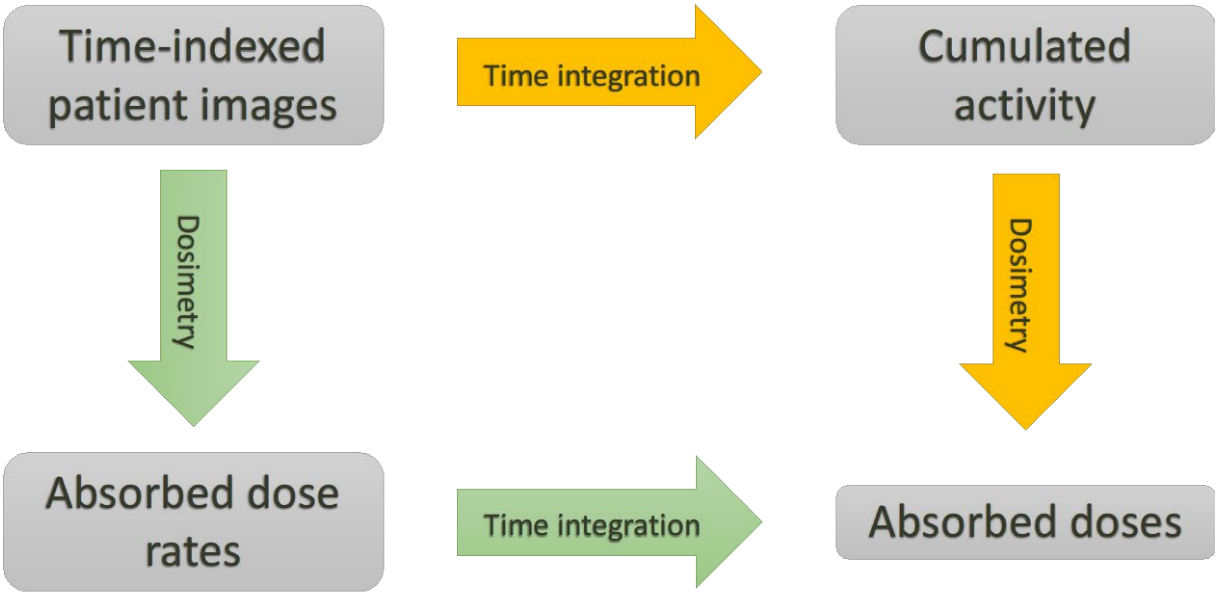

Fig. 7.2: Illustration of the 2 main workflows of OD3D: Activity and Absorbed dose rate workflows (From Della Gala et al. (2021)).

Pre-processing is made first. The first step is to create a specific file architecture for each study: image copies are renamed and added to time-indexed folders. Then CT images are resampled to the scale of the SPECT, and both SPECT and CT mages are rescaled to activity-indexed images and attenuation maps. New image datasets are created and stored at each step of the processing.

Registration is performed on a selected reference CT frame. Both rigid and elastic registrations are possible as they are both present as 3D Slicer modules. It is possible to check and validate registered images.

Regardless of the workflow selected, *absorbed dose rate* is computed at the voxel level on each image (at each time point). Three possibilities are offered to the user, corresponding to the broad algorithms (Bardiès and Vergara Gil, 2022) implemented for nuclear medicine dosimetry:

- Local energy deposition is only considering the beta/electronic radiation, assumed to be non-penetrating even at the voxel level. This is by far the fastest option, but it's relevance must be assessed for each study: it is usually adapted to ^{177}Lu emissions, but less so for ^{90}Y (electron range can be greater than voxel size) or ^{131}I (gamma component be neglected). A density correction when selected, is performed at the voxel level.
- Convolution is the second absorbed dose (rate) calculation algorithm. Voxel S Values (VSV) (Lanconelli et al., 2012) are computed in a specific module from absorbed dose point kernels. They can also be integrated from external sources if necessary. Even though initial development considered the possibility of performing convolution in heterogeneous media (Vergara Gil, Mora Ramirez et al., 2019), OD3D currently performs convolution in homogeneous media, but allows for density correction at the voxel level.
- Monte Carlo modelling of radiation transport and energy deposition is also possible in OD3D (Vergara Gil, Chauvin et al., 2019). If the user selects that option, an input file for the Monte Carlo code GATE is generated. This obviously requires access to GATE to perform the actual simulation, and at the end the output from GATE is read in OD3D to generate absorbed dose rate maps.

Segmentation is the next step. This is performed using 3D Slicer existing modules. This allows for manual, semi-automatic and more recently fully automatic, CT-based segmentation based on artificial intelligence thanks to the TotalSegmentator module (Wasserthal et al., 2022). Obviously, tumour segmentation may require definition on functional (SPECT) images. Yet, at the end of that stage, volumes of interest are defined, containing activity, or absorbed dose rates, depending on the selected workflow.

The time-integration step considers every VOI at each time point and allows the selection of a range of possible fit functions (mono- multi-exponential, trapeze). Extrapolation from zero to the first time point is also chosen by the user (forcing the origin of the curve to zero, or to the value of the first time point, or using the back-extrapolation of the fit to zero). This is equally valid for activity or absorbed dose rates (Fig. 7.3). At the end of time-integration step, absorbed doses are provided in tables. Intermediary results are also provided or stored in images.

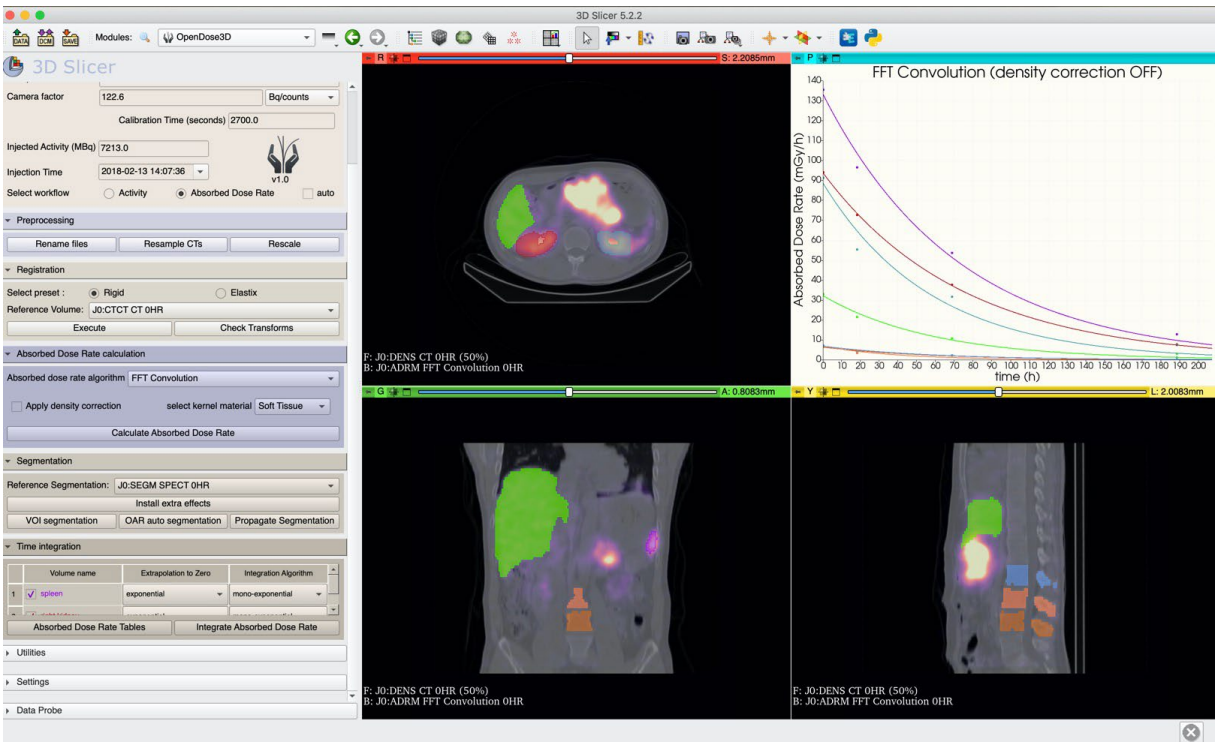

Fig. 7.3: Presentation of the results of the absorbed dose rate workflow: the absorbed dose rate curves are presented in the top right quadrant. They are later integrated to yield absorbed doses.

Then, along the development and test process, additional features were integrated:

- Checkpoints
  During OD3D processing, intermediary data are generated and stored automatically. They can be exported and processed to compare with other codes or verify consistency of the results.
- Sanity checks are also generated, depending on how well the DICOM headers are filled. The fact is that many DICOM fileds exist but left empty as they are usually not further used. Also, the anonymisation process, when required, tends to erase useful fields, and may prevent clinical dosimetry software operations.

- The Calibration module
  An important observation made during the comparison of commercial software is that the format of the calibration factor used to convert count-indexed images to activity-indexed images was highly variable. In addition, the calibration factor is manually entered by the operator, even when no real guidance is provided on how to generate it. This is an important source of error, due to incorrect transcription of a correct calibration factor, or issues related to the units. Basically, some software requires the sensitivity factor to be given in counts/MBq, or CPS/MBq, or Bq/counts, etc. Of note is that fact that a calibration factor in counts/MBq prevents the use of variable acquisition times, even when low image statistics would require longer acquisitions at the end of the pharmacokinetics.

The OD3D calibration module gives the user the possibility of selecting (and storing) calibration images. These are by default homogenous distributions of radioactivity in large water phantoms. Then, designing volumes of interest can be done on the whole field of view, or based on the CT-derived internal volume of the phantom, or a smaller volume inside the phantom to avoid edge effects. Sensitivity factors are then computed and stored for a given camera in a given facility. Calibration values and their units are then passed to the OD3D module, thereby decreasing the chances of transcription errors.

The idea is that, since camera calibrations can be used for several patients (until a new calibration factor is acquired, for whatever reason), an alias of the calibration images and results are included in each patient folder, in order to increase traceability.

At the moment, the calibration module only transfers the sensitivity factor (counts/Bq or equivalent) to OD3D, but work is in progress to integrate contrast recovery calibrations in the module.

7.4. Discussion

Clinical dosimetry can be performed using two approaches. Historically, model-based (reference) dosimetry has been used for diagnostic radiopharmaceuticals, to document the (low) absorbed doses delivered in diagnostics. Image-based, patient-specific dosimetry is more adapted to molecular radiotherapy. OD3D has been designed to address that second type of approach.

As was seen, different clinical dosimetry workflows are possible.

The *Activity* workflow is more adapted to reference dosimetry. It also follows the historical MIRD formalism where the cumulated activity (time-integrated activity) is computed first, before being multiplied by the relevant precomputed S value.

The *Absorbed dose rate* workflow seems a priori more adapted to image-based dosimetry, where absorbed dose rates are calculated specifically at each time point.

The 2 workflows are only apparently symmetrical. In fact, depending on which absorbed dose (rate) calculation algorithm is used, the results may not be identical. Furthermore, whereas the activity workflow requires keeping the same VOI in time, the ADR workflow can accommodate volume variations that may occur between time points. The comparison of the dosimetric consequences of selecting a given workflow is under study.

Regarding the validation of the software, several important steps have been performed and are reported by Vergara Gil (Vergara Gil et al., 2020):

- The generation of Dose Point Kernels (DPK) and their transformation in Voxel S Values was evaluated
- The benchmarking of Monte Carlo approach was also performed
- The comparison between OD3D and available clinical dosimetry code was done
- The internal comparison of the results obtained using the different absorbed dose calculation algorithms was finally made.

Several isotopes were considered (^{90}Y, ^{177}Lu, ^{131}I) in the validation, but DPK have been generated also for others. The reference chosen for nuclear data is the ICRP report 107 (ICRP, 2008) that considers 1252 radionuclides. It is beyond the scope of this report to present in detail the validation process, and this will be given in a separate publication. However, that stage of OD3D development triggered an interesting discussion regarding the requirements for clinical dosimetry benchmarking.

When dealing with such multiple steps processes, as is the case for clinical dosimetry, it is mandatory to verify/validate each step independently of the others, hence the requirement for a modular software architecture. Then, depending on the step, the benchmarking must be done using different tools: phantoms with known activity inserts are adapted to the validation of a calibration procedure. However, they are absolutely not adapted to the comparison of registration procedures. Models can be used to verify absorbed dose calculation algorithms, but they are sometimes overly simple when compared to real patient images. Patient datasets are a more realistic way to evaluate the end-to-end process. However, since the basics are not known, only precision can be assessed.

Finally, the accuracy required may differ from one clinical application to another. In that context, a fast, first order estimate of the delivered absorbed doses using local energy deposition may be preferable to lengthy Monte Carlo calculations. The two approaches may not be mutually exclusive: a rough estimate of delivered irradiation to OARs may be used as a fast "Go/No go" step for therapy continuation, while Monte Carlo modelling may still be implemented to further document the irradiation delivered. Obviously, each absorbed dose calculation algorithm should be carefully benchmarked to be as valid as reasonably possible.

The OpenDose3D project started as an attempt to develop clinical dosimetry software adapted to research, or to centres who do not have the possibility of purchasing expensive commercial software. The objectives have slightly shifted to consider now OD3D as software as the reference for benchmarking of other clinical dosimetry software.

Some implemented features are at the moment unique. The calibration module is one of these. The checkpoints are an essential part of the traceability. Sanity checks should be further developed. The possibility of implementing different CDW is interesting but requires further validation.

Work is in progress to integrate more robust curve fitting algorithms derived from those implemented in NukFit (Kletting et al., 2013). In addition, a collaboration with NPL has been initiated to integrate the calculation and propagation of uncertainties.

7.5. Conclusion

OpenDose3D was initially conceived as clinical dosimetry software for research. The idea was to develop software that could perform image-based dosimetry, implementing all steps of the clinical dosimetry workflow in a modular way that would allow generating as many checkpoints as deemed necessary.

With time, the objective deviated when we realized that OD3D was gradually becoming software to benchmark clinical dosimetry software, as its modularity allowed the assessment of the performances of academic or commercial software that would otherwise be difficult to compare. In other words, software A and B cannot be directly compared, but both can be compared to OD3D.

The opensource nature of OD3D allows the aggregation of several groups to develop the software collaboratively and add further features.

Finally, OD3D is a very interesting tool for clinical dosimetry education.

7.6. References

Bardiès, M., Vergara Gil, A., 2022. ABSORBED DOSE CALCULATION. In: International Atomic Energy Agency (IAEA), ed., Dosimetry for Radiopharmaceutical Therapy [IAEA Preprint]. Vienna (Austria), 154-175. http://inis.iaea.org/search/search.aspx?orig_q=RN:53037189.

Chauvin, M., Borys, D., Botta, F., Bzowski, P., Dabin, J., Denis-Bacelar, A.M. et al., 2020. OpenDose: Open-Access Resource for Nuclear Medicine Dosimetry. J Nucl Med., 61, 1514-1519.

Council of the European Union, 2014. European Council Directive 2013/59/Euratom on basic safety standards for protection against the dangers arising from exposure to ionising radiation and repealing Directives 89/618/Euratom, 90/641/Euratom, 96/29/Euratom, 97/43/Euratom and 2003/122/Euratom. Official Journal of the EU. 2014; L13:1–73.

Della Gala, G, Bardiès, M., Tipping, J., Strigari, L., 2021. Overview of commercial treatment planning systems for targeted radionuclide therapy. Physica Medica 92, 52-61.

ICRP, 2008. Nuclear Decay Data for Dosimetric Calculations. ICRP Publication 107. Annals of the ICRP 38 (3).

Kletting, P., Schimmel, S., Kestler, HA., Hänscheid, H., Luster, M., Fernández, M., Bröer, JH., Nosske, D., Lassmann, M., Glatting, G., 2013. Molecular radiotherapy: the NUKFIT software for calculating the time-integrated activity coefficient. Medical Physics 40, 102504. doi: 10.1118/1.4820367.

Lanconelli, N., Pacilio, M., Lo Meo, S., Botta, F., Di Dia, A., Torres Aroche, A., Coca Pérez, M. A., Cremonesi, M., 2012. A free database of radionuclide voxel S values for the dosimetry of nonuniform activity distributions. Phys Med Biol. 57(2), 517-533. doi:10.1088/ 0031- 9155/57/2/517.

Milano, A., Vergara Gil, A., Fabrizi, E., Cremonesi, M., Veronese, I., Gallo, S. et al., 2021. In Silico Validation of MCID Platform for Monte Carlo-Based Voxel Dosimetry Applied to ^{90}Y-Radioembolization of Liver Malignancies. Applied Sciences, 11, 1939.

Mora-Ramirez, E., Santoro, L., Cassol, E. et al., 2020. Comparison of commercial dosimetric software platforms in patients treated with ^{177}Lu-DOTATATE for peptide receptor radionuclide therapy. Medical Physics, 47, 4602-4615. doi: 10.1002/mp.14375

Vergara Gil, A., 2022. Implementation of a clinical dosimetry workflow to perform personalized dosimetry for internal radiotherapy: Université de Toulouse.

Vergara Gil, A., Amato, E., Auditore, L., Brenet, M., Chauvin, M., Clayton, N., Ferrer, L., Gibaud, B., Gnesin, S., Italiano, A., Kayal, G., Lima, T., Ocampo-Ramos, J., Pistone, D., Quang, G., Mora-Ramirez, E., Ruegger, J., Bardiès, M., 2020. OpenDose3D: A free, collaborative 3D Slicer module for patient-specific dosimetry. EJNMMI 47 (Suppl 1) S314-S315 (Meeting Abstract OP-622).

Vergara Gil, A., Chauvin, M., Kayal, G., Ocampo Ramos, J.C., Bardiès, M., 2019. Geant4/GATE ion source implementation for internal dosimetry applications. European Journal of Nuclear Medicine and Molecular Imaging, 46(Suppl 1), S365.

Vergara Gil, A., Mora Ramirez, E., Pouget, J., Kotzki, P., Santoro, L., Deshayes, E., Bardiès, M., 2019. Fast heterogeneous convolution algorithm used in absorbed dose calculation for beta emitters. European Journal of Nuclear Medicine and Molecular Imaging, 46(Suppl 1), S473-S474.

Wasserthal, J., Meyer, M., Breit H.C., Cyriac J., Shan Y., Segeroth, M., 2022. TotalSegmentator: robust segmentation of 104 anatomical structures in CT images. https://arxiv.org/abs/2208.05868

8. New developments in radiotherapy treatment planning with particle beams

Emanuele Scifoni, Trento Institute for Fundamental Physics and Applications (INFN-TIFPA), Italy

Abstract

Particle beams, with their different modalities for scanning, offer a specific series of advantages for radiotherapy treatment planning in terms of flexibility of the irradiation field, which can be optimized and adapted in several ways, for covering, e.g., with prescribed dose and LET, different areas according to specific tissue sensitivities.

Novel advances in the last decade focus on so-called biological treatment planning, i.e., a concept of maximizing the biological response of the irradiated tissue, rather than a purely dosimetric homogeneous coverage of the target, taking into account different radiobiological effects, related to LET, oxygenation, volume effects, dose rate etc.

An overview of such advances is reported in this contribution, including the novel direction of radiotherapy with ultra-high dose rates (FLASH) and the specifically related planning approaches.

8.1. Introduction

Particle beams have convenient ballistic features allowing better physical dose conformity and, in general, a higher biological effectiveness at the same delivered dose. Besides these well-known physical and radiobiological advantages, specific scanning modalities, such as pencil beam scanning, allow very accurate dose conformation and links to optimization routines in order to get straightforwardly the best possible coverage of the irradiated target, by exploiting the full number of degrees of freedom available (Durante and Flanz, 2019).

In fact, as can be seen in Fig. 8.1, magnetic scanning in the lateral direction together with energy switching in the depth coordinate allows the particle beams to be shaped, modulating their individual number in each spot (called raster spot) according to any optimization task. This allows the realization of an arbitrary distribution not only of the physical dose, but also of the radiation quality (Kraemer et al., 2000), in each voxel of the irradiated target, including normal tissue and organs at risk (OAR). Moreover, the use of multiple fields of particles coming from different defined angles allows an additional flexibility, e.g., in the sparing of OARs and in obtaining different distributions for a same physical dose. This is the so-called multiple field optimization (Gemmel et al., 2008). Thus, it simply becomes a question of defining the optimization task to prescribe a given effect on the target and then the planning routine can be enabled to realize the desired distribution of the voxels in terms of the chosen quantity, by browsing the multidimensional hypersurface of degrees of freedom and fixing the number of particles in each spot for each field.

This has opened the way for consideration of the biological effects on the target as a function of the raster spots, the so-called biological treatment planning (Gemmel et al., 2008).

A pioneer in these developments has been the TRiP98 code (Kraemer et al., 2000, Kraemer and Scholz 2000), which enabled the first treatment planning for particles other than protons, including ions with higher charge. This code was steadily expanded as a research tool, taking account of several features.

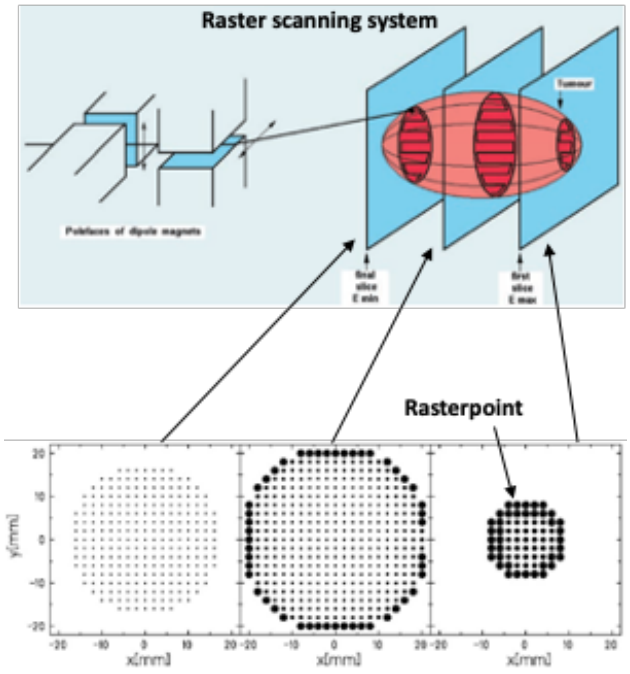

Fig. 8.1: Illustration of the raster points, i.e., the individual spots of irradiation, where an arbitrary number of particles can be delivered (quantified by the spot areas in the lower panel) thus defining the degrees of freedom for optimization with a fully active scanning particle beam. Modified from Kraemer et al., 2000.

Several other codes have included and explored these possibilities. Among them it is worth mentioning the analytical codes MatRad (Wieser et al., 2017), FROG (Choi et al., 2018) and RPLANIT (Manganaro et al., 2017) and FRED (Gajewski et al., 2021), FLUKA (Mairani et al., 2010) and TOPAS (Polster et al., 2015), the latter three Monte Carlo based. Some of these codes, e.g., FROG and FRED, benefit from higher computation speeds due to the GPU based computation. Also, some commercial TPSs, such as Raystation (*add manufacturer, location*), which has been recently released also with a Monte Carlo based engine, have included biological treatment planning features for several years (Rana et al., 2019).

Mathematically, a generic optimization task for delivering a prescribed dose D_{pre} to a target and not exceeding a maximum dose D_{max} on given organs at risk (OAR) can be written as a minimization of a cost function χ^2 with respect to the vector $\vec{N}$ of all raster spots coming from all fields (Kraemer et al., 2000):

$$\chi^2(\vec{N}) = (w_T)^2 \sum_{i=1}^{N_T} \frac{\left(D_{pre} - D_i(\vec{N})\right)^2}{\Delta D_{pre}^2} + \left(w_{OAR}\right)^2 \sum_{i=1}^{N_{OAR}} \frac{\left(D_{max} - D_i(\vec{N})\right)^2}{\Delta D_{max}^2} \cdot \theta\left(D_i(\vec{N}) - D_{max}\right) \quad (8.1)$$

Here, θ is the Heavyside function, returning 0 for negative argument and 1 elsewhere, the summations are over the respective number N of voxels in the target (index T) and the OAR (index OAR), the weights w and the ΔD (with the respective indices) are adjustable a-priori settings for the relative importance of the OAR in the optimization.

8.2. From RBE to OER based optimization

Thus, the aim of biological treatment planning is to expand the concept of the doses prescribed to the target and limiting those doses to the OAR, with a specific definition including biological effects.

A conventional way to account for any biological effect is typically through a so-called dose modifying factor, or, better phrased, dose effectiveness factor (DEF). The DEF is a ratio of the doses in a specific irradiation condition to that of standard or normal conditions, both giving the same biological effect *S* on a given endpoint:

$$\boldsymbol{DEF} = \frac{\boldsymbol{D_{specialconditions}}}{\boldsymbol{D_{n.c.}}}\Big|_{\boldsymbol{sameeffect(S)}} \tag{8.2a}$$

$$\boldsymbol{DEF}([\boldsymbol{C}]) = \frac{\boldsymbol{D}([\boldsymbol{C}])}{\boldsymbol{D_{n.c.}}}\Big|_{\boldsymbol{sameeffect(S)}} \tag{8.2b}$$

where [*C*] is the concentration of a given sensitizer or protector species. As indicated in Eqs. 8.2, such specific conditions may refer either to the radiation, such as in RBE (relative biological effectiveness) weighted dose for a given particle field with respect to the dose from a standard X-ray irradiation. They may also refer to some target properties, such as the concentration of a given sensitizer or protector species. This is the case for the OER, which compares the doses in standard oxygenation (normoxia) to hypoxia, i.e., at a given oxygen concentration [O_2], typically indicated as a partial pressure of equilibrium, pO_2.

$$OER(pO_2, LET) = \frac{D(pO_2,LET)}{D(normoxia,LET)} \tag{8.3}$$

As indicated in Eq. 8.3, any DEF may depend on several parameters, as is the case for the dependence of OER on LET (linear energy transfer). This dependence is very strong, decreasing from a factor of about 3 to 1 and this is one of the additional merits of using high LET particles on hypoxic tumours. Such dependence is however quite complex and requires a specific model (e.g., (Scifoni et al., 2013)) to account for the full bidimensional range of values for any condition. It also requires a mapping of the actual oxygenation in the specific target, a feature which is becoming available through recent advances of functional imaging techniques, such as the PET tracers FMISO and FAZA (Horsman et al., 2014).

Thus, a typical RBE weighted optimization replaces the physical doses in Eq. 8.1 (denoted as D_i^{phys} in Eq. 8.4) with a biologically weighted dose D^{bio} or RBE weighted dose *RWD*, where

$$D_i^{bio}(\vec{N}) = D_i^{phys}(\vec{N}) \cdot RBE_i(\vec{N}) = RWD_{\mathrm{i}}. \tag{8.4}$$

In Eq. 8.4, the quantities are evaluated for any voxel *i* of the target and normal tissue, including the RBE according to its actual dependence on the number of particles. Such modification, now present in most particle treatment planning codes, is not trivial since it introduces a high non-linearity in the optimization task through the point-by-point RBE evaluation. This complicates the solution of the cost function minimization in the form of gradients (see Horcicka et al. (2012) for details). These gradients are the driving forces of the minimization, i.e., they "drive" the convergence of the number of particles for each spot, in the most convenient way.

When it comes to the adaptation of the treatment to account for hypoxia, the recently proposed idea of the kill-painting method (Tinganelli et al., 2015) is to exploit the advantage of a 3D mapping of oxygen content. This information is available – or soon to be available- as mentioned above, from functional imaging PET, which could be co-registered to a CT map to obtain multimodal information. Thus, D^{bio} can be extended to a $D^{bio\prime}$, which accounts, voxel by voxel, for the additional DEF introduced by the OER, thus leading to a RBE and OER weighted dose, *ROWD:*

$$ROWD_i(\vec{N}) = D_i^{bio\prime}(\vec{N}) = D_i^{phys}(\vec{N}) \cdot RBE_i(\vec{N})\, OER_i(\vec{N}) \tag{8.5}$$

Here, the OER at voxel i depends on the specific pO_2 in that voxel, in addition to the dependence on the LET realized by the specific local field generated by the particle arrangement (Tinganelli et al., 2015). This clearly also affects the gradient calculations, increasing the non-linearity of the problem, but also allows inclusion of the oxygenation map as the driving force of the optimization. This enables the automatic realization of an optimal LET distribution and concentrates the higher LET components in the less oxygenated regions, where they are more effective, as illustrated in Fig. 8.2.

This leads to a similar result as the so-called LET-painting method (Bassler et al., 2014), where dose ramps are applied to the particle fields, according to the oxygen distribution, which enter directly in the optimization.

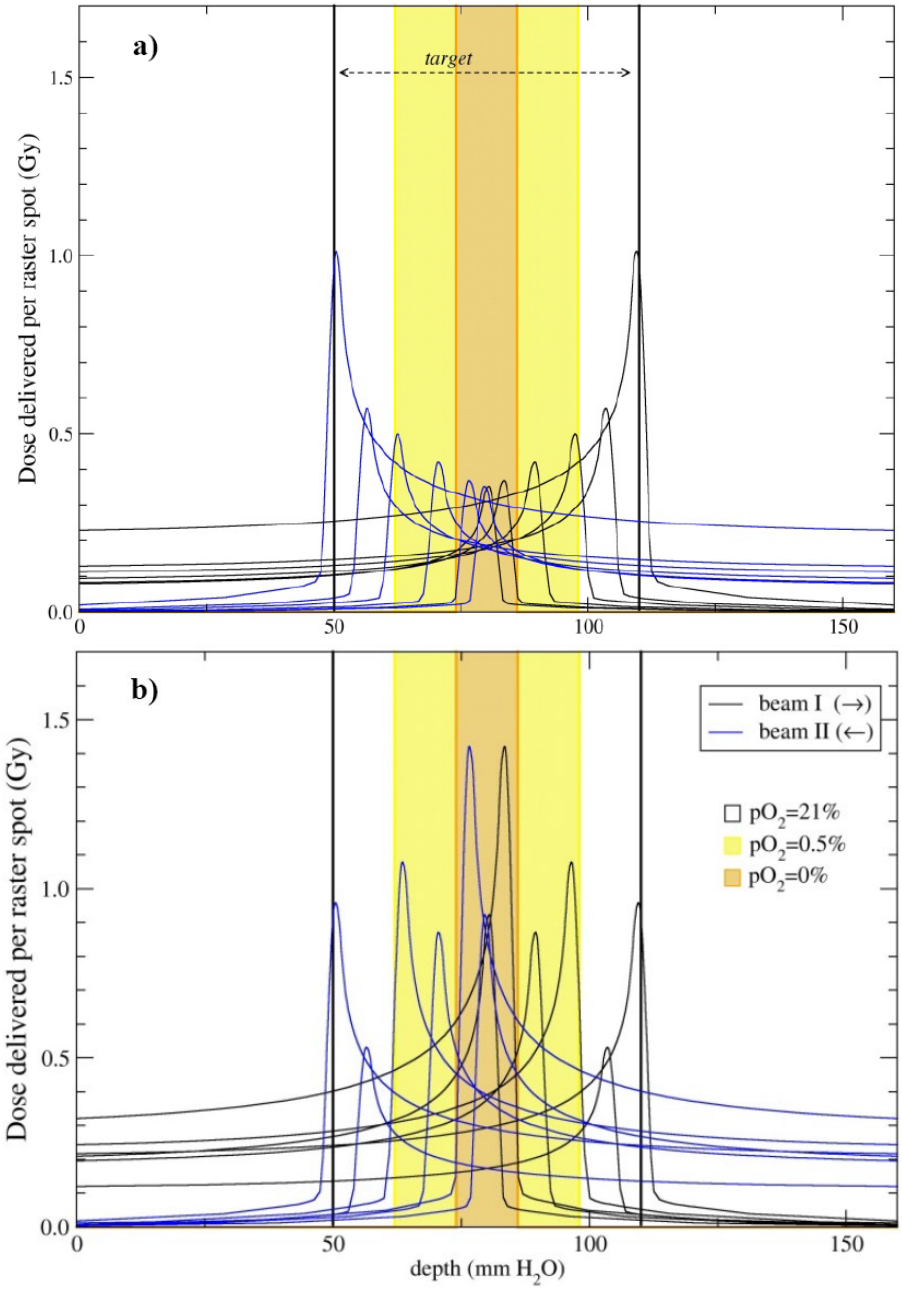

Fig. 8.2: Comparison of treatment plans based on the kill-painting method for two opposed fields of carbon ions, both leading to the same uniform biological dose in for the non-uniformly oxygenated target: (a) RWD optimization disregarding oxygenation; (b) ROWD optimization. Adapted from Tinganelli et al. (2015).

8.3. Multi-ion and multi-fraction biological optimization

In the attempt to use, as many degrees of freedom as possible of a particle beam irradiation, the concept of making non-uniform particle fields and non-uniform fraction sizes during a single treatment could be undoubtedly extremely attractive, albeit challenging.

8.3.1. Simultaneous optimization of multiple ion species

This is the case in the latest advancement of the use of different particle beams simultaneously, the so-called multi-ion optimization. The motivation for this is, firstly, the recent evaluation of the differential advantages of different particle beams, ranging from protons to oxygen, in particular the novel analysis of the physical and biological peculiarities of helium (Kraemer et al., 2016, Mairani et al., 2022) and oxygen beams (Sokol et al., 2017). Secondly, the latest technical ability of commercial ion-beam medical accelerators, (e.g., Toshiba ESS HIT, to perform a very fast switching and tuning between different ion sources connected to the irradiation beamline. This allows consideration of the use of different particles, and thus the exploitation of the different features, within the same treatment session.

First introduced by Kraemer et al. (2014), multi-ion optimization includes in the cost function the possibility to account for the full spectrum of primary and secondary particles generated in a given voxel by all different particle fields with, in general, different charge Z, and to optimize the particle numbers for each field according to physical and biological requirements. Different evolutions of this concept have been realized, mostly at NIRS in Japan (Inaniwa et al., 2020), HIT (Kopp et al., 2020) and GSI-TIFPA (Sokol et al., 2019) in Europe, the latter mostly focused on hypoxic tumour irradiations.

An exemplary view of the potential of such approaches is shown in Fig. 8.3, where a tumour with a given oxygenation map is irradiated with a combined helium and oxygen beam, adopting multi-ion kill painting, leading to optimal coverage of the *ROWD*. Taking advantage of the oxygen beam properties, this beam is concentrated in the most hypoxic regions.

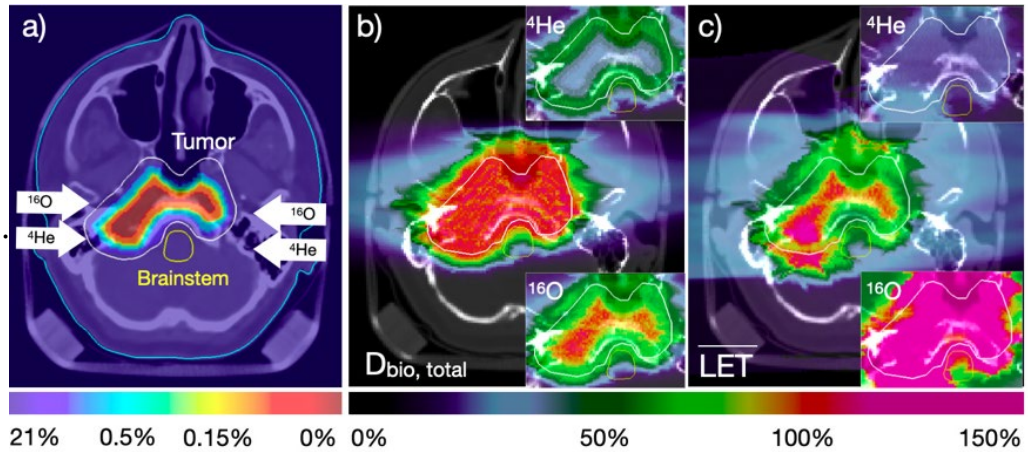

Fig. 8.3: Exemplary plan with multiple ion fields optimized for getting a uniform biological dose in the target, accounting for the different hypoxic levels. From Sokol et al. (2019).

New avenues for these types of treatments have been opened very recently through the exploitation of particle arc therapy, where the potential of multiple ions can be even more profitably exploited (Mein et al., 2022).

8.3.2. Simultaneous optimization of multiple fractions

Another frontier is characterized by the, still biology driven, flexibility of the different fractions of irradiation. Beyond the standard paradigm of delivering all identical plans during the several fractions of a treatment, this approach attempts to exploit the possibility of combining different plans, in a similar way as the different fields of a multiple field optimized irradiation are computed.

Of course, the complication arising in this case is the impossibility of neglecting the temporal features related to the damage processing following the previous course of irradiation. For this reason, a full spatiotemporal optimization is necessary. After the initial proposition by Unkelbach et al. (2013), a very advanced application to a prostate clinical case was proposed by Manganaro et al. (2022), where the novel approach was shown to improve both standard and hypofractionation (i.e., delivering the dose in few fractions) regimes, but also to allow more robust biological outcomes.

8.4. NTCP based optimization

Another direction to account for biological effects in treatment planning is to link the outcome not on purely dosimetric indices, but rather directly on the clinical response, i.e., on the tumour control probability (TCP) or on the normal tissue complication probability (NTCP).

The latter, in particular, has a challenging role, since the biological effect on the normal tissue, in contrast to the effect on the tumour, is not that strictly and directly linked to a quantity such as cell killing or some other easily measurable *in vitro* endpoint. For this reason, reducing the dose to normal tissue is not necessarily proportionally related to sparing normal tissue. This is because a typical NTCP dependence on dose is not only sigmoidal, but linked to a quantity that takes into account a volumetric index of the dose coverage, i.e., considering serial or parallel characteristics of the irradiated normal tissues and organs at risk.

An example of a convenient way to account for this was recently proposed by Battestini et al. (2022). The approach is to replace the key dosimetric quantity in the OER part of Eq. 8.1 with a *generalized equivalent uniform dose*, *gEUD*, a quantity taking into account the volume effect, mixing all N voxels of an OAR through a parameter a, which quantifies the level of "seriality" of a given organ (i.e., to what extent collective effects of damage on several voxels play a role):

$$gEUD = \left(\frac{1}{N}\sum_{i=1}^{N}\left(D_i^{bio}\left(\vec{N}\right)\right)^{a}\right)^{\frac{1}{a}} \tag{8.6}$$

Seriality implies that the biological dose D_i^{bio} in each voxel i depends on all other voxels, as indicated by $\vec{N}$. This leads to a new objective function

$$\chi^2\left(\vec{N}\right) = (w_T)^2 \sum_{i=1}^{N_T} \frac{\left(D_{pre} - D_i\left(\vec{N}\right)\right)^2}{\Delta D_{pre}^2} + \left(w_{OAR}^{gEUD_0}\right)^2 \frac{\left(gEUD_0 - gEUD\left(\vec{N}\right)\right)^2}{\Delta gEUD_0^2} \cdot \theta\left(gEUD\left(\vec{N}\right) - gEUD_0\right) \tag{8.7}$$

As in Eq. 8.1, θ is the Heavyside function, returning 0 for negative argument and 1 otherwise. The summation is over the number N of voxels in the target. In the term related to the OAR, the sum over the voxels in the OAR of dose has been replaced by *gEUD*. Accordingly, the (new) weights and factors are labelled in Eq. 8.7 with the superscript $gEUD_0$. This approach returns a much-improved coverage across the volume of the indicated OAR, which has an impact on the NTCP of such an organ, as can be seen in Fig. 8.4.

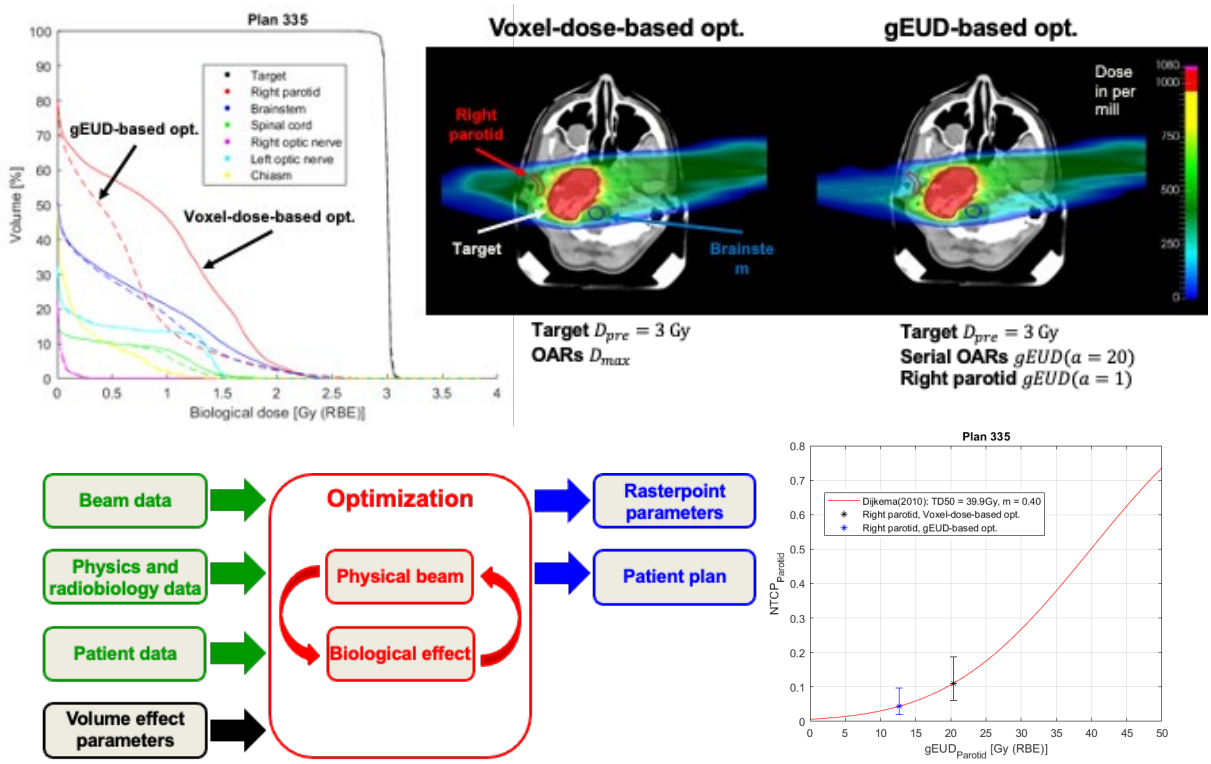

Fig. 8.4: Example of gEUD based optimization with carbon ion fields compared to voxel-based optimization, sparing a parotid gland during a head tumour irradiation. Upper panels: dose volume histograms and dose 3D maps, lower panels: scheme of the optimization and impact on the NTCP. Modified from Battestini et al. (2022).

8.5. FLASH radiotherapy and FLASH planning

8.5.1. The FLASH effect

A revolutionary wave in the radiotherapy community appeared in the last 7-8 years since Vincent Favaudon et al. (2014) reported a revived use of ultrahigh dose rate which had been largely explored in radiobiology studies of the 1950s. Ultra-high dose rate gives a remarkable protective effect as compared to conventional dose rate radiation (normally indicated as CONV), while maintaining the same efficacy on tumours (Favaudon et al., 2014). From a steadily accumulating set of experimental results, in vitro and in vivo, confirming such an effect, it became evident that the normal tissue sparing effect of FLASH irradiation is associated with the physical irradiation parameters exceeding thresholds, i.e., an average dose rate of around 40 Gy/s and an overall delivered dose of around 10 Gy. However, the different values reported in the continuously enlarging panorama of available experimental data indicates several deviations from these strict thresholds. Parameters other than the above-mentioned ones have also been highly debated, depending both on the irradiation modality (dose per pulse, intra-pulse dose rate, pulse duration, quality of radiation) and on the irradiated tissue characteristics (oxygenation, tissue type etc.). To date the FLASH effect has been observed, with different frequency, in a broad range of radiation types, including photons, electrons protons and heavier ions (Limoli and Vozenin, 2023).

A major challenge in this context is presently the mechanistic understanding of the underpinning process, the explanation of the protective effect, contradicting decades of radiobiology, in particular the opposite trend of effectiveness versus dose rate occurring at the lower end of the dose rate

ranges explored in standard experiments. Even more challenging appears the explanation of the differential behaviour of normal versus tumour tissue, and the correlation of the latter effect with the range of observed thresholds. An exponentially growing amount of modelling and experimental investigations, proposing or confuting alternative explanations, have been published in the last five years (as reviewed, e.g., in Limoli and Vozenin, 2023).

Other challenges address the production and delivery of ultra-high dose rate beams of different types (electrons, photons, ions), through dedicated acceleration and beam transport techniques, and their dosimetric control. The latter issue originates in the typical saturation encountered by conventional dosimetric and beam monitoring systems (such as ionization chambers) when, in contrast to standard irradiation modalities, the extremely high dose rates increase the probability of local recombination and other non-linear effects. The need to overcome this problem is of utmost importance not only for the safe clinical exploitation of FLASH, but also for accurate verification of ongoing experiments, where the exact ratio of doses, CONV over FLASH, is the crucial observable defining the sparing factor.

8.5.2. FLASH in Biological Treatment Planning

The evidence of these thresholds for both the dose and the dose rate, brilliantly collected and emphasized in a recent work using a simple phenomenological model (Boehlen at al., 2022) which is purely based on data rather than on mechanistic hypotheses, called for the need to consider this sparing effect in treatment planning and to include it in the optimization process. In fact, in most irradiation facilities, the available dose rates are not much smaller than the indicated thresholds. Thus, a careful redistribution of the particle fields – protons and very high energy electrons (VHEE)– is necessary to realize the required parameters in the relevant regions of the irradiated tissues. Moreover, the actual definition of local dose rate at a specific voxel level, e.g., in a beam scanning irradiation, due to the successive accumulation of different beam portions across the scanning process, is not obviously clear. This stems from the present lack of understanding of the FLASH mechanism, so that it is not clear at which local level a dose rate may be significant. Several different metrics have been suggested for defining an *effective* dose rate, useable at a voxel level, summing up the dose contributions from all the different spots to that specific voxel. Among them, the dose averaged dose rate (DADR) is the most used, which weights each beamlet with the delivered dose, in analogy to the dose averaged LET. This is based on the hypothesis that the biological effectiveness can be captured in this way.

A visualization of the local dose rate experienced during the scanning of a carbon beam field is shown in Fig. 8.5 (Weber et al., 2021).

According to the specific dose rate definitions, this implies that biological optimization approaches are dedicated to concentrating the highest dose rate on the more critical voxels of organs at risk in order to maximize the onset of the FLASH sparing action.

Among the many activities in this field, it is worth mentioning the *simultaneous dose and dose rate optimization* SDDRO approach, introduced by Gao et al. (2020), which remarkably allows to introduce in the cost function a metric for both the dose and the dose rate, enabling a simultaneous optimization of the desired quantities.

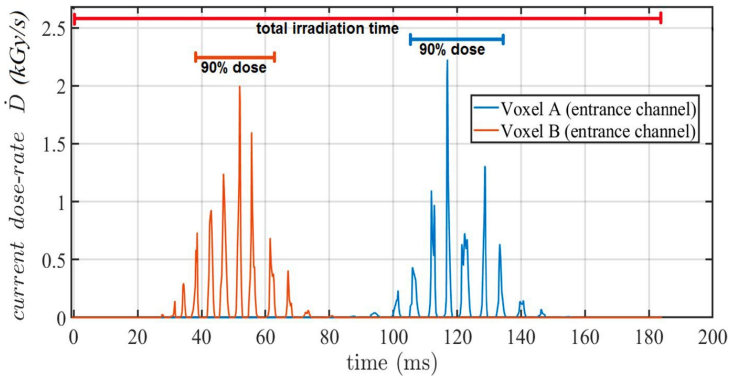

Fig. 8.5: Plot of the actual instantaneous dose rates verified in 2 randomly chosen voxel positions across the timestamp of a FLASH irradiation with carbon beams. Modified from Weber et al. (2021).

8.6. Summary and Conclusions

An overview of some of the ongoing efforts in extending particle therapy treatment planning to account for biological effects of different types and levels, so called biological treatment planning, has been given. It has been stressed how the flexibility of particle beam irradiations allow exceptional customization of the plans in terms of dose, LET and, in general, the local field of radiation.

The parallel advances in imaging and characterization of biological targets provide the ideal complement for exploiting these novel features. On the other hand, it should be mentioned that a present limit of these advanced planning approaches is the affordability of such imaging information, which is also known to vary with time. Thus, the robustness of these plans is a major question, which often may lead to the choice of more conservative approaches. However, the availability of such tools may offer instruments for assessment of the different patient cases and to guide the patient allocations (i.e., which patients are assigned to which therapies) on model-based criteria as already suggested for proton therapy (Langendijk et al., 2013).

Biological treatment planning is expanding increasingly in different directions, including the definition of the biological quantity to be optimized. In this context, it is worth mentioning as an outlook that beyond what has been described in this article, a new approach has recently been proposed of using nanodosimetry-based quantities as additional optimization targets in treatment planning (Ramos Mendez et al., 2018, Faddegon et al., 2023). This promising approach would exploit the close connection of nanodosimetric quantities to the radiobiological effectiveness to assess the biological effects of the particle field voxel by voxel based on a mechanistic radio-biophysical model.

8.7. References

Bassler, N., Toftegaard, J., Lühr, A., Sørensen, B.S., Scifoni, E., Krämer, M., Jäkel, O., Mortensen, L.S., Overgaard, J., Petersen, J.B., 2014. LET-painting increases tumour control probability in hypoxic tumours. Acta Oncologica, 53, 25-32.

Battestini, M., Schwarz, M., Krämer, M., Scifoni, E. (2022). Including Volume Effects in Biological Treatment Plan Optimization for Carbon Ion Therapy: Generalized Equivalent Uniform Dose-Based Objective in TRiP98. Frontiers in Oncology, 12, 555.

Böhlen, T. T., Germond, J. F., Bourhis, J., Vozenin, M. C., Ozsahin, E. M., Bochud, F., Bailat, C., Moeckli, R., 2022. Normal tissue sparing by FLASH as a function of single-fraction dose: a quantitative analysis. International Journal of Radiation Oncology* Biology* Physics, 114, 1032-1044.

Choi, K., Mein, S. B., Kopp, B., Magro, G., Molinelli, S., Ciocca, M., Mairani, A., 2018. FRoG – A new calculation engine for clinical investigations with proton and carbon ion beams at CNAO. Cancers, 10, 395.

Durante, M., Flanz, J., 2019. Charged particle beams to cure cancer: strengths and challenges. Seminars in Oncology 46, 219-225.

Faddegon, B., Blakely, E.A., Burigo, L., Censor, Y., Dokic, I., Domínguez Kondo, N., Ortiz, R., Ramos Méndez, J., Rucinski, A., Schubert, K., Wahl, N., Schulte, R., 2023. Ionization detail parameters and cluster dose: a mathematical model for selection of nanodosimetric quantities for use in treatment planning in charged particle radiotherapy. Physics in Medicine and Biology 68, 175013. https://doi.org/10.1088/1361-6560/acea16.

Favaudon, V., Caplier, L., Monceau, V., Pouzoulet, F., Sayarath, M., Fouillade, C., Poupon, M.-F., Brito, I., Hup´, P., Bourhis, J., Hall, J., Fontaine, J.-J., Vozenin, M. C. (2014). Ultrahigh dose-rate FLASH irradiation increases the differential response between normal and tumor tissue in mice. Science Translational Medicine, 6, 245ra93.

Gajewski, J., Garbacz, M., Chang, C. W., Czerska, K., Durante, M., Krah, N., Krzempek, K., Kopeć, R., Lin, L., Mojżeszek, N., Patera, V., Pawlik-Niedzwiecka, M., Rinaldi, I., Rydygier, M., Pluta, E., Scifoni, E., Skrzypek, A., Tommasino, F., Schiavi, A., Rucinski, A., 2021. Commissioning of GPU–accelerated Monte Carlo Code FRED for clinical applications in proton therapy. Frontiers in Physics, 8, 567300.

Gao, H., Lin, B., Lin, Y., Fu, S., Langen, K., Liu, T., Bradley, J., 2020. Simultaneous dose and dose rate optimization (SDDRO) for FLASH proton therapy. Medical Physics, 47, 6388-6395.

Gemmel, A., Hasch, B., Ellerbrock, M., Weyrather, W.K., Krämer, M., 2008. Biological dose optimization with multiple ion fields. Physics in Medicine and Biology, 53, 6991.

Horcicka, M., Meyer, C., Buschbacher, A., Durante, M., Krämer, M., 2012. Algorithms for the optimization of RBE-weighted dose in particle therapy. Physics in Medicine and Biology, 58, 275.

Horsman, M.R., Mortensen, L.S., Petersen, J.B., Busk, M., Overgaard, J., 2012. Imaging hypoxia to improve radiotherapy outcome. Nature Reviews Clinical Oncology, 9, 674-687.

Inaniwa, T., Suzuki, M., Lee, S.H., Mizushima, K., Iwata, Y., Kanematsu, N., Shirai, T., 2020. Experimental validation of stochastic microdosimetric kinetic model for multi-ion therapy treatment planning with helium-, carbon-, oxygen-, and neon-ion beams. Physics in Medicine and Biology, 65, 045005.

Kopp, B., Mein, S., Dokic, I., Harrabi, S., Böhlen, T. T., Haberer, T.,... Mairani, A., 2020. Development and validation of single field multi-ion particle therapy treatments. International Journal of Radiation Oncology* Biology* Physics, 106, 194-205.

Krämer, M., Jäkel, O., Haberer, T., Kraft, G., Schardt, D., Weber, U., 2000). Treatment planning for heavy-ion radiotherapy: physical beam model and dose optimization. Physics in Medicine and Biology, 45, 3299.

Krämer, M., Scholz, M., 2000. Treatment planning for heavy-ion radiotherapy: calculation and optimization of biologically effective dose. Physics in Medicine and Biology, 45, 3319.

Krämer, M., Scifoni, E., Schmitz, F., Sokol, O., Durante, M., 2014. Overview of recent advances in treatment planning for ion beam radiotherapy. The European Physical Journal D, 68, 306.

Krämer, M., Scifoni, E., Schuy, C., Rovituso, M., Tinganelli, W., Maier, A., ... Durante, M., 2016. Helium ions for radiotherapy? Physical and biological verifications of a novel treatment modality. Medical Physics, 43, 1995-2004.

Langendijk, J. A., Lambin, P., De Ruysscher, D., Widder, J., Bos, M., Verheij, M., 2013. Selection of patients for radiotherapy with protons aiming at reduction of side effects: the model-based approach. Radiotherapy and Oncology, 107, 267-273.

Limoli, C. L., Vozenin, M. C., 2023. Reinventing radiobiology in the light of FLASH radiotherapy. Annual Review of Cancer Biology, 7, 1-21.

Mairani, A., Brons, S., Cerutti, F., Fassò, A., Ferrari, A., Krämer, M., ... Sommerer, F., 2010. The FLUKA Monte Carlo code coupled with the local effect model for biological calculations in carbon ion therapy. Physics in Medicine and Biology, 55, 4273.

Mairani, A., Mein, S., Blakely, E., Debus, J., Durante, M., Ferrari, A., ... Weber, U., 2022. Roadmap: helium ion therapy. Physics in Medicine and Biology, 67, 15TR02.

Manganaro, L., Russo, G., Cirio, R., Dalmasso, F., Giordanengo, S., Monaco, V.,... Attili, A., 2017. A Monte Carlo approach to the microdosimetric kinetic model to account for dose rate time structure effects in ion beam therapy with application in treatment planning simulations. Medical physics, 44, 1577-1589.

Manganaro, L., Attili, A., Bortfeld, T., Paganetti, H., 2022. Spatiotemporal optimisation of prostate intensity modulated proton therapy (IMPT) treatments. Physics in Medicine and Biology, 67, 045005.

Mein, S., Tessonnier, T., Kopp, B., Schömers, C., Harrabi, S., Abdollahi, A., ... Mairani, A., 2022. Biological dose optimization for particle arc therapy using helium and carbon ions. International Journal of Radiation Oncology* Biology* Physics, 114(2), 334-348.

Polster, L., Schuemann, J., Rinaldi, I., Burigo, L., McNamara, A. L., Stewart, R. D., ... Paganetti, H., 2015. Extension of TOPAS for the simulation of proton radiation effects considering molecular and cellular endpoints. Physics in Medicine and Biology, 60(13), 5053.

Rana, S., Greco, K., Samuel, E.J.J., Bennouna, J., 2019. Radiobiological and dosimetric impact of RayStation pencil beam and Monte Carlo algorithms on intensity-modulated proton therapy breast cancer plans. Journal of Applied Clinical Medical Physics, 20, 36-46.

Scifoni, E., Tinganelli, W., Weyrather, W. K., Durante, M., Maier, A., Krämer, M., 2013. Including oxygen enhancement ratio in ion beam treatment planning: model implementation and experimental verification. Physics in Medicine and Biology, 58, 3871.

Sokol, O., Scifoni, E., Tinganelli, W., Kraft-Weyrather, W., Wiedemann, J., Maier, A., ... Krämer, M., 2017. Oxygen beams for therapy: advanced biological treatment planning and experimental verification. Physics in Medicine and Biology, 62(19), 7798.

Sokol, O., Krämer, M., Hild, S., Durante, M., Scifoni, E., 2019. Kill painting of hypoxic tumors with multiple ion beams. Physics in Medicine and Biology, 64, 045008.

Sokol, O., Durante, M., 2023. Carbon Ions for Hypoxic Tumors: Are We Making the Most of Them? Cancers 2023, 15, 4494.

Tinganelli, W., Durante, M., Hirayama, R., Krämer, M., Maier, A., Kraft-Weyrather, W., ... Scifoni, E., 2015. Kill-painting of hypoxic tumours in charged particle therapy. Scientific Reports, 5, 17016.

Unkelbach, J., Zeng, C., Engelsman, M., 2013. Simultaneous optimization of dose distributions and fractionation schemes in particle radiotherapy. Medical Physics, 40, 091702.

Weber, U. A., Scifoni, E., Durante, M., 2022. FLASH radiotherapy with carbon ion beams. Medical Physics, 49, 1974-1992.

Wieser, H. P., Cisternas, E., Wahl, N., Ulrich, S., Stadler, A., Mescher, H., ... Bangert, M., 2017. Development of the open-source dose calculation and optimization toolkit matRad. Medical Physics, 44, 2556-2568.

9. Personal online dosimetry using flexible computational phantoms

Pasquale Lombardo, **Abdelrahman Mahmoud**, Nuclear Research Centre (SCK.CEN), Belgium

Abstract

This chapter discusses the current state of development of the PODIUM project personal online dosimetry system, its potential advantages and the current limitations. The evolution of computational dosimetry over the past decade has contributed to a significant transformation in the radiation protection and dosimetry fields, allowing more accurate and individualized dose assessments. With the development of increasingly flexible computational phantoms, computational dosimetry can offer unprecedented accuracy and personalization in dose assessments. This evolution from physical dosemeters to comprehensive, real-time computational models enables direct estimation of protection quantities across the entire body, overcoming limitations inherent in traditional dosimetry methods.

´Through the integration of marker-less computer vision for personnel tracking and advances in Monte Carlo simulations, AI models, and the inclusion of a virtual reality environment, the PODIUM online dosimetry system aims at providing a powerful dosimetry tool for significantly enhancing radiation protection. Despite current challenges such as tracking accuracy and the complexity of extensive validation measurements, online dosimetry systems can effectively address the need of more individualized and effective radiation protection strategies.

9.1. Introduction

In the last decade, there has been consistent demand within the radiation protection and dosimetry scientific communities for higher accuracy and individualization of dose assessment. In this context, computational dosimetry has consolidated its key role in dosimetry, as it can effectively provide the tools required to improve accuracy, personalization and potentially even enhance the effectiveness of radiation protection.

9.1.1. Advantages of Computational Dosimetry

Thanks to their computational nature, simulations can push the boundaries beyond what is possible with current physical dosemeters, delivering more efficient and comprehensive dosimetry data. The most obvious advantage is the fact that by using computational phantoms, computational dosimetry allows the direct estimation of protection quantities, bypassing the need for operational quantities. In other words, with simulations, we are not bound to single measurement points outside the body, but we can calculate dose distributions throughout the whole body, including organ doses. With the recent introduction of flexible computational phantoms such as the realistic anthropomorphic flexible (RAF) phantom family of SCK CEN (Lombardo et al., 2018), simulations can now even account for the effect of posture on organ and extremity doses, allowing a more realistic representation of real exposure scenarios.

Furthermore, simulations can estimate energy depositions without being subject to typical limitations of dosemeters, such as limited sensitivity to low doses, saturation at high dose rates, energy, or angular dependences. In addition, simulations can outperform the most advanced

dosemeters by providing deep analytical metrics, such as spectrum histograms and classification of energy deposition events with microscopic resolution.

9.1.2. From dosimeters to Personal Online Dosimetry based on computer simulations

In a broad sense, computational dosimetry has not only the potential for complementing conventional dosimetry, but we are approaching the moment at which it will completely supersede physical dosemeters. Following the approach initiated by the PODIUM (Personal Online DosImetry Using computational Methods) project in occupational monitoring (Abdelrahman et al., 2020), more and more research is going towards replacing physical dosimeters with a monitoring system based on pure computational methods, whilst providing accurate and possibly close to real-time dose reports.

Thanks to its computer vision framework for tracking of persons and object by means of cameras, the Personal Online Dosimetry system envisioned by PODIUM can infer and reconstruct the movements of the people exposed to radiation at any given moment and translate this information to a flexible computational phantom. The coupling of real-word movements with flexible phantoms allows the generation of personalized simulations reproducing the monitored scene with unprecedented comprehensiveness and realism, addressing the demand for higher accuracy and individualization in dosimetry.

Besides the above-mentioned dosimetry advantages, the PODIUM personal dosimetry system also aims at increasing the effectiveness of radiation protection in two aspects.

First, a computational dosimetry system can also be used to emulate realistic exposure situations in a Virtual Reality environment, i.e., similar to a videogame. This approach can be extremely effective in the training of exposed workers, potentially saving both time and costs, and improving radiation protection education. Thanks to its "visualization" capabilities, VR allows radiation fields to be "seen", thus educating workers to fully understand the value of the ALARA principle.

Second, by exploiting the real-time aspects, the computational dosimetry system is used to warn workers approaching or surpassing high dose rate thresholds and possibly even guide their actions towards a reduction of the dose rate.

9.1.3. Current state of the art

The first version of the Personal Online Dosimetry system was developed during the PODIUM European project. In PODIUM, the main applications of the dosimetry system were monitoring interventional radiology (IR) personnel and monitoring nuclear workers exposed to neutron fields (such as those coming from a nuclear reactor fuel assembly). By the conclusion of the project, a first set of validations had been performed in both applications, proving the feasibility of performing dosimetry with pure computational methods. Since then, several initiatives at European level have taken forward the PODIUM concept, applying similar approaches for improving dosimetry monitoring in relevant applications.

By far the most explored application has been interventional radiology. Due to the high dose rates and the high variability in this imaging technique, interventional radiology constitutes an ideal study case for a dosimetry system based on simulations. Some systems (Badal et al., 2013) are focused on the imaging and patient radiation protection aspects, while others, like PODIUM's, address primarily staff monitoring (Abdelrahman et al., 2020).

9.1.4. Development status of the SCK CEN Personal Online Dosimetry system

The Personal Online Dosimetry system currently under development at SCK CEN carries over the experience and the achievements obtained during the PODIUM project while updating the technology and resolving some of the limitations of the original framework. These new developments allowed the extension of the applications of online dosimetry to monitoring nuclear medicine staff and personnel involved in decommissioning activities in nuclear power plants.

The improvements include several meliorations of the tracking system, a larger set of flexible phantoms for the dose calculation (now including an adult female and, less relevant for monitoring, a 1-year-old child), the possibility of using the open-source Monte Carlo transport code Geant4 (besides the export-controlled MCNP) and a set of optimization tools for the simulations based on machine learning.

Apart from improvement of the technology and dosimetry accuracy of the system, integration and data management aspects are becoming one of the main focuses at the current development stage. Improving these aspects means assuring a seamless compatibility between various components of the system and the environment where the system is installed, and the effective processing, analysis and communication of the dosimetry data produced. The emphasis on these facets ensures that the Personal Online Dosimetry system not only functions optimally, but also aligns with the current technological standards and requirements in the field where it is deployed, be it interventional radiology, nuclear medicine or decommissioning of nuclear installations.

In order to ensure accuracy and robustness, each new development requires performing extensive validations under operational conditions, i.e., within actual interventional radiology rooms, nuclear medicine departments, and so forth. Due to difficulties in accessing clinical and nuclear facilities during the peak years of the COVID pandemic (2020-2021) and due to the new safety protocols adopted since then, the validation of new technologies developed for the SCK CEN online dosimetry system were postponed several times. For this reason, validation will become the main priority of our computational dosimetry research in the next years.

9.2. Material and methods

The Personal Online Dosimetry system envisioned by PODIUM is constituted by four main elements or modules. The first is the flexible computational phantom model, which is used for performing personalized dose calculations. The second element is the computer vision tracking framework, which by making use of 3D cameras, is used to track person, object, and source positions. The third module is constituted by the Monte Carlo simulation framework including source definition and optimization algorithms. Lastly, the visualization module, which by means of a Virtual Reality environment allows the graphical rendition of the results of the simulations, both for ALARA training and for providing real-time feedback to exposed personnel.

9.2.1. Flexible Computational Phantoms

In order to fit both the accuracy and flexibility requirements, the phantoms used in the personal online dosimetry system, constituting the realistic anthropomorphic flexible (RAF) phantom family, were developed using the polygonal mesh (PM) boundary-representation (B-Rep) method. The RAF phantom family currently includes an adult male (AM) phantom, an adult female (AF) and a 1-year-old female (1YOF) phantom. These phantoms were modelled based on three-dimensional

anatomical atlases, ICRP Publications 89, 110 and 145 reference data (ICRP, 2002, 2010, 2020), and reference data for the Belgian population (Motmans, 2005).

In PM phantoms, the organs are represented by means of interconnected triangles and four-sided polygons, i.e., meshes, outlining the external surface of the organ. PM modelling is currently the gold standard in videogame development, which implies that a large set of advanced software tools is available for modelling and animating. For developing most of RAF phantom organs, the Autodesk 3Ds Max (Autodesk, San Francisco, California, USA) software was used. In the case of the skin, muscles, and bones, both 3Ds Max and the open-source code Blender (Stichting Blender Foundation, Amsterdam, Netherlands) were used.

Most of the organs were developed starting from a simple object, such as a box or a sphere, whose vertices, edges, and faces are stretched, subdivided, and extruded in order to reproduce the shape of each organ. In order to achieve realistically shaped organs with very complex surfaces such as blood vessels, brain, or intestines, some of the mesh deformations were performed using the advanced "modifier" tools of 3Ds Max rather than only manual editing of vertices/edges and faces. Blender was primarily used to refine the topology of larger tissues so that the triangles and quads defining the organ were well organised and easy to control. In the case of the RAF phantoms, Blender's extensive set of re-topology tools proved to be extremely helpful in re-organizing the mesh topology. Having a clean mesh topology was crucial for enabling phantom flexibility, and to optimize computational performance both during the creation of the organ models, and later for the conversion to Monte Carlo input files.

One of the biggest advantages of PM modelling is the comprehensive software framework for creating computer animations. By using 3Ds Max animation framework and scripting tools, a mathematical skeleton system for simulating the natural joint motion was integrated into the three phantoms from the RAF family. Because of the mathematical skeleton, the RAF phantom postures can be easily tuned, without "breaking the bones". The main toolsets used in this step were the "biped" and "bones" rigging tools and the "skinning" modifiers, which offer accurate and easy-to-use tools for human animation. However, the workflow used to animate the phantom had to be tailored in a slightly different manner for each of the three phantoms. Animation tools are normally meant to be used for videogame characters to move, so they might trigger unexpected behaviours where some meshes might overlap each other, especially at microscopic scale. Small overlaps do not constitute a problem in videogames, but they may result in errors during the conversion of the phantom to an input format compatible with MC code. For this reason, special precautions had to be taken to not incur unwanted overlapping among organs of the phantoms during animations. Combined joint rotations allowed to accurately reproduce most human movements, with the objective of simulating more realistic external exposures. This capability of the RAF phantom is particularly relevant for monitoring exposed workers whose doses to inner organs, eyes, or extremities are known to be affected by the body posture, and, thus, for improving their protection.

To easily control the posture of the phantom without needing the graphic modelling software (3Ds Max) and the knowledge needed to control the mathematical skeleton, stand-alone software was developed. The software, named Interactive Posture Program (IPP) allows the posture of the phantoms to be easily controlled and the required format conversions to be performed for using the phantoms with MC codes. Figs. 9.1, 9.2 and 9.3 show the interface and some of the capabilities of IPP.

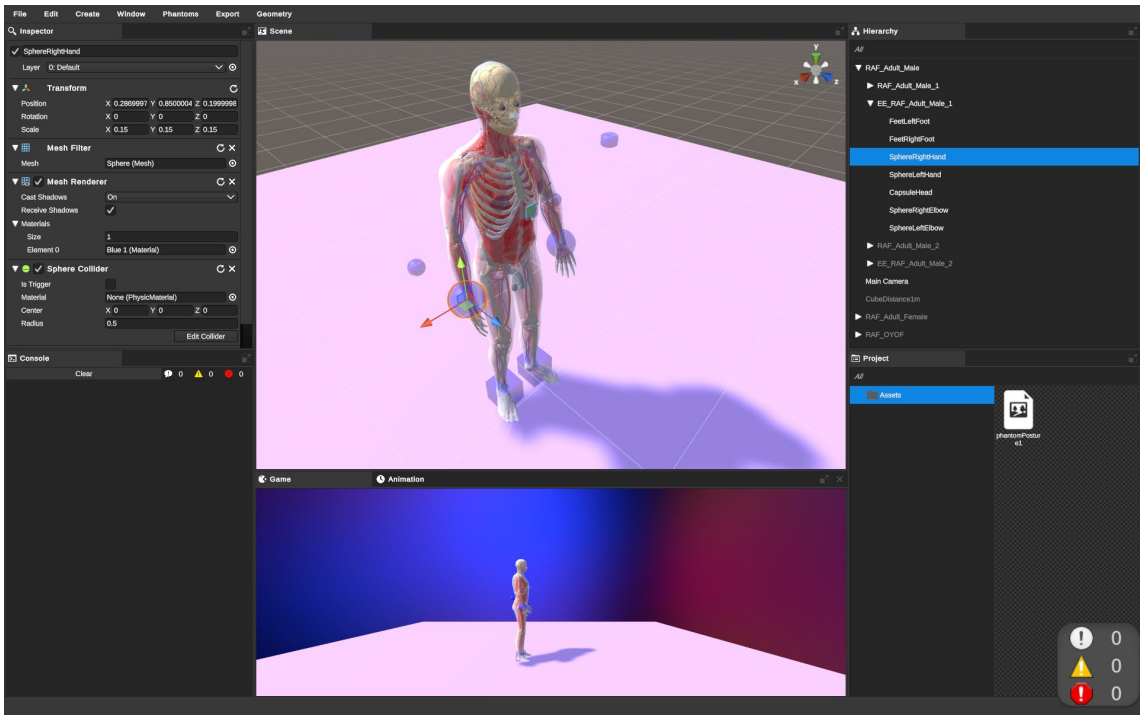

Fig. 9.1: Main interface of the Interactive Posture Program (IPP), showing the adult male phantom of the RAF phantoms family.

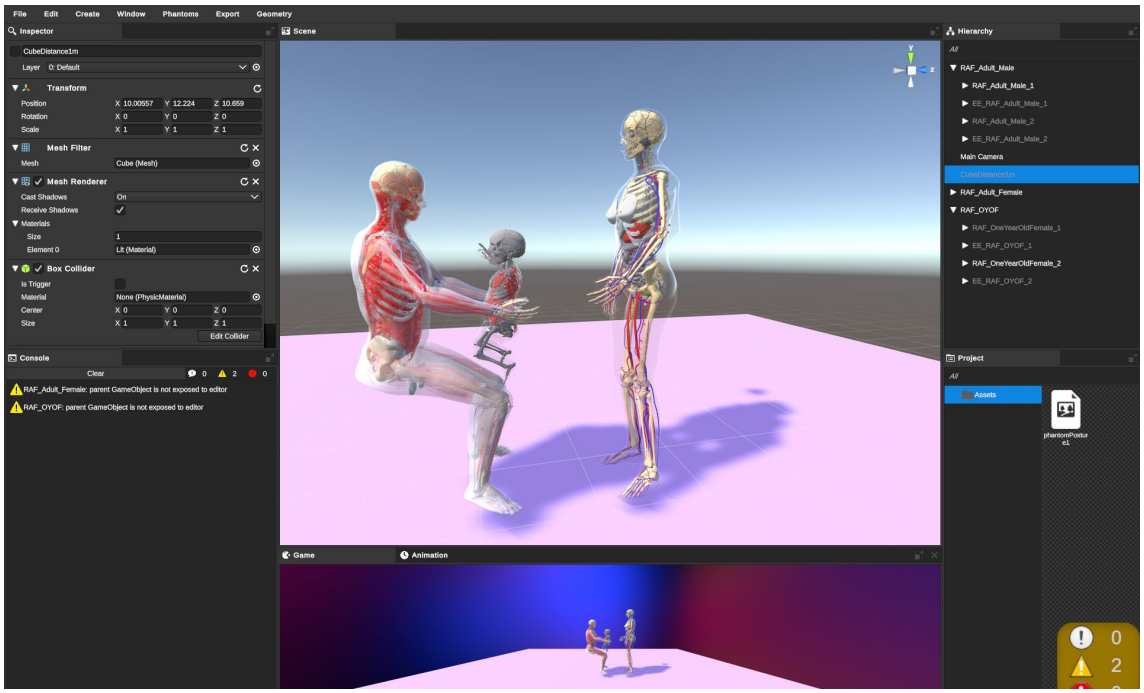

Fig. 9.2 Main interface of the Interactive Posture Program (IPP), showing an interaction between the adult male, adult female, and 1-year old female phantoms

A variant of the animation framework was also implemented for deforming the phantoms' anatomy and simulating different body types, or different age groups. However, by default. the RAF phantom family was locked out with this feature, as it triggered an excessive number of uncontrolled overlaps between meshes belonging to different tissues.

While the PM format is ideal in the modelling and animation stages of a computational phantom, PM geometries are not yet completely supported by Monte Carlo codes. This is mainly due to the

fact that PMs are surface objects that do not define a volume explicitly. On the one hand, this feature is beneficial in the modelling and animation stages, as it allows overlapping and stacking of organ meshes. On the other hand, for an MC code it is not trivial to classify whether a particle enters or exits an organ when it traverses an organ surface, especially if the surface is complex or characterized by concave shapes. Among all MC codes, Geant4 offers the most advanced tools regarding the loading of PM models with its G4TasseletedSolid class and its GDML (Geometry Description Markup Language) format. However, by the time of this report it was found that the RAF phantoms could not be loaded correctly in Geant4, leading to errors such as overlapping volumes and invalid facets errors. Even when reducing the phantom models by stripping a few organs, energy depositions were not scored correctly in the innermost tissues. These issues were mainly related to tissues such as blood vessels, bones, and muscles that, being relatively large, are likely to overlap with several other organs. In principle, the overlapping could be solved by developing a method to automatically sub-segment tissues in PM format at the interface of other organs, so that their volumes could be arranged using the hierarchy tree structure available in Geant4. However, such an automated segmentation feature has not yet been implemented.

Thus, to be able to use the phantoms, a voxelization algorithm was developed. By running an intersection test iteratively, the algorithm assigns voxels to each organ in a grid. Following the topological voxelization methodology of Laine (2013), the intersection test uses a parallelepiped as intersection object. The intersection parallelepiped was defined to have the same size of a voxel, but it was centred at the nodes of the voxel grid rather than at the centre of each voxel. To speed up the calculation, the algorithm was implemented on GPU using C# with DirectX, and C++ with CUDA API. If a standard or low-end GPU is present, the algorithm uses compute shaders from DirectX11 to perform the voxelization. If a NVIDIA GPU is available, the calculation is run using the faster and more efficient CUDA's compute shaders. In the first case, the maximum supported voxel grid size corresponds to 512 million voxels. In the second case, there is no theoretical limit: as long as there is sufficient GPU-RAM (or shared CPU-RAM) memory, the algorithm can handle voxel grids with several billions of voxels. To perform a voxelization with a medium resolution (~ 100 million voxels), the algorithm requires from 1 to 10 minutes to execute.

9.2.2. Person and object tracking framework.

One of the main tasks of PODIUM was to develop a tracking system that could substitute personal dosemeters without the need to wear any physical device to perform the personnel tracking, i.e., a completely marker-less solution. In this way, the online dosimetry system would not be subject to the same practicality issue of dosemeters, such as forgetting to wear or losing the tracking device, wearing it incorrectly, having to perform maintenance (changing/charging batteries), etc…

In the original PODIUM concept, as soon as a person walks into a radiation field, her/his position and posture should be detected and tracked. This tracking information together with the position and rotation of the source term is then used to perform dose calculations.

Computer vision emerged as the most promising solution to meet the requirements of PODIUM. Thanks to its detection and tracking algorithms, computer vision allows real-time tracking data to be obtained with speed and accuracy. Furthermore, thanks to the constant improvement of both computational power and neural network models, computer vision-based tracking methods are improving at a fast pace.

Within the PODIUM project, some important achievements were obtained, proving the capabilities of computer vision for tracking exposed workers. However, due to the short time, limitations were

still present by the end of the project. Shortcomings included the impossibility of tracking the ceiling mounted glass shields in the interventional radiology application, the need to build up manually the geometry for each workplace and the need to perform frequent calibrations to accurately locate workers. Furthermore, some stability issues emerged for the tracking algorithms when multiple workers are operating near each other, causing issues such as the fusion of the skeleton tracking or identity switching between different workers. Finally, due to the limited range and area covered by a single 3D camera (Kinect v.2), multiple cameras for monitoring larger areas are needed.

For this reason, new developments have been initiated to upgrade the tracking system and improve its capabilities. First, support for a newer and more capable camera was added, allowing tracking of larger areas and at distances up to 20 meters. The new main camera, the ZED 2i Stereo from StereoLabs® (Stereolabs, San Francisco, California, USA), also offers a more stable and robust person tracking algorithm based on deep neural networks. Being based on stereo RGB cameras rather than infrared illuminators like the Kinect, the ZED camera has some advantages. Besides good accuracy in tracking workers at far distances (+- 10% at 20 meters), the tracking of the ZED camera is less sensitive to lighting conditions, and it is not affected by the presence of other cameras. Furthermore, it requires less power, so that it can be powered by the same single USB C cable providing data transfer.

In order to comply with the requirements of applications such as nuclear medicine (NM) staff dosimetry, support for a highly accurate and compact camera based on LIDAR was added. LIDAR (light detection and ranging) utilizes laser-based distance measurement technology to estimate movement and positioning of objects in three-dimensional space (Van Nam, 2021). The camera, the Intel RealSense L515 offers unmatched performance in terms of spatial accuracy especially for the short distances available inside the typical laminar airflow cabinets of NM departments. In this case, we also developed special tracking algorithms to reconstruct the position of the hand, its fingers and syringes/vials and shielding used by nuclear medicine staff preparing and injecting radiopharmaceuticals.

Besides the ZED and RealSense Lidar cameras, a new system based on ultra-wideband (UWB) sensors was introduced for further improving the tracking accuracy of objects with large effect on the radiation field (such as source term, shielding device, etc…). While partially contrary to the base principle of PODIUM (i.e., to avoid physical devices at all), the UWB sensors are meant to be fixed only to moving objects that are either too far away or do not properly reflect light for accurate tracking through cameras. In the interventional radiology application, UWB sensors are utilized to track the ceiling-mounted shield's position, rotation, and movement. In our system, the UWB sensors from Qorvo® (Qorvo, Greensboro, North Carolina, USA) were adopted because of their performance/cost ratio, and because of the included Software Development Kit (SDK). This SDK allowed us to develop a specialized data logging software to connect to the UWB sensors and fetch positional data in real time.

To simplify the initial setup and calibration of the tracking system, we introduced a more automated method to create a digital twin of the room being monitored. The creation of the digital twin is based on the Matterport Pro2® 3D scanning camera (Matterport, Sunnyvale, California, USA). The Matterport Pro2 camera is an innovative 3D scanning system that creates highly accurate and immersive 3D models of physical spaces. Utilizing a combination of infrared sensors, high-resolution cameras, and artificial intelligence algorithms, the Matterport camera can build digital twins with remarkable precision (of the order of 3-5 cm). The 3D models built with this camera can be easily exported in the most widely common formats (mesh or CAD). To integrate the digital twins with the PODIUM software framework, we used the wavefront OBJ mesh format. By having this digital twin

of the monitored room, we were able to increase substantially the tracking accuracy for both workers and objects of interest.

Together with these improved capabilities, the tracking system was also made less obtrusive by switching the connected acquisition machine from a laptop/desktop computer to a microcomputer. Thanks to its hardware characteristics and because of support of the ZED camera SDK, the Jetson Nano microcomputer from Nvidia (Nvidia, Santa Clara, California, USA) was chosen for our system.

As an additional result, we expect that new cameras together with the integrated microcomputer will allow us to substantially streamline the deployment of the tracking system within the workplace to be monitored, so that aspects such as installation, configuration and maintenance of the tracking system will require less time and effort, reducing the impact on medical staff in terms of workload.

9.2.3. Monte Carlo Simulation Framework.

The third module within the PODIUM system is the Monte Carlo (MC) simulation framework, which takes care of generating input files and running the simulations.

This framework uses tracking data to generate dynamic radiation dosimetry scenarios, automatically calculating transformation matrices from the tracking data. These transformation matrices are used to position and rotate the phantom(s) and other relevant objects in the MC model to reproduce the monitored environment. In this calculation of transformation matrices, the framework accounts for converting tracking data from camera-space-coordinates to world-space-coordinates, with a calibration.

Furthermore, the framework performs some adjustments of the skeleton tracking data, so that it can be fitted to the sizing of a reference adult male or female, according to the ICRP standard human measurements. If major body size differences are present between the tracked person and the standard phantom, it may not be possible to converge the tracking information to fitting with the body and limbs of the phantom. In such cases, the framework recurs automatically to some deterministic and application-specific rules with which we establish whether to give preference to realistically positioning of the body part (typically the most exposed limb) or whether to use a realistic positioning of the whole body while whilst accepting a reduced accuracy in the positioning of the limb.

Finally, the framework also includes a specialized filtration algorithm which removes, if present, jittering noise from the camera tracking.

Besides building a dynamic geometry model of a phantom and the monitored environment, the simulation framework is also used for generating the source definition in the MC input file. For specific applications, such as in interventional radiology, the position, direction, beam size, energy and intensity of the radiation source frequently varies. For this reason, the framework was developed to automatically load source parameters via dose structure report files and time-synchronized irradiation events with the tracking data. By uploading these parameters, the framework automatically generates the source definition within the MC input files.

During PODIUM, the simulation framework was developed to be compatible primarily with the MCNP particle transport code. Recently, support of the Geant4 code was added, providing several technical benefits. Since Geant4 is open source, its development is supported by a large community, which leads to faster inclusion of new features and enhancements. When Geant4 is used by the framework, parts of the simulated environments were defined by using polygonal mesh models

directly, which benefits the accuracy and simplifies the geometry generation process. Furthermore, the open-source nature of Geant4 allowed reduction of the code to run required features only, with substantial increase in performance.

9.2.4. Virtual Reality and visualization of dosimetry data.

Over the last few years, the scope of computational dosimetry has evolved beyond just improving the accuracy of dose assessments. It has become clear that because of the most recently developed tools, computational dosimetry can also deliver comprehensive dosimetry data in a new manner that is both insightful and impactful. By using on the graphic visualization capabilities of the Unity rendering engine, our online dosimetry system can generate a dynamic digital twin of the monitored scene. The intensity distribution of radiation fields in space was rendered by using Unity's particle system and procedural generation of material and textures. This approach allows the generation of overlays of transparent colour coded "fog" around radiation sources, suggesting the presence of high/medium/low intensity radiation fields. The scripts taking care of this visualization were also developed to fetch and readout output simulation files in real time, so that for every simulation that is completed, dosimetry data is immediately reported and visualized.

Besides enhancing real-time dosimetry, the same 3D rendering tools are also used for generating impactful virtual reality training. Because of the possibility of navigating and interacting with the scene, changing source parameters, and changing the configuration of the geometry models, the virtual reality environment allows different irradiation scenarios to be built, so that their effect in terms of doses can be studied.

9.3. Results and Conclusions

The development and refinement of the personal online dosimetry system represents a significant advance for radiation protection and dosimetry. This system is designed to provide real-time dose assessments, aiming to enhance the safety and protection of individuals in highly exposed environments. By employing the RAF phantom family of mesh phantoms and by using real tracking data information, the system can generate dynamic geometry models that reproduce the monitored scene with accuracies in the order about 2-5 centimetres.

The integration of marker-less computer vision and 3D camera technologies allows effective mitigation of common drawbacks characterizing the use of dosemeters, such as forgetting or misplacing the dosemeters and eliminates the need for readout and maintenance logistics.

In the latest iteration, the SCK CEN dosimetry system was further improved by including additional features. We enhanced tracking accuracies and enlarged monitoring areas by updating person and object recognition algorithms (Fig. 9.3), and by adding support for new models of 3D cameras such as the ZED 2i and the Intel RealSense L515.

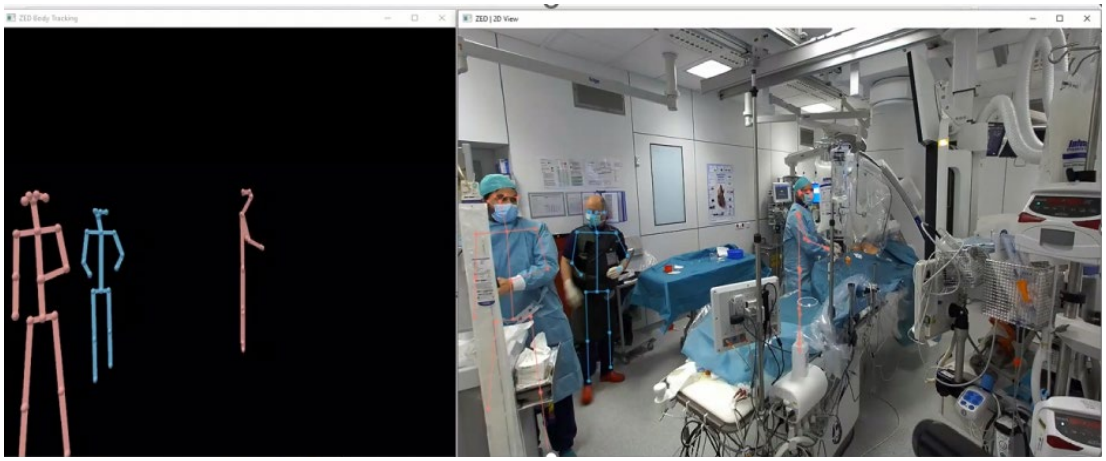

Figure 9.3 Improved algorithm for tracking position and posture of medical staff in interventional radiology.

We also addressed the case of poor computer vision tracking performance by integrating support for UWB based trackers. This approach is resorted to only when due to the light reflection property, materials such as ceiling-mounted lead shielding glass are transparent to the 3D cameras, which can lead to errors or misidentification in the object tracking algorithm. Fig. 9.4 shows the implementation of the UWB for tracking the ceiling mounted shield, and the improved tracking algorithms.

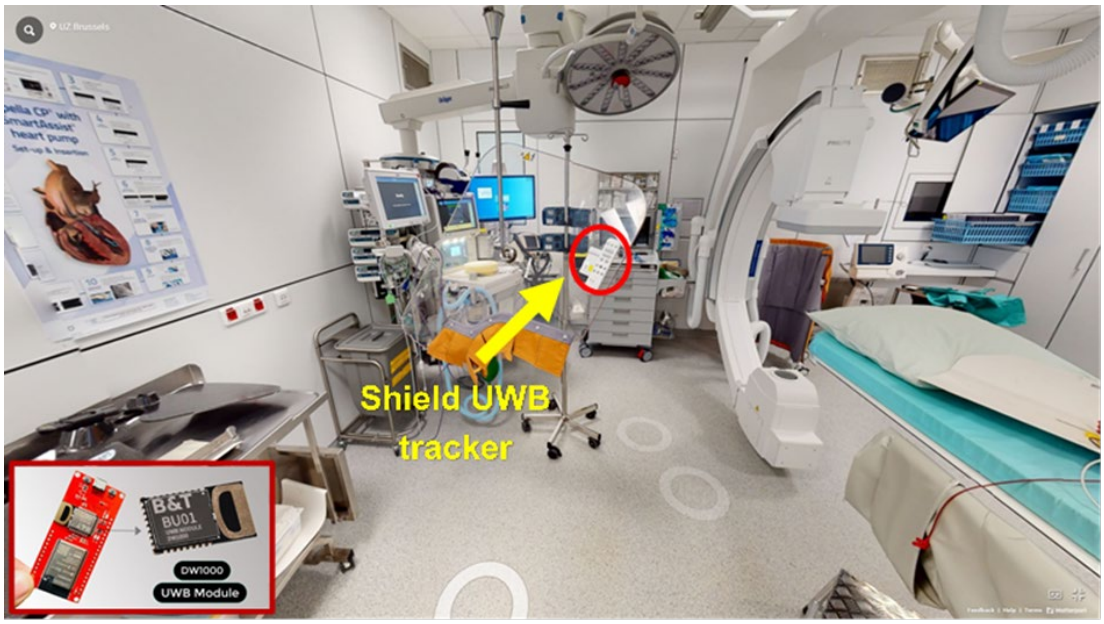

Figure 9.4 UWB trackers implementation for tracking position and orientation of the ceiling mounted shielding in an interventional radiology room.

Improvements were also achieved for the Monte Carlo simulation framework, where support for Geant4 was added, and coordinate calibrations algorithms were automated. The steady evolution of computer hardware and software has made simulations faster and more capable, up to a point where it is currently possible to perform simulations within tens of seconds within applications such as nuclear medicine staff monitoring. Thanks to the advancements in machine learning that are currently carried out for the online dosimetry system, this time is expected to further reduce within the next few years, up to the point where simulations will be performed within 1-2 seconds, so that truly individualized dose assessments will become possible.

We also addressed integration and data management aspects, with the objective of streamlining the deployment of the hardware and software in the operational environment where the system is installed. In doing so, we opted for the use of non-obtrusive edge computing solutions, where the cameras installed in the monitored site are connected to micro-computers performing only highly optimized tasks.

By introducing digital twin creation technology with the Matterport Pro2 3D scanning camera, the installation and configuration of the dosimetry system was simplified while supporting high geometrical accuracy in the creation of the model of a monitored area. Furthermore, this technique facilitates the creation of accurate and immersive digital replicas of the workplace, which can improve the immersivity of our virtual reality environment and thus improve the impact of training activities. Figs. 9.5 and 9.6 show the capabilities of the scanning camera system, which allowed to build up with relative ease an accurate geometrical replica of a temporary waste storage facility at SCK CEN, including a highly realistic texture overlay.

Figure 9.5 3D scanning of a temporary waste storage facility. Note: the red markers in this and the following figures mask parts of the image not to be disclosed owing to privacy and security concerns.

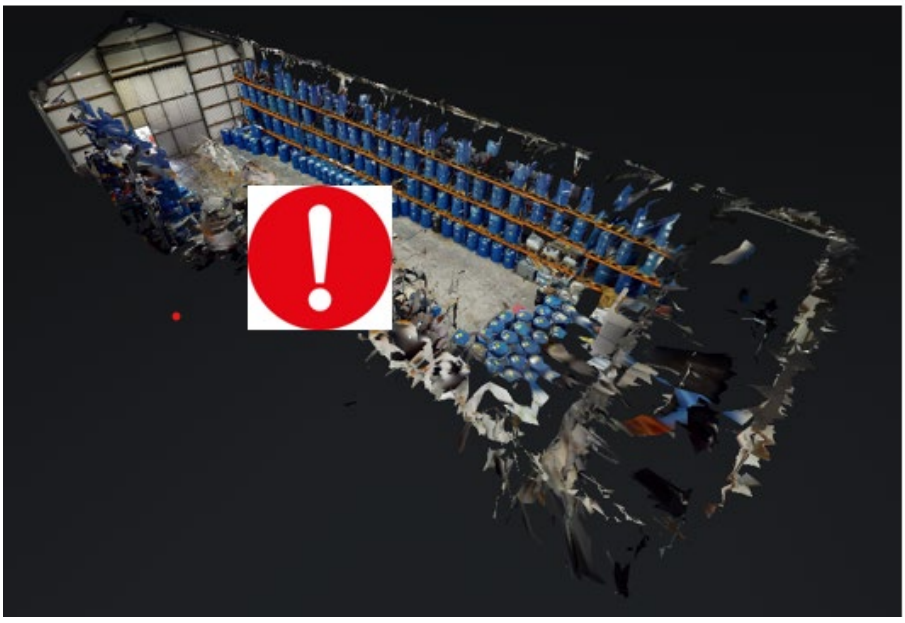

Figure 9.6: Reconstructed 3D model of a temporary storage facility at SCK CEN.

ALARA aspects can effectively increase the usefulness of dosimetry, transforming it into a more active tool to optimize radiation protection. Fig. 9.7 shows the capability of the software to visualize

a dose mapping generated by combining measurements and simulations, which can be used to train workers performing tasks within the facility.

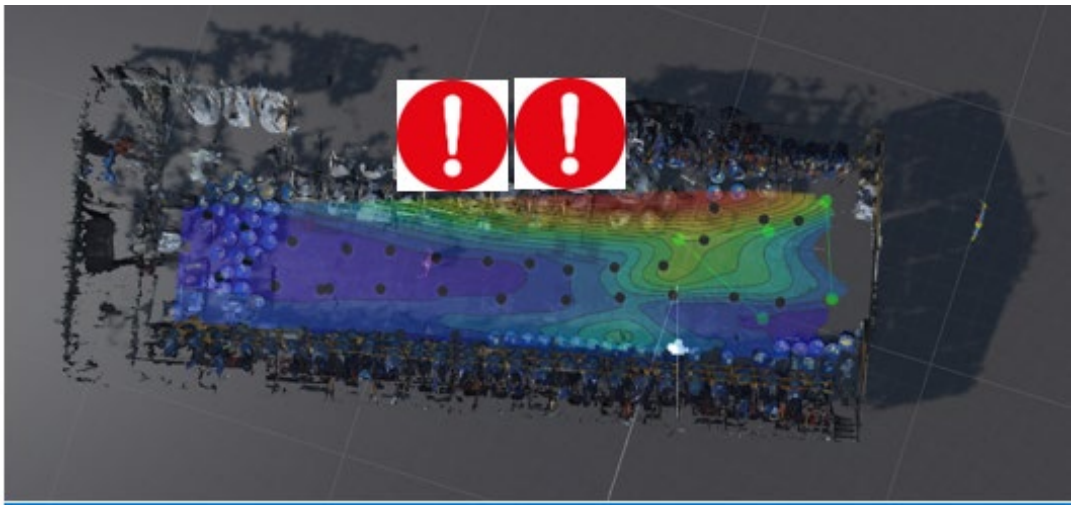

Figure 9.7 Dose mapping overlaid on the reconstructed 3D model of a temporary storage facility at SCK CEN.

Fig. 9.8 shows a tracking test performed within the same temporary storage facility. The improved camera tracking algorithm was able to accurately calculate the position of a worker and thus map the tracking information within the 3D virtual environment. In the figure, the camera view is shown on the left bottom corner, while on the right, the reconstructed digital twin including an avatar representing the worker is shown.

Figure 9.8: View of the camera tracking a worker and the corresponding digital twin reconstruction of the scene.

However, several challenges and limitations encountered in the first version of the Online Dosimetry System are still present in the latest iterations. One of the main challenges remains the robustness of the object tracking algorithm, which can be very sensitive to lighting conditions. This has led us to develop application specific object tracking algorithms, which leads to difficulties in testing and

installing the tracking system in new, untested environments. For the future, more advanced methodologies based on semantic segmentation (Ulku 2022) will be considered.

Another limitation is the difficulty of performing a proper extended validation. Besides difficulties in accessing clinical or nuclear facilities, carrying out validation measurements proved to be particularly difficult due to the lack of a simple measurement methodology that could serve as ground truth for physical and protection quantities. Paradoxically, relying solely on operational quantities for the validation reduces and hampers the added value of computational dosimetry as substitute of physical dosemeters. For example, not being able to validate the time resolution capabilities of the online dosimetry system can complicate the process of acknowledging computational dosimetry as a legally recognized online dose assessment methodology, and thus limit its applicability to passive, *a posteriori* dose assessment. This could even affect the market interest in a dosimetry solution replacing a physical dosimetry service, due to aspects such as higher costs.

In summary, the multifaceted approach of the PODIUM project envisaged an online dosimetry system which integrated cutting-edge technologies from diverse fields. While challenges remain, the rapid pace of advancements ensures that there will be a continuous and steady improvement, and that in the near future, online individualized dosimetry will become a fundamental part of radiation protection methodologies.

9.4. References

Abdelrahman, M., Lombardo, P., Vanhavere, F., Seret, A., Phillips, C., Covens, P., 2020. First steps towards online personal dosimetry using computational methods in interventional radiology: Operator's position tracking and simulation input generation. Radiation Physics and Chemistry, 171, 108702. doi: 10.1016/j.radphyschem.2020.108702.

Autodesk 3Ds Max 2024, Autodesk San Francisco, California, USA 2024. Website: www.autodesk.com/products/3ds-max/overview.

Badal, A., Zafar, F., Dong, H., Badano, A., 2013. A real-time radiation dose monitoring system for patients and staff during interventional fluoroscopy using a GPU-accelerated Monte Carlo simulator and an automatic 3D localization system based on a depth camera, in: Nishikawa, R.M., Whiting, B.R. (Eds.). Presented at the SPIE Medical Imaging Conference, Lake Buena Vista (Orlando Area), Florida, USA, p. 866828. doi: 10.1117/12.2008031

Blender 4.0, Stichting Blender Foundation, Amsterdam, Netherlands 2024. Website: www.blender.org.

ICRP, 2002. Basic anatomical and physiological data for use in radiological protection: reference values. ICRP publication 89. Annals of the ICRP, 32, 5.

ICRP, 2009. Adult reference computational phantoms. ICRP Publication 110. Annals of the ICRP, 39(2).

ICRP, 2020. Adult mesh-type reference computational phantoms. ICRP Publication 145. Annals of the ICRP, 49(3).

Laine, S., 2013. A Topological Approach to Voxelization. Computer Graphics Forum, 32, 77–86. doi: 10.1111/cgf.12153.

Lombardo, P.A., Vanhavere, F., Lebacq, A.L., Struelens, L., Bogaerts, R., 2018. Development and Validation of the Realistic Anthropomorphic Flexible (RAF) Phantom. Health Physics 114, 486–499. https://doi.org/10.1097/HP.0000000000000805.

Motmans, R., 2006. DINBelg 2005. Ergonomie RC, Leuven © 2005-2006. Website: www.dinbelg.be.

NVIDIA Jetson Nano, NVIDIA 2018, Santa Clara, California, USA. Website: https://developer.nvidia.com/embedded/learn/get-started-jetson-nano-devkit.

Ulku, I., Erdem, A., 2022. A Survey on Deep Learning-based Architectures for Semantic Segmentation on 2D images. Applied Artificial Intelligence 136, e2032924 (2157 pages). DOI: https://doi.org/10.1080/08839514.2022.2032924.

Van Nam, D. and Gon-Woo, K., 2021, January. Solid-state LiDAR based-SLAM: A concise review and application. In: 2021 IEEE International Conference on Big Data and Smart Computing (BigComp) (pp. 302-305). IEEE.

ZED 2i Stereo, StereoLabs 2024, San Francisco, California, USA. Website: https://www.stereolabs.com/products/zed-2.

10. Data Processing in Radiation Protection Dosimetry

Robert Bernat, Ruđer Bošković Institut (RBI), Croatia, **Panagiotis Askounis**, Greek Atomic Energy Commision, Greece, **Vedran Bandalo**, Mirion Technologies, Germany, **Codrut Cherestes**, Dositracker, Romania, **Nicky Gibbens**, Public Health England, United Kingdom, **Phil Gilvin**, Public Health England, United Kingdom **Carolina Hernandez Gonzalez**, The Centre for Energy, Environmental and Technological Research (CIEMAT), Portugal, **Irene Mas**, Ministry of Health, Consumer Affairs and Social Welfare, Spain, **Anatol Oprea**, Dositracker, Romania, **Begoña Perez Lopez**, The Centre for Energy, Environmental and Technological Research (CIEMAT), Portugal

Abstract

The topic of data security and practice has regularly been raised at the plenary meetings of EURADOS Working group 2 *Harmonization of Individual Monitoring in Europe*. Due to an increasing interest in this topic, a task group on Dosimetry and Information Technology was formed in 2020.

The increasing interest among individual monitoring services (IMSs) results from a number of factors.

For IMSs there is a need to balance the various requirements for long-term retention, secure transmission and discarding of obsolete data. Since IMSs have different contexts (service size, nature of organisation, national requirements), the principles may need to be interpreted differently. The present work seeks to provide advice to support that the principles may need to be interpreted differently.

10.1. Data processing

Data processing is the converting of information into something that is understood by a computer or simply: manipulation of data by a computer.

Data processed in radiation protection dosimetry include personal data, dose records, medical data (pregnancy dates), industry (of employment) and other information (algorithms, procedures, standards, etc.).

Data storage of the collected information (both data on exposed workers and their dose results) must insure up-time/data availability, integrity of data, and security. Data availability can be split up into two related but separate concepts: up-time/redundancy, and backup.

Up-time/redundancy deals with how to ensure that data stays available in day-to-day routine operations, that is, use of techniques like RAID and/or failover to increase tolerance to equipment failure. It is critical to understand that redundancy is not backup.

Backups are NOT up-time improving technology but a last resort in case of massive failure of routine systems. This also means that it must be a completely separate system from the normal running system. It is especially important that access control is different between routine and backup systems to ensure that if one is compromised, this does not affect the other. By having separate access controls, backups can be protected during more and more common (crypto) ransomware attacks.

With the advance of new technology like Solid State Drives (SSD) and new requirements in ISO/IEC standards, integrity of data is becoming increasingly important. In general, the integrity of data is split into protection against unintended change (failure of equipment, interference with the

equipment etc.) and against intended change (access limit to necessary, logging of all data changes irrespective of access level).

Backup should be considered a last-resort option to recovery of data. This means that backups must be made often enough (how often depends on the data production timing) to ensure that all data that is not recoverable by other means (e.g., by measuring the dosemeter again) is available in case of failure of the primary systems.

Restoration of backups should regularly be checked to confirm that everything works as intended and that backups cover all the data needed. While this is additional work it ensures that when the primary system goes down there is a way back. Test recovery can also be seen as recurring training in the recovery process that will speed up recovery when actually needed.

It is critical to have separate access control for primary systems and the backup. The same set of credentials should never work on both systems so that compromise of one does not affect the other. This is becoming more and more important with advanced threats like ransomware that can easily encrypt backups too, in the case of common access controls. Optimally, completely separate access controls and hardware two-factor authentication should be used.

Given the current threat landscape, where the question is not whether an organisation will be hacked but when, the design of the network should aim at minimising the damage in the event of a breach.

This usually means segmenting the network into protected enclaves that have minimal, if any, contact with each other. However, segmentation introduces an amount of friction and annoyance into use so that there will always have to be a balance between security and ease of use. For each system, there should be evaluation of potential consequences when compromised compared with day-to-day ease of use.

Fig. 10.1 shows a very simplified segmented network with the following components:

- Office network
  - Network for normal users, with access to internet
  - Sealed off from other networks/systems except for users who must have access
- Production network
  - System critical, responsible for dose reads
  - Fully sealed off network that has one way communication to the dose management system (dose data export)
  - Separate credentials from any other system, preferably backed by 2 factor authentication using hardware or Time-based One-Time Password (TOTP)
- Dose management system
  - System critical, responsible for pairing of personal data and dose results as well as issuing dose reports to customers
  - Due to the need for communication this system cannot be sealed off completely
    - It needs input from the production system (doses)
    - It needs input from customer support in the office network
    - It needs ability to export all this data to “customer access” portal
  - Firewalled on all sides with only absolutely necessary services allowed through
  - Separate credentials compared to other networks and backed by 2 factor authentication using hardware or Time-based One-Time Password (TOTP)
- Customer access

- High value system that is exposed to the internet for customer access
  - Exposure to internet is always dangerous as it demands very rapid response to any identified vulnerabilities in the software used which leads to high workload
  - Large, exposed attack surface if direct access to web/application/similar service is exposed
- Must be able to communicate with the main dose management system
  - User must be able to change some of the data
- Should use separate system and credentials from the dose management system
- 2 factor authentication (hardware or TOTP) should be used both by customers and administrators (In general all administrative tasks should demand 2 factor authentication)

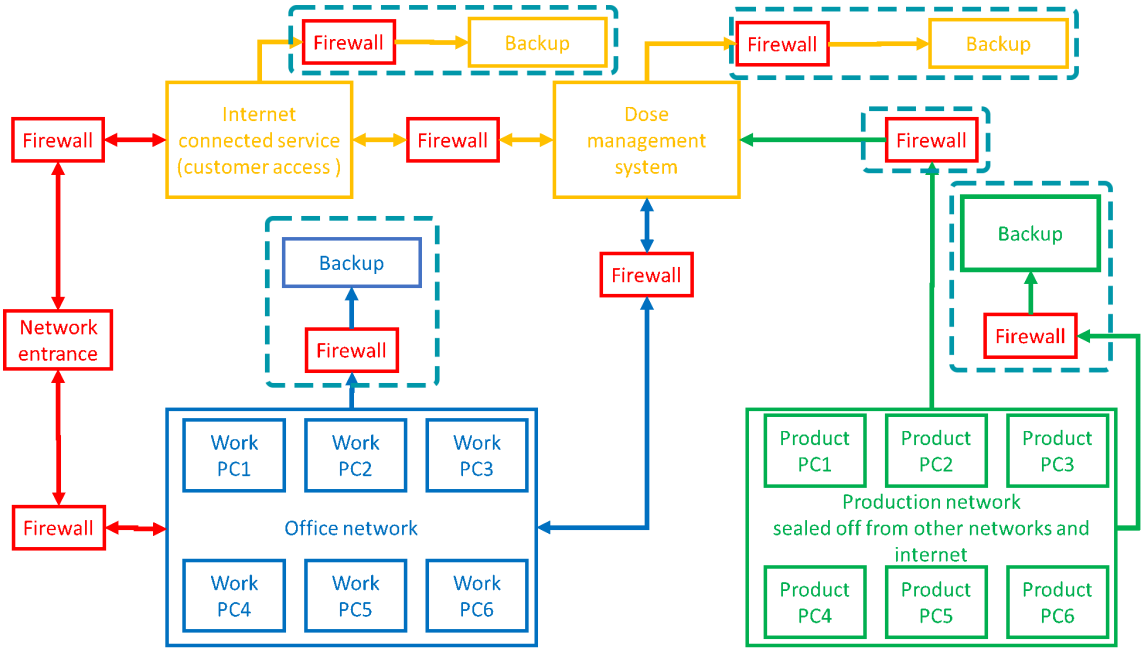

Fig. 10.1: Simplified schematic of a segmented network designed to protect most critical systems.

10.2. Data Encryption

Data encryption converts data from a readable, plaintext format into an unreadable, encoded format. Users and processes can only read and process encrypted data after it is decrypted. The decryption key is secret, so it must be protected against unauthorized access.

Encryption is the process of converting data into an unusable form and does not by itself prevent hacking or data theft. Instead, it prevents stolen content from being used, since the hacker or thief cannot see it in plaintext format.

Dosimetry data may be personal, medical, or commercial in nature and must therefore be handled confidentially. By default, IMSs should send data in encrypted or other protected format; however, the needs of the client must be taken into account. Different arrangements may need to be made for clients whose technology restricts or controls incoming data, or who prefer to receive hard copy documents.

10.3. GDPR – Data minimization

The data minimization principle requires entities to process (collect, store, share with, etc…) only 'adequate, relevant and limited' personal data. EU data protection law does not define what 'adequate, relevant and limited' means but states that the assessment of what is 'necessary' must be done in relation to the purposes of processing.

In accordance with this principle, by default, only the amount of personal data that is necessary for the processing shall be processed. "Amount" refers to quantitative as well as qualitative considerations. Moreover, both the volume of personal data, as well as the types, categories and level of detail must be taken into consideration.

The minimization procedure could be consisting of the following steps:

- **Identification of the necessary data for the purposes of processing**: The key to an efficient data minimization process is to be clear about what is needed and why.
- **Clear definition of processing time.** This could be a major issue as, in many cases, there are other obligations, requirements or regulations demanding long periods of keeping dosimetry data.
- **Correction of inadequate data**: Keep data as up to date as possible (by working with individuals and customers to update their data) and cultivate optimized databases.
- **Limitation of access**: The dosimetry service must define who and which (organisations, radiation officers, health services etc. …) can have access to personal data based on an assessment of necessity. Furthermore, the number of persons who have privileged access to customers' personal data should be minimized
- **Strategic deletion:** in accordance with progressive evaluation protocols, remove any unusable or incorrect information. Consistently purge stale data to ensure the information stored is truly valuable. Discuss what new data is needed as well as any outdated types of information.
- **Reduction of the degree of identification**: If the purpose of the processing does not require the final set of data to refer to an identifiable individual (such as in statistics) then data should be anonymised.
- **Review the whole procedure**

10.4. References

Arokia Paul Rajan, R., 2012. Evolution of Cloud Storage as Cloud Computing Infrastructure Service. IOSR Journal of Computer Engineering (IOSRJCE) ISSN: 2278-0661 1, 38-45.

Deng, Y., 2009. Deconstructing Network Attached Storage systems, Journal of Network and Computer Applications, 32, 1064-1072, ISSN 1084-8045. doi: 10.1016/j.jnca.2009.02.006.

Council Directive 2013/59/EURATOM of 5 December 2013 laying down basic safety standards for protection against the dangers arising from exposure to ionising radiation, and repealing Directives 89/618/Euratom, 90/641/Euratom, 96/29/Euratom, 97/43/Euratom and 2003/122/Euratom.

EU REGULATION 2016/679 of 27 April 2016 on the protection of natural persons with regard to the processing of personal data and on the free movement of such data, and repealing Directive 95/46/EC.

EU, 2018. Technical recommendations for monitoring individuals for occupational intakes of radionuclides. Radiation Protection N° 188.

Ju, J.H., Wu, J.Y., Fu, J.Q., Lin, Z.J., 2011. A Survey on Cloud Storage. Journal of Computational Physics, 6. 1764-1771. Doi: 10.4304/jcp.6.8.1764-1771.

Liu, K., Dong L.J., 2012. Research on Cloud Data Storage Technology and Its Architecture Implementation. Procedia Engineering, 29, 133-137. doi: 10.1016/j.proeng.2011.12.682.

Liu, A., Yu, T., 2018. Overview of Cloud Storage. International Journal of Scientific and Technology Research, 2018. hal-02889947.

O'Reilly, J., 2016. Network Storage: Tools and Technologies for Storing Your Company's Data, 1st Edition. ISBN 978-0-12-803863-5. Morgan Kaufmann Publications.

Tate, J., Beck, P., Ibarra, H.H., Kumaravel, S., Miklas, L., 2021. Introduction to Storage Area Networks. https://www.redbooks.ibm.com/abstracts/sg245470.html?Open (accessed April 2021).

Trikha, Bindu., 2010. A Journey from floppy disk to cloud storage. International Journal on Computer Science and Engineering, 2, 1449-1452.